Enhancement of Rydberg atom interactions using dc and ac Stark shifts

by

Parisa Bohlouli-Zanjani

A thesis
presented to the University of Waterloo
in fulfillment of the
thesis requirement for the degree of
Doctor of Philosophy
in
Physics

Waterloo, Ontario, Canada, 2010

I hereby declare that I am the sole author of this thesis. This is a true copy of the thesis, including any required final revisions, as accepted by my examiners.

I understand that my thesis may be made electronically available to the public.

Abstract

This thesis reports the use of both dc and ac electric field induced resonant energy transfer, RET, between cold Rydberg atoms as a useful tool for enhancement of interatomic interactions. A general technique for laser frequency stabilization and its suitability for Rydberg atom excitation is also demonstrated.

RET between cold Rydberg atoms was used to determine Rydberg atom energy levels. The ^{85}Rb atoms are laser cooled and trapped in a magneto-optical trap. For energy level determination experiment, atoms were optically excited to $32d_{5/2}$ Rydberg states. The two-atom process $32d_{5/2} + 32d_{5/2} \rightarrow 34p_{3/2}+30g$ is resonant at an electric field of approximately 0.3 V/cm through dipole dipole interaction. The experimentally observed resonant field, together with the Stark map calculation is used to make a determination of the ^{85}Rb ng-series quantum defect to be $\delta_g(n = 30) = 0.00405(6)$.

The ac Stark effect was also used to induce RET between cold Rydberg atoms. When a 28.5 GHz dressing field was set at specific field strengths, the two-atom dipole-dipole process $43d_{5/2} + 43d_{5/2} \rightarrow 45p_{3/2} + 41f$ was dramatically enhanced, due to induced degeneracy of the initial and final states. This method for enhancing interactions is complementary to dc electric-field-induced RET, but has more flexibility due to the possibility of varying the applied frequency. At a dressing field of 28.5 GHz all of the participating levels ($43d_{5/2}$, $45p_{3/2}$ and $41f$) show significant shifts and these give a complicated series of resonances. An oscillating electric field at 1.356 GHz was also used to promote the above RET process where the atoms are initially excited to the $43d_{5/2}$ Rydberg states. The ac field strength was scanned to collect RET spectra. Different resonances were observed for different magnetic sublevels involved in the process. Compared to the higher dressing field frequency of 28.5 GHz, the choice of dressing frequency of 1.356 GHz, which is slightly blue detuned from the $41f - 41g$ transition, and structure of the spectra may be understood, by analogy with the dc field case.

Acknowledgements

I owe thanks to many people for the completion of this dissertation.

- To my supervisor James D D. Martin, with whom it has been a privilege to work with. I would like to thank him for his ongoing and excellent advices and free donation of his time. My research was greatly improved by the high standards with which he conducts his own work.
- To my committee members, W.-K. Liu, Donna Strickland and Peter Bernath, for their invaluable insights.
- To Walt W. Duley and K.T. Leung, for kindly agreeing to act as examiners and for their comments on this thesis work.
- To A. Kumarakrishnan, from York University, for carefully reading this thesis. This dissertation was greatly improved by his invaluable suggestions and comments.
- To the administrative staff of the Physics Department, especially Judy McDonnell for her constant presence with a beautiful smile to help and assist graduate students.
- To Andy Colclough in the Physics Student Machine Shop for his help and suggestions especially in the early stages of setting up the magneto-optical trap.
- To all members of the Laser Cooling and Trapping group, especially Joseph Petrus for his tremendous help on ac Stark shift experiment and to Kourosh Afrousheh, Maria Fedorov, Ashton Mugford, Owen Cherry, and Jeff Carter for their friendship, assistance and support.
- To Roshanak Moradi for her love, care, and priceless coffee breaks that we shared together.
- To my schoolmates and friends for their support, help, great discussions, comments, criticism, and fun: Zahra Fakhraii, Sina Valadkhan, Hamidreza Molavian, Sattar Taheri, Mohaddesseh Azimloo, Leila Shahrzad, Ghodrat Esmaeili, Roxana Moradi, Shadi Khonsari, Zarrin Langari, Mahtab Kamali, Alaleh Dara, Mojgan Daneshmand, Pedram Mousavi and many others whose names are inadvertently left out... thank you all.

- To my sisters and best friends Nazila, Sanaz, and Golnaz for their friendship, understanding, and continuous encouragements and their families for their love and support.

- To my brother Hamidreza for his friendship and support. Regardless of where he was and what he was doing, he always made sure to be present when I needed him the most.

- To my husband's parents and family members for their love, understanding and encouragements.

- To my little Ideen and Yashar for their encouragements with their childish words and sweet smiles. I was blessed to experience the joy of motherhood halfway through my PhD program. They have been such an inspiration for me even long before they were born.

- To my parents Mehri and Shokrollah for, well, everything. I am forever indebted to them for what they have done for me to succeed. You are both far beyond any appreciation.

- To my beloved friend, schoolmate, and husband Ali Nasseri-Moghaddam. I owe thanks to him not only for his care, support and loving inspiration but also for his scientific and technical insights, which always helped me and kept me positive through out this demanding journey. This thesis is as much a product of his support, and patience as it is of my efforts. Thank you my love!

to my mother and my father

(Mehri Khatibi and Shokrollah Bohlouli-Zanjani)

Dear Mother and Father;

I am forever indebted to you for your unconditional love and all you have done for me to succeed. You are far beyond any appreciation.

With profound love and respect I dedicate this dissertation to you.

Parisa

Waterloo - Canada
May 2010

I would like to translate this dedication into Farsi, the language that they taught me:

مادر عزیزم، پدر مهربانم؛

عشق بی قید و شرط، زحمات و ازخود گذشتگیهای شما فراتر از هرگونه تقدیر و سپاسگزاری است.
تنها میتوانم در مقابل قامت صبور و عاشق شما زانو زده و بر دستهای گرم و مهربانتان بوسه بزنم .

این رساله دکترا را با عشق و احترامی عمیق به شما تقدیم مینمایم.

پریسا

واترلو- کانادا
اردیبهشت ۱۳۸۹

Contents

List of Tables

List of Figures

Chapter 1

Introduction and Background Theory

1.1 Introduction

1.1.1 Rydberg Atoms

A Rydberg atom is an atom with a single valence electron in a high principal quantum number, n, state [1, 2]. The excited valence electron is shielded from the electric field of the nucleus by the electrons in the ion core of a Rydberg atom. Therefore the excited electron sees the ion-core as a single elementary charge, like the electron of a hydrogen atom. Rydberg atoms are similar to the hydrogen atom in many aspects. The energy levels of hydrogen can be obtained from the Rydberg formula:

$$E = \frac{-R_y}{n^2} \tag{1.1}$$

where for an atom with nuclear mass M, $R_y = M(M + m_e)^{-1}R_\infty$ with $R_\infty = \frac{m_e c\alpha^2}{2h} = 13.605$ eV [3]. In these equations, m_e is the mass of the electron and R_∞ is the Rydberg constant. Since the electron is much lighter than the proton, $R_y \approx R_\infty$.

The energy levels of atoms other than hydrogen differ from the energy level relation in Eq. 1.1. When the valence electron is far from the ionic core (high angular momentum, l, states) the orbits become more circular and the valence electron is only sensitive to the net charge and behaves like the hydrogen atom. On

the other hand, when the valence electron comes near the ionic core (low-l states) it can polarize and penetrate the ionic core. To adjust the Rydberg equation for this penetration of the inner core electrons, a correction term called the "quantum defect" is introduced. The Rydberg relation is modified to include the quantum defect of the element being studied:

$$E = \frac{-R_y}{(n^*)^2}. \tag{1.2}$$

The principal quantum number n in Eq. 1.1 is replaced by an effective principal quantum number $n^* = n - \delta_l$ where δ_l is the quantum defect of the state of angular momentum l. The quantum defect is different for different angular momentum states. For low-l states the penetration and polarization of the core electrons by the valence electron lead to large quantum defects and the atom shows less hydrogenic behavior (ex. for ^{85}Rb s-series: $\delta_s \approx 3.13$). Whereas, the non penetrating high-l states of Rydberg atoms have small quantum defects (ex. for ^{85}Rb f-series: $\delta_f \approx 0.0165$) which scale as $1/l^5$ [1].

The radius of the charge distribution of the valence electron scales as n^{*2} (this was experimentally confirmed by Fabre *et al.* in 1983 [4]). Due to the vast separation of the electron and ion-core in high-n Rydberg atoms, these atoms have large transition dipole moments. These large transition dipole moments make the Rydberg atoms much more sensitive to electric fields than less excited atoms. For example, the electric polarizability for the quadratic Stark effect for low-l Rydberg states increases as n^{*7} [1]. Rydberg states can also be ionized in rather weak fields. The classical field for ionization of the ground state of atomic hydrogen is 3.2×10^8 V/cm, while the field required to ionize a Rydberg state with $n = 47$; is 65.9 V/cm - which can be obtained easily in the laboratory. The low ionization threshold of Rydberg states results in effective detection of such states.

In general, different properties of Rydberg atoms scale with some power of n^*, and as n^* increases these properties can be exaggerated.

Table 1.1 gives the various properties of Rydberg atoms and their dependence on n^* [5]. As shown in this table, the energy between adjacent n states scales as n^{*-3} and electric dipole moment scales as n^{*2}. Rydberg atoms therefore strongly absorb millimeter wave (mm-wave) radiations. High-resolution spectroscopy of Rydberg atoms using mm-wave transitions has been used as a probe of external electric or magnetic field and also for precise measurement of fine and hyperfine structure intervals [6, 7, 8, 9, 10, 11].

Table 1.1: Properties of Rydberg atoms [5]

Property	n^* dependence
Binding energy	n^{*-2}
Energy between adjacent n states	n^{*-3}
Orbital radius	n^{*2}
Electric dipole moment	n^{*2}
Geometric cross section	n^{*4}
Polarizability	n^{*7}
Radiative lifetime (low-l states)	n^{*3}
Radiative lifetime (high-l states)	n^{*5}
Fine structure interval	n^{*-3}

Because of these unusual properties, Rydberg atoms have been of interest in physics and chemistry for a long time. In 1970, the invention and development of narrow bandwidth frequency tunable dye lasers made it possible to selectively populate highly excited states in the laboratory. Hence spectroscopic studies of Rydberg states became more common. Since then, the interest in Rydberg atoms has increased constantly. Laser cooling and trapping is one of the techniques that has opened new areas of research related to Rydberg atoms such as ultra cold plasmas [12, 13] and quantum computing with cold neutral atoms (see for example [14, 15]).

The large transition dipole moments of Rydberg atoms can be exploited for various means. For instance, energy transfer between Rydberg atoms may often be tuned into resonance using dc electric fields [16]. Rydberg atoms are also sensitive to small oscillating electric fields. For example, microwave dressing fields may be used to modify the dc polarizabilities of Rydberg states [17].

In the present experiments, the Rydberg states of ^{85}Rb atom are used. Rb is an alkali metal atom with 36 electrons in a closed core and one optically accessible valence electron. Laser cooling and trapping techniques in a magneto-optical trap are employed to have a higher density and narrower velocity distribution for the atomic sample. The valence electron of Rb can be optically excited from its ground state, $5s_{1/2}$, to the first excited state, $5p_{3/2}$, by a cw diode laser. It is subsequently excited to the Rydberg state, nl, by a frequency doubled Ti:Sapphire laser and then to $n'l'$ Rydberg states by absorption of the mm-waves.

Laser cooled Rydberg atoms are then employed to study the atomic structure and its behavior in the presence of dc and ac electric fields. Exaggerated behavior of Rydberg atoms in response to electric fields makes it possible to readily induce resonant energy transfer, RET, between the Rydberg atoms. The ac and dc electric-field-induced RET are then used to enhance the interactions between Rydberg atoms and determine their energy levels.

Electric fields shift the atomic energy levels and split them into several spectral lines due to the Stark effect. In the following sections a brief description of the Stark effect and resonant dipole-dipole interactions are presented.

1.2 Background Theory

1.2.1 Stark calculation

The effect of an electric field on Rydberg states is known as the Stark effect. In the presence of an electric field, Rydberg state energies are shifted; spherical symmetry is lost and l fails to be a good quantum number as the electric field mixes different l states. The effect arises because of the interaction between the electric dipole moment of an atom with an external electric field. If the electric field is uniform over the length scale of the atom, then the perturbing Hamiltonian is of the form

$$\hat{H}' = -\overrightarrow{\mu} \cdot \overrightarrow{\varepsilon} = e\varepsilon_z z, \tag{1.3}$$

where $\overrightarrow{\mu}$ is the electric dipole moment and $\overrightarrow{\varepsilon}$ is the electric field. Some part of the following explanations are adapted from Ref. [1].

Hydrogen

It is easiest first to consider the behavior of the hydrogen atom in a static field. The effect of electron and nuclear spins are small, thus neglected. Assuming the applied field ε is in the z direction, the electron's potential energy V is calculated in atomic units by,

$$V = -\frac{1}{r} + \varepsilon_z z. \tag{1.4}$$

Using the zero field nlm angular momentum eigenstates, the matrix elements $\langle nlm\,|\varepsilon_z z|\,n'l'm'\rangle$ of the Stark perturbation to the zero field Hamiltonian can be calculated. The matrix element in spherical coordinates is

$$\langle nlm\,|\varepsilon_z z|\,n'l'm'\rangle = \varepsilon_z \langle nlm\,|r\cos\theta|\,n'l'm'\rangle \tag{1.5}$$

where the quantization is along the z axis. These matrix elements are non vanishing if $m' = m$ and $l' = l \pm 1$ due to the properties of the spherical harmonic angular functions. The ε field lifts the degeneracy of the lm states of a particular n state. For all the diagonal elements, the Hamiltonian matrix has the same term, $-1/2n^2$. If the electric dipole coupling to other n states is neglected, when the matrix is diagonalized all of its eigenvalues will be proportional to ε. That means the H atom shows a linear Stark shift. Stark states with linear Stark shift, have permanent electric dipole moments. For non-relativistic hydrogen, the highly degenerate zero-field states fan out into a "manifold" for each m_l, which remains a good quantum number.

The energy separation between the extreme states of the manifold increases with n. Figure 1.1 shows the Stark structure and field ionization of the $|m_l| = 1$ states of the H atom. The levels exhibit linear Stark shift from zero field to the point at which field ionization occurs, which is shown by broken lines in Fig. 1.1. We also see, in this diagram, that the down shifted Stark states ionize at lower fields compared to the up shifted states. The classical threshold field for ionization of different Stark states, which is obtained from $E_c = -2\sqrt{\varepsilon}$ [1], is shown by a heavy line. Figure 1.1 also shows that the levels of n and $n+1$ cross, which is because of the lack of coupling between these states.

Alkali-Metal Atoms

Alkali-metal atoms have similar characteristics to the H atom in an electric field. However as described before, the presence of the finite sized ionic core in these atoms results in important differences. For example, in contrast to the H atom's case the wave function is no longer separable in parabolic coordinates. The presence of the core in zero field reduces the energies, especially those of the lowest l states. In the region below the classical ionization limit, the n and $n+1$ state do not cross as they do in H. Since these states are coupled in alkali atoms, they exhibit avoided crossings.

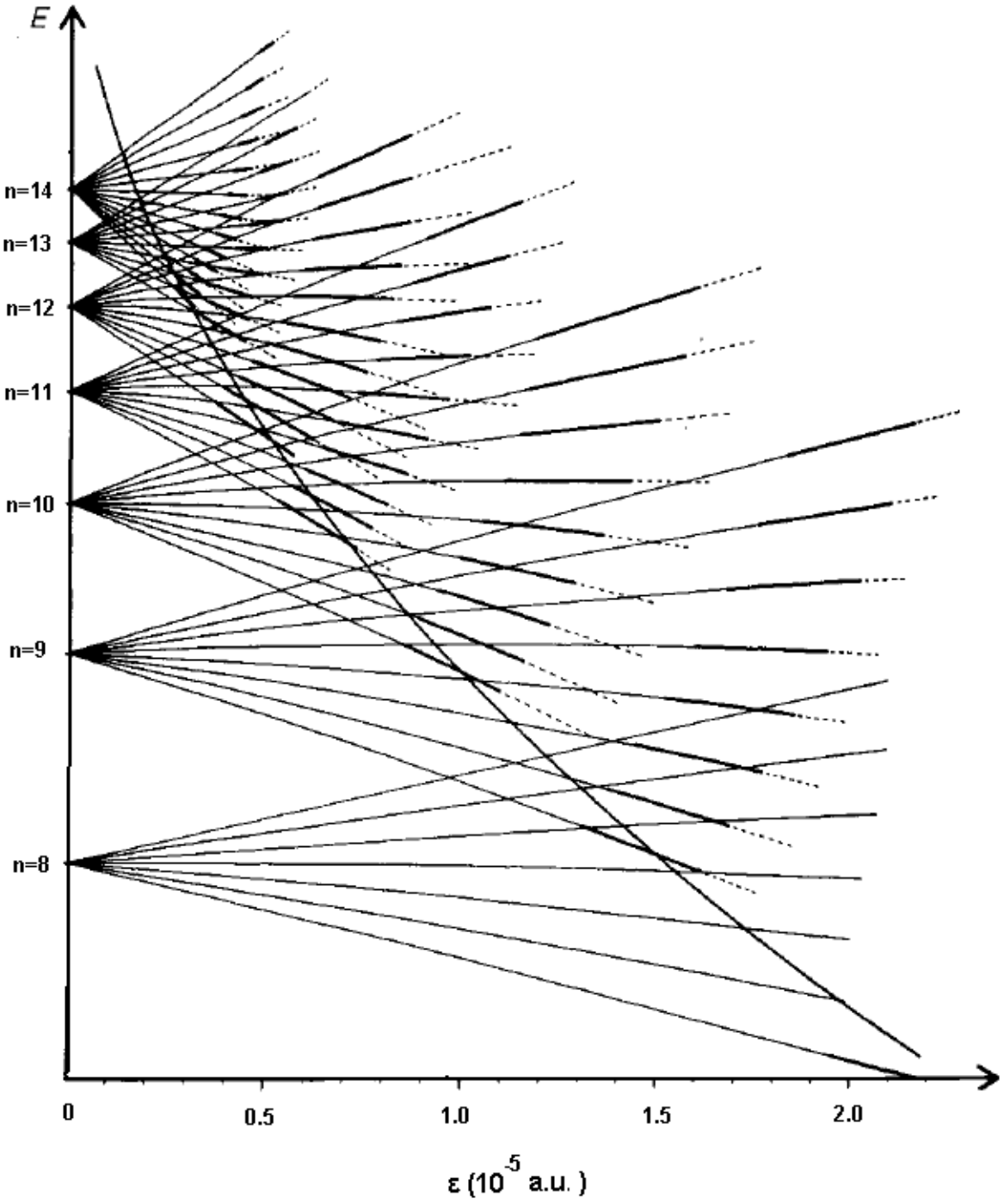

Figure 1.1: Energy level diagram for the hydrogen atom as a function of electric field. The field ionization properties for different Stark states are also marked by heavy lines (from Ref. [1]).

An efficient method of calculating the energy levels (Stark maps) for alkali metals in Rydberg states is described by Zimmerman *et al.* [18]. Using the same method, the Stark map of Rb for high n Rydberg states is calculated and illustrated in Fig. 1.2 [19] . If the Rydberg electron's spin is neglected, the Hamiltonian is given by [1],

$$H = -\frac{\nabla^2}{2} + \frac{1}{r} + V_d(r) + \varepsilon_z z \tag{1.6}$$

where $V_d(r)$ is the difference between the Rb potential and the Coulomb potential,$-1/r$, and is only nonzero near $r = 0$. By direct diagonalization of the Hamiltonian matrix we can calculate the energies and wave functions. If we use the Rb nlm spherical states as basis functions, the diagonal matrix elements are given by the energies of the zero field nlm states. These are well approximated by [1],

$$\langle nlm\,|H|\,nlm\rangle = \frac{1}{2(n-\delta_l)^2} \tag{1.7}$$

where δ_l is the quantum defect. Off diagonal matrix elements are given by,

$$\langle nlm\,|\varepsilon_z z|\,n'l\pm 1m\rangle = \delta_{m,m'}\delta_{l,l'\pm 1}\varepsilon_z \langle l,m\,|\cos\theta|\,l\pm 1,m\rangle\langle n,l\,|r|\,n',l\pm 1\rangle \tag{1.8}$$

where $\delta_{m,m'}$ and $\delta_{l,l'\pm 1}$ are the selection rules, and $\langle l,m\,|\cos\theta|\,l\pm 1,m\rangle$ is the angular matrix component derived using spherical harmonics,

$$\langle l,m\,|\cos\theta|\,l-1,m\rangle = \left(\frac{l^2-m^2}{(2l+1)(2l-1)}\right)^{1/2} \tag{1.9}$$

$$\langle l,m\,|\cos\theta|\,l+1,m\rangle = \left(\frac{(l+1)^2-m^2}{(2l+3)(2l+1)}\right)^{1/2} \tag{1.10}$$

The radial matrix component, $\langle n,l\,|r|\,n',l\pm 1\rangle$, is calculated by numerical integration. If several n manifolds of l states are included, the eigenvalues of the Hamiltonian matrix give the energy levels of the Rb atom in the field and the Stark maps are generated by simply connecting the eigenvalues of the matrix. In Fig. 1.2, the Stark energy states of the Rb atom for $n = 44$ manifold for $|m_j| = 1/2$ are shown. This Stark map is obtained by direct diagonalization of the Hamiltonian matrix [19]. In zero field, the quantum defects $\delta_{s_{1/2}}$, $\delta_{p_{1/2}}$, $\delta_{p_{3/2}}$, $\delta_{d_{3/2}}$, and $\delta_{d_{5/2}}$ of the Rb states displace them (s, p, and d states) from the high l states and they only exhibit large Stark shifts when they intersect the manifold of Stark states. The s, p, and d states undergo quadratic Stark effect at low fields (s and p states are shown in Fig. 1.2). Unlike the Stark map of hydrogen the energy levels of different

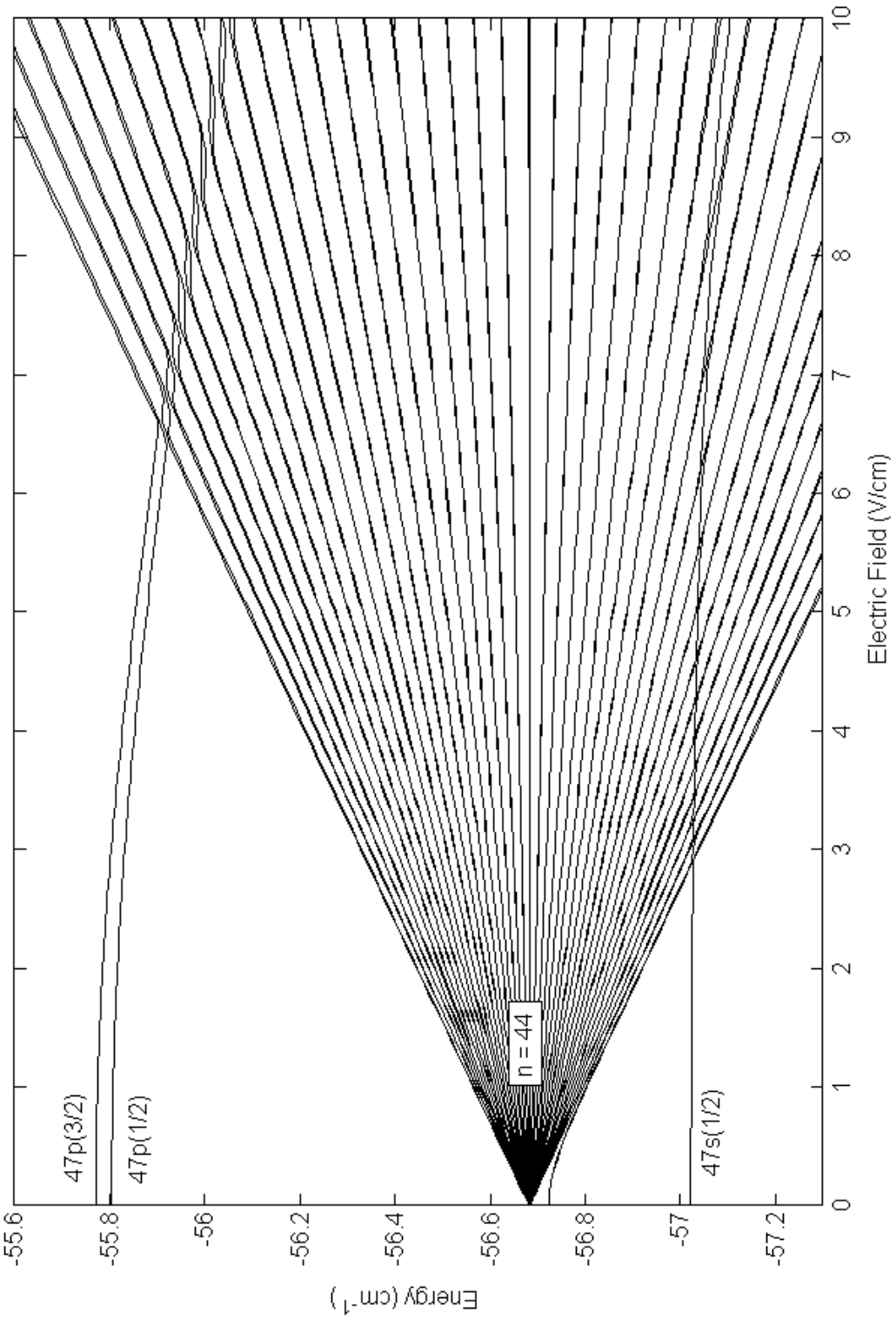

Figure 1.2: Calculated Stark structure of the $|m_j| = 1/2$ states of the Rb atom at the $n = 44$ manifold. [19]

n do not cross in the Rb stark map. For a heavy alkali metal such as Rb, the fine structure interaction is large enough to influence the Stark structure and must be taken into account. The fine structures of the p and d states of Rb are large and can not be neglected, so that $|m_j|$ rather than $|m_l|$ is the "good " quantum number. Each $|m_j|$ manifold is a mixture of states with $m_l = m_j \pm \frac{1}{2}$. As illustrated in Fig. 1.2, the fine structure interaction has been implemented into the Stark calculation [19]. Since high-l ($l > 3$) states have negligible quantum defects at zero field, they fan out into a "manifold" for each m_l. These states have hydrogenic Stark shifts, as illustrated in Fig. 1.2 for the $n = 44$ manifold.

In the present work we use external electric fields to create resonant interactions between ultra cold Rydberg atoms by inducing Stark shifts of atomic energy levels. Thus far, the dc Stark effect has only been discussed. Oscillating electric fields may also be used to enhance atomic interactions. The ability to vary both the frequency and amplitude of the ac field gives additional freedom in achieving the resonance condition. In general, the magnitude and direction of the Stark shifts depend on the frequency and amplitude of the electric field being applied. This can be better understood if we look at the perturbative energy level shifting for both dc and ac electric fields. Using second order perturbation theory, the dc Stark shift of a state $|\phi>$ in a dc electric field of magnitude ε_z in the z direction is given by (see, for example, [20]):

$$\Delta E_\phi = \varepsilon_z^2 \sum_{m \neq \phi} \frac{|<\phi|\mu_z|m>|^2}{(E_\phi - E_m)} \tag{1.11}$$

where E_m refers to the energy of state $|m>$ and μ_z is the electric dipole moment in the z direction. Similarly an equation of the ac Stark shift can be developed. The ac Stark shift of a state $|\phi>$ in an electric field oscillating at angular frequency ω with amplitude ε_z in the z direction is given by (see, for example, Ref. [21]):

$$\Delta E_\phi = \frac{1}{2}\varepsilon_z^2 \sum_{m \neq \phi} \frac{(E_\phi - E_m)|<\phi|\mu_z|m>|^2}{(E_\phi - E_m)^2 - (\hbar\omega)^2} \tag{1.12}$$

This equation is equivalent to Eq. 1.11 when ω is set to 0 apart from a 1/2 factor due to time averaging the oscillating field. More importantly, in Eq. 1.12 we have an additional parameter, ω, that can be used to alter the shift direction.

1.2.2 Resonant electric dipole-dipole energy transfer between cold Rydberg atoms

As discussed in Sec. 1.1.1, highly excited Rydberg atoms have large electric transition dipole moments compared to ground state atoms. This is due to the large separation of the Rydberg atom's valence electron from the ionic core. The size of dipole transition moments, which scales as n^{*2} (n^* is the effective principle quantum number), dictates the strength of the dipole-dipole interaction between two atoms. Therefore, the negligible dipole-dipole interaction between atoms in ground states could become enormous by excitation to Rydberg states. The dipole-dipole interaction between two atoms (a and b) is given by (see for example Ref. [22]):

$$\hat{V}_{dd} = \frac{\vec{\mu}_{\rm a} \cdot \vec{\mu}_{\rm b} - 3(\vec{\mu}_{\rm a} \cdot \vec{n})(\vec{\mu}_{\rm b} \cdot \vec{n})}{R^3_{\rm ab}} \tag{1.13}$$

where $R_{\rm ab}$ is the separation of the two atoms, $\vec{n}$ is a unit vector pointing between them, and $\vec{\mu}_{\rm a}$ and $\vec{\mu}_{\rm b}$ are transition dipole moments evaluated on each of the individual atoms. Energy is transfered between atoms a and b through the dipole-dipole interaction and the Rydberg states of these atoms are shifted. The large dipole-dipole interaction between neighboring Rydberg atoms can be made even larger if they are resonant. Resonance energy transfer, RET, occurs when a pair of atoms have the same total energy in two different state configurations. In general this could be written as:

$$a + a \rightarrow b + c. \tag{1.14}$$

The large Stark shifts of cold Rydberg atoms may allow the resonant condition to be exactly obtained by application of an electric field. In the resonant condition the key element is that the total energy of the initial states is the same as that of the final states.

Figure 1.3 illustrates RET for the process in Eq. 1.14. On the left side of the figure a pair of atoms are illustrated to be initially in the same energy state, E_a, at zero electric field. On the right side the energy levels are shifted with electric field such that the energy separation between states a and b ($E_{ab} = E_b - E_a$) is equal to the energy separation between states a and c ($E_{ca} = E_a - E_c$). In this condition energy is transfered between the two atoms through dipole-dipole interaction and one atom goes up in energy and the other one goes down in energy. Static electric fields have been used experimentally to tune energy levels into resonance. For example, Safinya *et al.* [16] used dc electric field to tune the energy levels ($20s$,

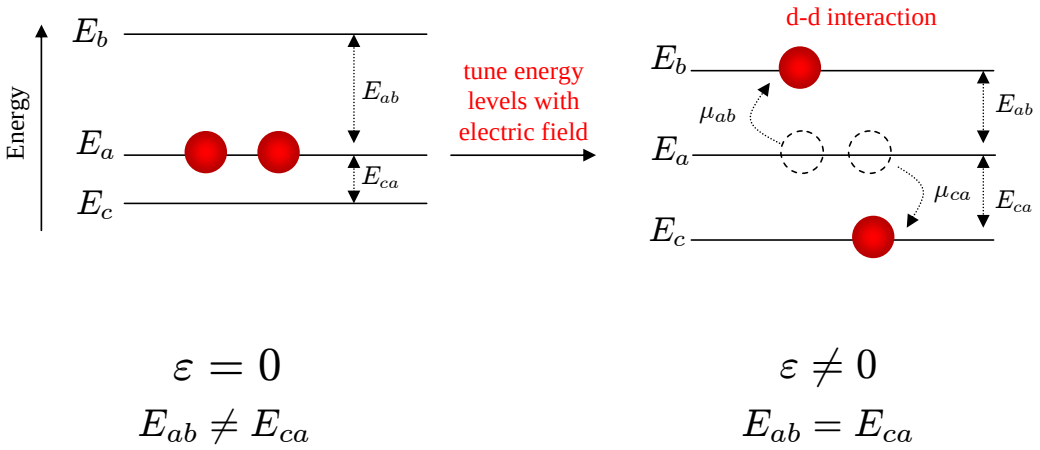

Figure 1.3: The left side is an energy level schematic of a pair of atoms in zero electric field; both atoms are in the same energy state. On the right, in the presence of an electric field the energy levels are shifted; in this process one atom gives a specific amount of energy to the other atom through a dipole-dipole interaction (see process of Eq. 1.14). μ_{ab}, μ_{ca}: transition dipole moments; ε: electric field.

$20p$, and $19p$) of atomic Na into resonance (Fig. 1.4); this process is written as:

$$20s + 20s \rightarrow 20p + 19p. \tag{1.15}$$

In Fig. 1.4, the four energy transfer resonances are shown where the intervals between the $20s - 20p$ and $20s - 19p$ are equal at dc electric fields of $\approx 200 - 240$ V/cm. Resonant energy transfer between Rydberg atoms was first studied in atomic beam experiments (see for example Refs. [4, 16]). The invention of magneto-optical trap made it possible to study the interactions between frozen Rydberg atoms [23, 24, 25, 26, 27]. For example, Vogt *et al.* [28] have demonstrated RET between cold Cs Rydberg states ($38p_{3/2}$, $38s_{1/2}$, and $39s_{1/2}$) at small electric fields $\approx 1 - 2$ V/cm.

In the present work atomic energy levels are determined by dc field induced RET spectra. This work also demonstrates the use of weak microwave dressing fields to tune electric dipole-dipole interactions between Rydberg atoms into resonance, in a case where this cannot be accomplished by dc fields.

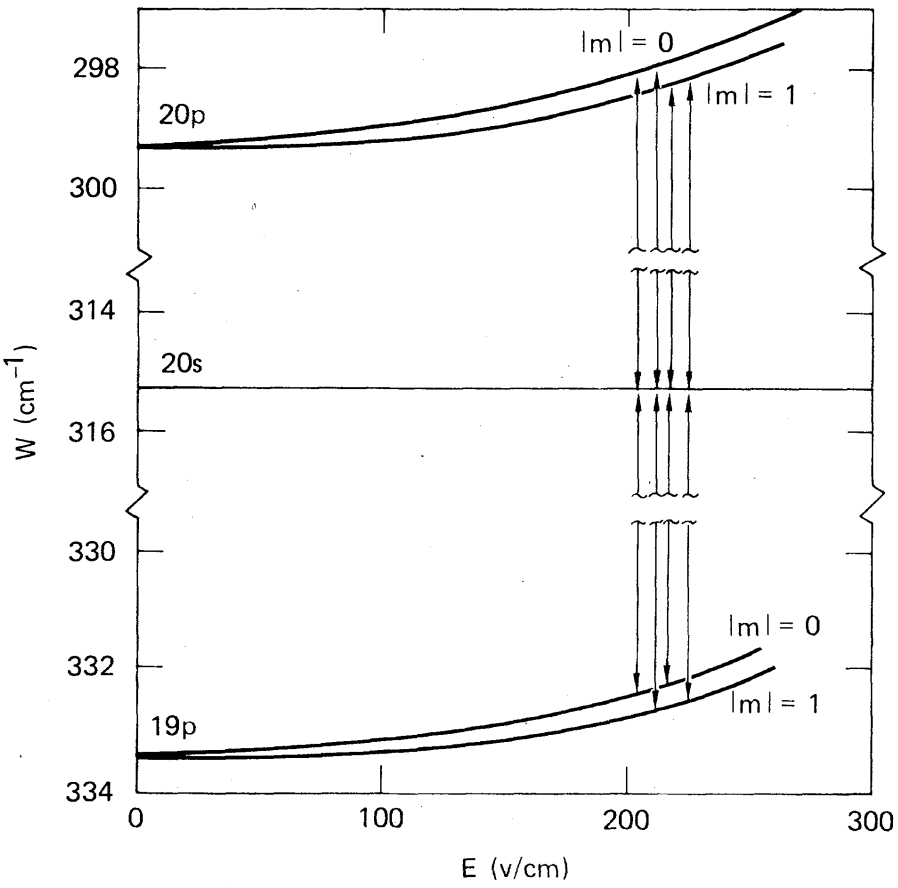

Figure 1.4: Energy levels of Na in an electric field showing the four energy transfer resonances where the intervals between the $20s - 20p$ and $20s - 19p$ are equal (from Ref. [16]).

1.3 Organization of the thesis

This thesis is organized as follows:

- In Chapter 2, the operation of the magneto-optical trap to produce ultra cold samples of ^{85}Rb atoms is briefly described. Then the techniques that were used to produce and detect Rydberg atoms are presented. Many of these techniques have been developed by others [29, 30, 31, 32, 33] and they are included in this thesis as a reference for future experiments. Due to the sensitivity of Rydberg atoms to electric and magnetic fields, it is essential to be able to compensate any stray fields. The last part of this Chapter describes the techniques that were developed to address this issue.

- In order to reliably excite Rb atoms to a desired Rydberg state the excitation laser frequency needs to be stabilized to within less than a MHz. The excitation of cold Rb atoms to nl Rydberg states occurs as a two-color process with 780 nm light (to excite atoms from the ground state $5s_{1/2}$ to the first excited state $5p_{3/2}$) and 480 nm light (for $5p_{3/2}$ to nl Rydberg state). The 480 nm light is obtained by frequency doubling the output of a 960 nm Ti:sapphire ring laser. In Chapter 3 we report a general technique for laser frequency stabilization at arbitrary wavelengths using a reference laser and transfer cavity. Using this technique the Ti:sapphire laser is stabilized with frequency drift of < 1 MHz/hr.

- Chapter 4 is devoted to the study of dc electric-field-induced RET between Rydberg atoms. The two-atom process $32d_{5/2} + 32d_{5/2} \rightarrow 34p_{3/2} + 30g$ is resonant at an electric field of approximately 0.3 V/cm. This process is driven by the electric dipole-dipole interaction. The experimentally observed resonant field together with the Stark map calculation is used to determine the ^{85}Rb ng-series quantum defect.

- In Chapter 5 it is demonstrated that weak microwave dressing fields can be employed to tune electric dipole-dipole interactions between Rydberg atoms into resonance. This method for enhancing interactions is complementary to dc electric-field-induced RET(Ch.4), but benefits from the ability to shift energy levels either up or down by an appropriate choice of frequency. The dressing frequency is set at 28.5 GHz to enhance $43d_{5/2} + 43d_{5/2} \rightarrow 45p_{3/2} + 41f$ process.

- The results in Chapter 5 agreed with the theoretical predictions for the ac Stark effect, but it is not obvious why 28.5 GHz was an appropriate frequency to use. At this frequency all of the participating levels ($43d_{5/2}$, $45p_{3/2}$ and $41f$) show significant shifts and these give a complicated series of resonances. In Chapter 6, it is demonstrated that a much lower frequency of 1.356 GHz, chosen to be slightly blue detuned from the $41f - 41g$ transition, shifts only $41f$ significantly. We can shift the $43d_{5/2} + 43d_{5/2} \rightarrow 45p_{3/2}+41f$ process into resonance by varying the dressing field amplitude. Since the only important magnetic sublevel structure is due to the $41f$ states the spectra are not as complicated as in the case of much higher dressing frequency.

- Chapter 7 includes a summary and proposed future work.

Chapter 2

Experimental Techniques

This chapter starts with a description of the operation of the magneto-optical trap used for the production of cold atoms. Rydberg atoms are produced by exciting the cold atoms; this excitation scheme is also presented. The selective field ionization technique for Rydberg state detection is discussed.

Studying Rydberg atoms in the presence of external fields is a major part of this thesis work. Since Rydberg atoms are very sensitive to electric fields, the techniques that were used for compensating stray fields and application of precisely known electric and magnetic fields are explained in the last section.

2.1 Magneto-Optical Trap

To study the interactions between cold Rydberg atoms, laser cooled and trapped atoms were excited to Rydberg states. A standard vapour-cell Rubidium magneto-optical trap (MOT) was used to make a cold cloud of atoms [34, 29, 35]. A detailed description of the operation of a MOT is presented in author's MSc thesis [36]. In this section the modifications to the MOT are highlighted.
Comprehensive studies of laser cooling and trapping can be found in literature, such as Ref. [29]. The magneto-optical trap has been the most commonly used apparatus for producing cold samples of neutral atoms since its invention in 1987 [35]. A schematic picture of a MOT is shown in Fig. 2.1. Atoms that are captured from a vapour in a vacuum cell are initially at room temperature and move randomly in all directions. To achieve cooling and trapping in three dimensions, we use three pairs

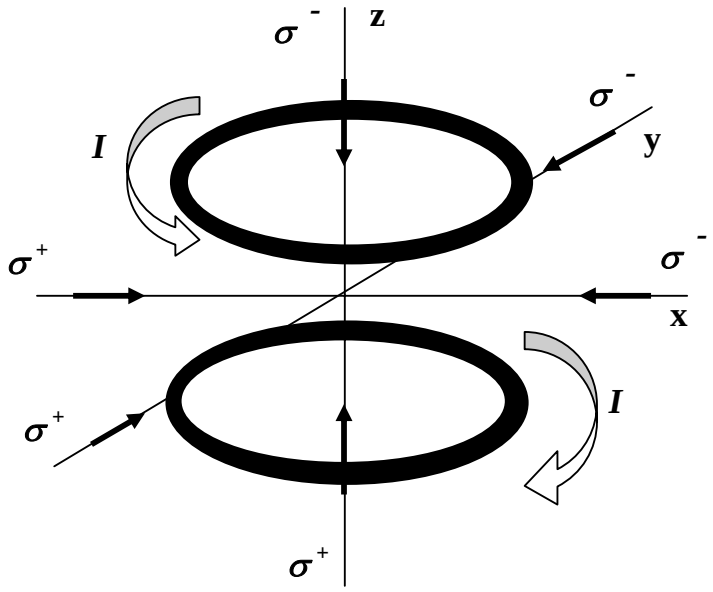

Figure 2.1: Schematic diagram of the anti-Helmholtz coils configuration of MOT and three orthogonal $\sigma^+\sigma^-$ standing waves. Since the currents in the two coils are in opposite directions, there is a $|B| = 0$ point at the center.

of counter-propagating laser beams and an inhomogeneous magnetic field produced by a pair of anti-Helmholtz coils (Fig. 2.1).

The primary force that atoms feel is a radiation pressure force or recoil each time they scatter a photon and receive its momentum. The momentum kick that the atom receives from each scattered photon is quite small; however, by exciting a strong atomic transition, it is possible to scatter more than 10^7 photons per atom per second and produce a large deceleration [29].

To account for the Doppler effect caused by the atomic motion, the laser beams are detuned below specific atomic transition. In this case, atoms scatter more photons from the laser beam that opposes their motion. Also, the laser beams are circularly polarized such that counter propagating beams have opposite helicity. The combination of an inhomogeneous magnetic field and circularly polarized laser beams ensures that atoms experience a space dependent force. This way, atoms experience a friction force (needed for cooling) that damps the velocity of atoms, and a harmonic force (required for trapping) that binds the atoms to the trap center [29]:

$$\vec{F} = -\beta\vec{v} - k\vec{r}. \tag{2.1}$$

In the experiment presented in this text, ^{85}Rb atom is used. Cooling and trapping Rb atoms in a MOT requires laser light at two frequencies, one for cooling and trapping and another one for repumping (Fig. 2.2). This is required since Rb atom is not a perfect two level system.

For ^{85}Rb, the $5s_{1/2}(F = 3) \rightarrow 5p_{3/2}(F = 4)$ transition at 780 nm is an appropriate transition for laser cooling and trapping. However, due to the detuning necessary for cooling there is a small transition probability to $5p_{3/2}(F = 2 \text{ and } 3)$ states. If an atom is excited to $5p_{3/2}(F = 3)$ the atom is then free to decay either to the $5s_{1/2}(F = 3)$ state, where it will continue cycling, or to the $5s_{1/2}(F = 2)$ state. Without a mechanism for removing atoms from the $5s_{1/2}(F = 2)$ state, atoms will be optically pumped and stop interacting with the $5s_{1/2}(F = 3) \rightarrow 5p_{3/2}(F = 4)$ laser. A repump laser is used to drive the $5s_{1/2}(F = 2) \rightarrow 5p_{3/2}(F = 3)$ transition and put the population back into the cycle so that cooling can continue.

The energy levels of ^{85}Rb for the ground state ($5s_{1/2}$), the first excited state ($5p_{3/2}$), and the transitions used for cooling and trapping in a MOT are shown in

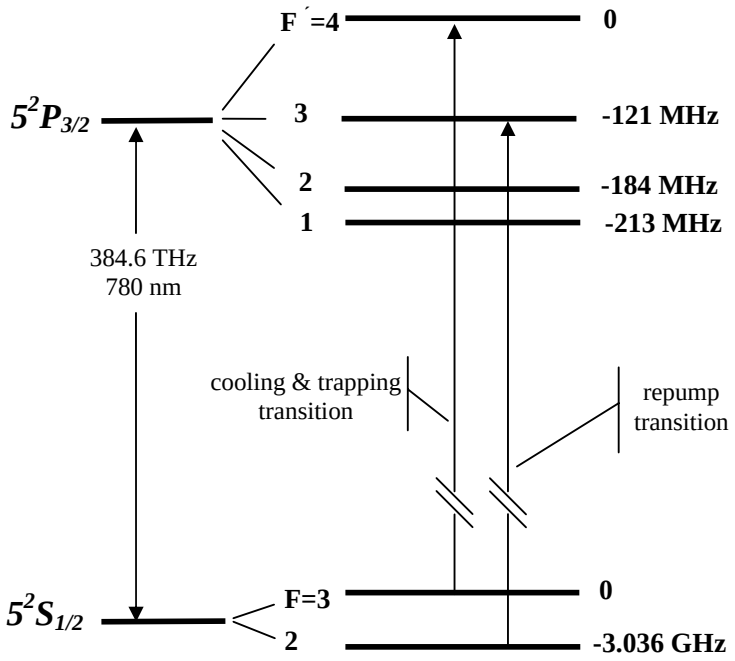

Figure 2.2: Hyperfine structure of the $5s_{1/2}$ and $5p_{3/2}$ states of ^{85}Rb, showing the cooling-trapping and repump transitions [29, 37]. Energy separation of the hyperfine states are shown relative to the $F = 3$ hyperfine state for the $5s_{1/2}$ states and the $F = 4$ hyperfine state for the $5p_{3/2}$ states.

Fig. 2.2. Both cooling-trapping and repump lasers are locked to atomic transitions in ^{85}Rb. The cooling-trapping laser is locked using beat-note locking techniques [38, 30] whereas the repump laser is locked using the the dichroic atomic-vapor laser lock (DAVLL)[31]. Saturated absorption spectroscopy (SAS)[32] was used to identify the cooling-trapping and repump atomic transitions for the purpose of laser frequency locking. SAS and DAVLL techniques are explained in Ref. [36]. A brief description of beat-note locking technique is explained at the end of this section.

For the cooling-trapping transition a high power commercial external cavity, grating stabilized, diode laser (Toptica DLX 110, 780 nm, output power: 380 mW) was used. The output beam of this laser was split into three beams. One beam went to the setup for SAS to identify the cooling-trapping atomic transitions and carried roughly 3 mW power. The second beam (70 mW) was used for beat-note locking (see Sec. 2.1.1) for laser frequency stabilization. The third beam of the cooling-trapping laser (300 mW) was focused down into an acousto-optical modulator (AOM) (IntraAction, Model ME-801ENG Modulator Driver) to be able to quickly switch off the light going into the when it is required. The first-order diffracted output of the AOM was coupled into a single mode fiber in order to shape the laser beams going into the MOT, and also reduce the sensitivity of the MOT to any changes in the alignment of the lasers. The output of the fiber was then split into six beams which were sent into the MOT setup in a configuration shown in Fig. 2.1.
For the repump transition, a home-made external cavity diode laser was used. The output beam of repump laser was also split into three beams. One beam went to a setup for SAS to identify the repump atomic transitions. The second beam went to a DAVLL setup for laser frequency stabilization. To enhance the repump power, the third beam of the repump laser was used to injection lock a temperature stabilized, commercial, 780 nm diode laser (Thorlabs, DL7140-201S). The output of the slave laser (output power: 35 mW), now used as the repump beam for the MOT, was coupled into a single mode fiber and then split into two beams which were made collinear with a pair of counter propagating cooling-trapping beams. The maximum coupling efficiency that was obtained for single mode fibers was roughly 50%.

As mentioned earlier in this section, here are the summary of the modifications made on the MOT used in Ref. [36] to further improve the stability and shape of the cold cloud of atoms for the experiments described in this work:

1. In order to obtain Gaussian spatial profiles for the cooling-trapping and repump lasers, and also reduce the sensitivity of the MOT to any changes in

the alignment of the lasers, the lasers were coupled into single mode fibers.

2. For the cooling-trapping laser, a high power commercial external cavity diode laser was used (Toptica DLX 110, output power: 380 mW) instead of a home-made external cavity diode laser (output power: 40mW) to compensate for the power loss in fiber coupling and increase the number of cold atoms in the MOT.

3. As for repump laser, a home-made external cavity diode laser (ECDL) was frequency stabilized using DAVLL technique. To enhance the repump beam power, the frequency stabilized beam of the ECDL was used to injection lock another 780 nm diode laser. The output of the second laser was then fiber coupled and sent into the MOT as a repump beam.

4. The cooling-trapping laser was stabilized using a beat-note locking technique (see next section).

5. In the old setup three beams were sent into the MOT in three orthogonal directions. Each beam was then retro reflected to account for the counter propagating beams as shown in Fig. 2.3. The three beams which were retroreflected had slightly lower power compared to the counter propagating beams. This resulted in displacement of the quadrupole zero of the MOT and instability of the trap. In the new setup, the cooling-trapping beam was focused down into an AOM to be able to quickly switch off the laser beams used for the MOT. The first-order diffracted output of the AOM was fiber coupled. The fibre output power was then split into six equal beams which were sent into the MOT setup in a configuration shown in Fig. 2.1 to address the instability of the trap due to the beam power imbalance in the old setup.

2.1.1 Beat-note locking technique

Using this technique [30] the difference frequency (beat-note frequency) of two independent diode lasers at 780 nm is stabilized. One of the lasers is the cooling-trapping laser to be stabilized using the beat-note technique and the other laser serves as the master laser for laser frequency stabilization of a Ti:sapphire 960 nm ring laser (see Chapter. 3). The master laser is locked using the polarization spectroscopy technique [33]. The beat-note signal of the cooling-trapping laser and the master laser experiences a frequency-dependent phase shift when it passes

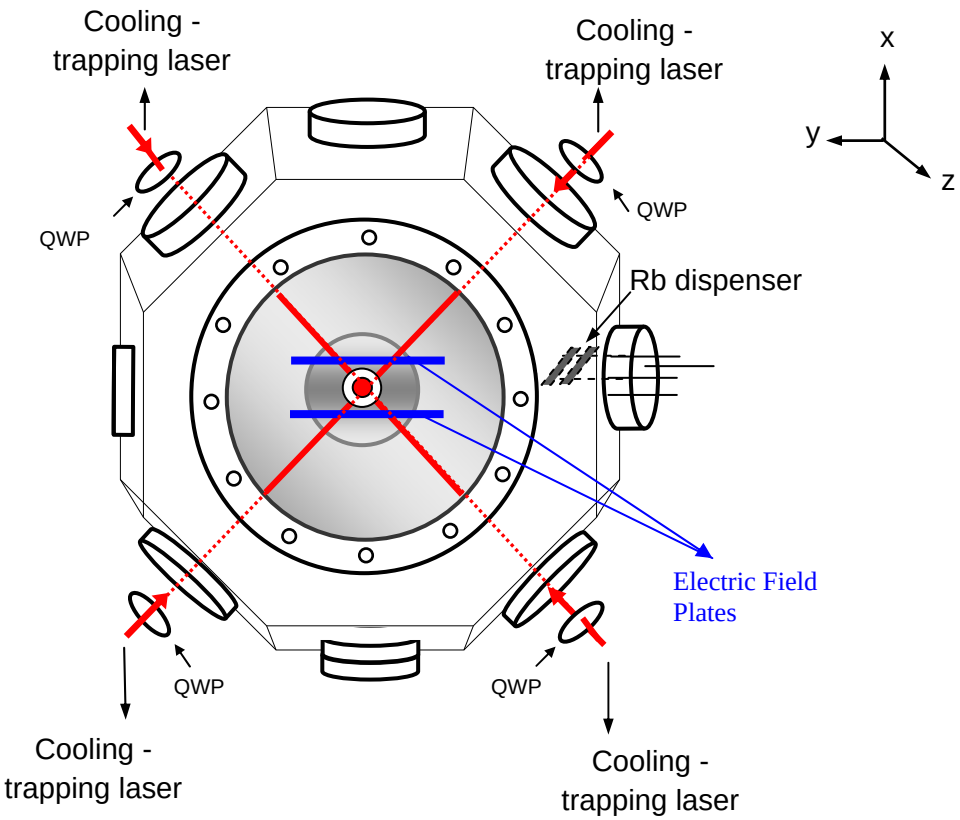

Figure 2.3: Schematic drawing of vacuum chamber showing the six orthogonal $\sigma^+\sigma^-$ standing waves in the MOT (not to scale). Quarter wave plates are labelled QWP. The third pair of beams, perpendicular to the page, is shown by a dot at the center of the chamber. The repump beam is sent into the trap in z direction.

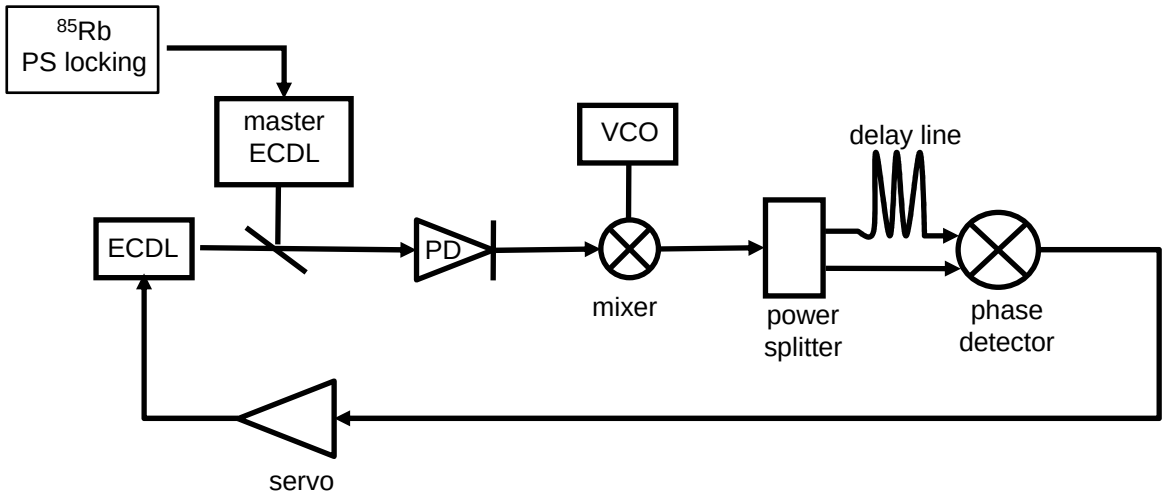

Figure 2.4: Schematic diagram of the circuit for beatnote frequency locking; ECDL, external cavity diode laser (master ECDL is locked using polarization spectroscopy technique [33]); PD, photodiode; VCO, voltage-controlled oscillator.

through a coaxial cable. In the locking system used for this work the difference frequency of two diode lasers is stabilized close to the frequency difference of the $5s_{1/2}(F = 3) \rightarrow 5p_{3/2}(F = 2)$ and $5s_{1/2}(F = 3) \rightarrow 5p_{3/2}(F = 4)$ transitions in ^{85}Rb (see Fig. 2.2). A small portion of each laser beams are focused onto a photodiode to generate and measure the beat note frequency. The photodiode output signal at frequency $\Delta f \approx 180$ MHz is first amplified and then mixed with the output of a voltage-controlled oscillator (VCO) at f_{VCO}. The output of the mixer, $|\Delta f - f_{VCO}|$, is split into two equal parts. After one part is delayed by a coax cable the two parts are recombined on a phase detector. The zero crossings of the phase detector output as a function of the beat frequency provides error signal for locking the beat frequency using a servo loop. The locking point can be tuned by varying the reference frequency f_{VCO}. Figure 2.4 is a schematic diagram of the circuit for the beatnote frequency locking.

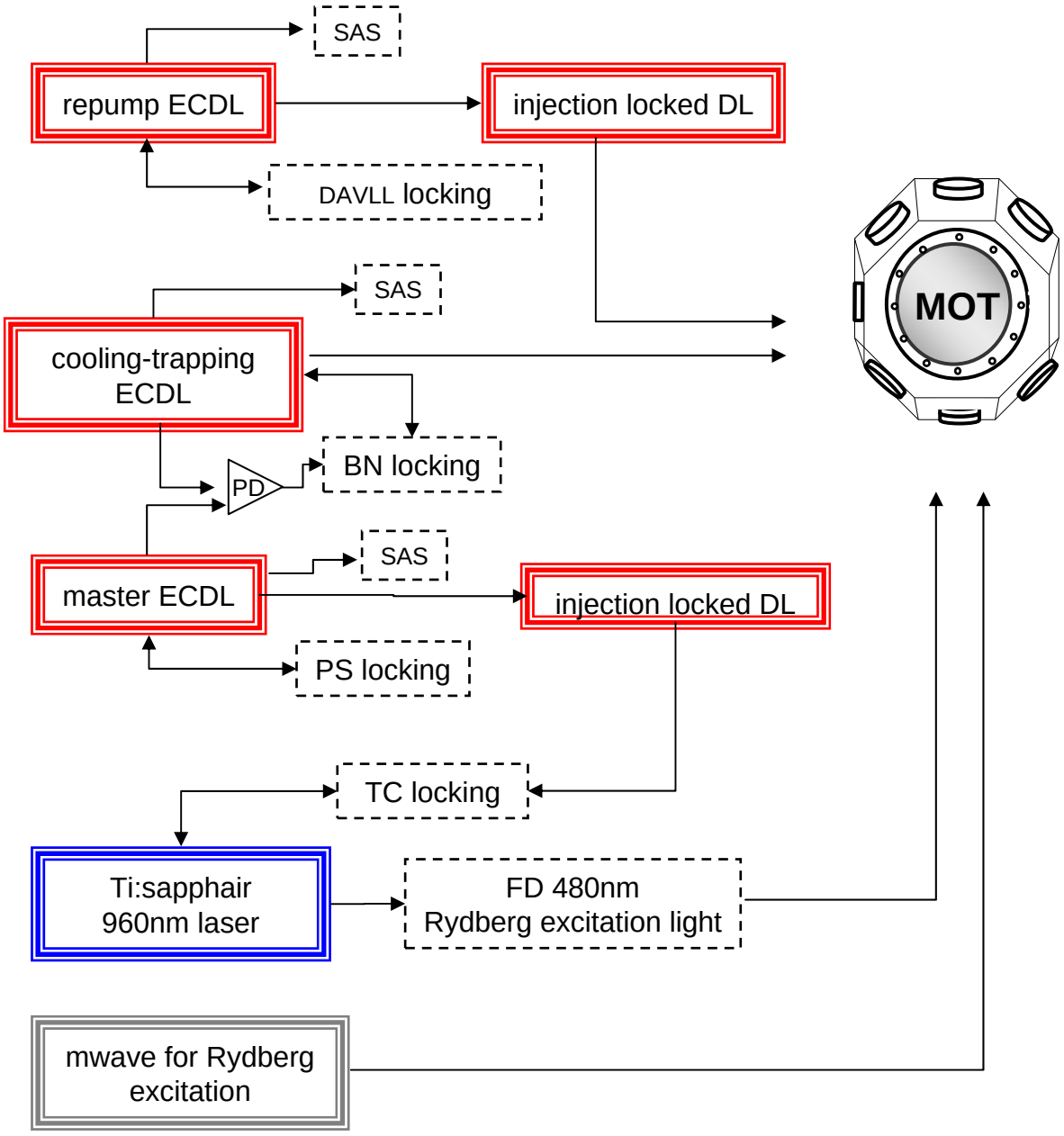

Figure 2.5: Schematic drawing of all the lasers and their locking schemes that were used in the experiments presented in this thesis. SAS: Saturated Absorption Spectroscopy; DL: Diode Laser; PD: Photo Diode; TC: Transfer Cavity (see Chp. 3); FD: Frequency Doubler; ECDL: External Cavity Diode Laser; DAVLL: Dichroic Atomic-Vapor Laser Lock.

2.2 Production of Rydberg Atoms

2.2.1 Optical excitation

In the experiments presented in this thesis, excitation of cold ^{85}Rb atoms to Rydberg states occurs as a two-color process with nearly resonant 780 nm light ($5s_{1/2} - 5p_{3/2}$) and 480 nm light ($5p_{3/2} - nl$). The 780 nm light is necessary for the ^{85}Rb MOT and is detuned approximately 12 MHz to the red of the $5s_{1/2}(F = 3) \rightarrow 5p_{3/2}(F = 4)$ transition. Figure 2.5 is a schematic drawing of all the lasers and their locking schemes that were used in these experiments.

Figure 2.6 shows the excitation of the ground state Rb atoms to Rydberg states in a MOT. The 480 nm light is obtained by frequency doubling the output of a 960 nm Ti:sapphire ring laser. The 780 nm cooling and trapping light remains on continuously. The 480 nm light is pulsed using an acousto-optic modulator. In most of the experiments described in this text Rb Rydberg atoms are excited to higher Rydberg states using microwave pulses. A pulsed electric field is then applied to field ionize any Rydberg atoms and draw the resulting ions to a microchannel plate (MCP) detector. Experiments are done at a 10 Hz repetition rate.
The 960 nm laser is frequency stabilized using a transfer cavity. The transfer cavity is stabilized using a rf current-modulated diode laser which is injection locked to a 780 nm reference diode laser. The reference laser is stabilized using the polarization spectroscopy in a Rb cell [33]. The Ti:sapphire ring laser at 960 nm is locked to this transfer cavity and may be precisely scanned by varying the rf modulation frequency. This technique for frequency stabilization of 960 nm laser will be described in detail in Chp. 3.

2.3 Detection of Rydberg atoms using selective field ionization (SFI)

The large separation of the electron and ion-core in Rydberg atoms makes them quite susceptible to dc electric fields. One of the most sensitive methods for detection of Rydberg atoms is the selective field ionization technique (SFI) [39]. In this method the atoms are ionized in an increasing electric field, and the resulting electrons or ions are detected as a function of applied field. SFI has become the

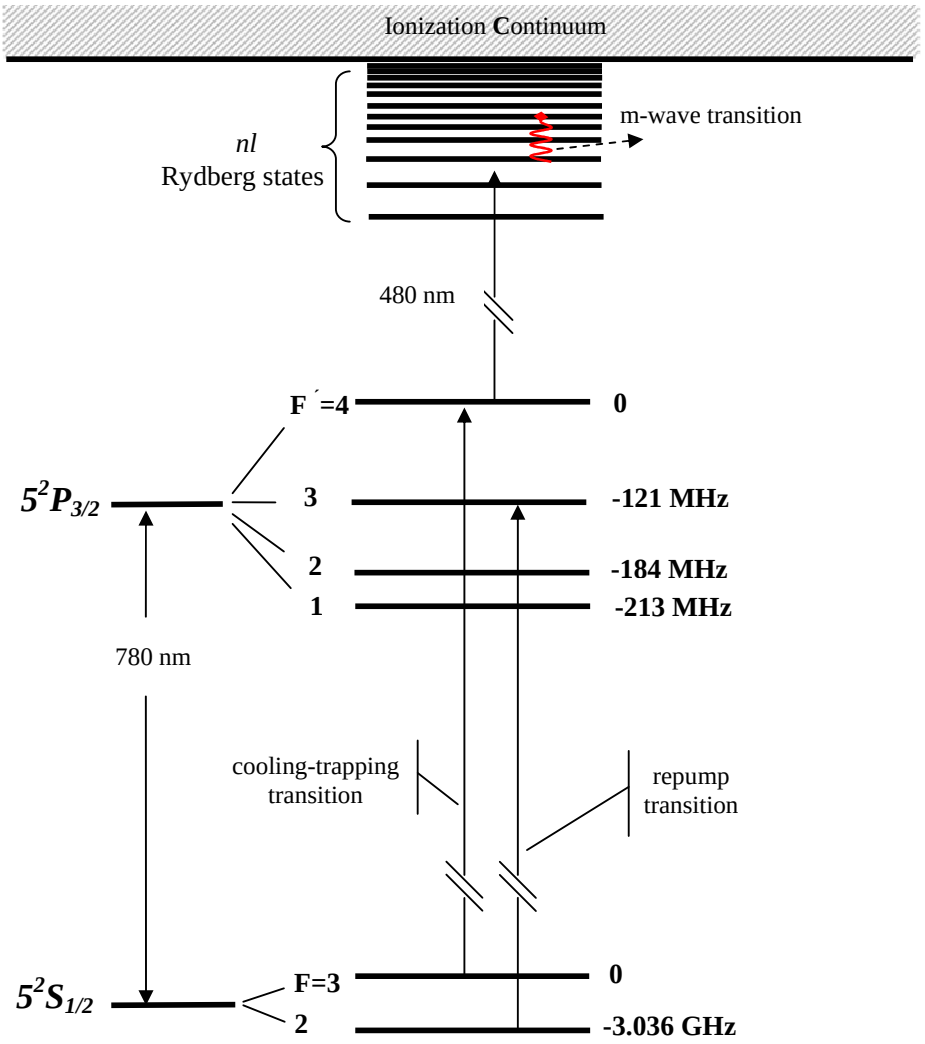

Figure 2.6: Excitation to Rydberg states of Rb using a two-colour two-photon process (not to scale).

most popular method of Rydberg atom detection in recent years and is especially suitable for atoms in states with large principal quantum numbers that require a low ionizing field [40].

If the energy shift of a Rydberg state in the presence of an electric field is ignored, then the classical field for ionization in terms of n (where n is the principal quantum number) is [1],

$$E = \frac{1}{16n^4}. \tag{2.2}$$

As soon as a field on this order is applied, the Rydberg atoms are ionized and the resultant ions or electrons can be accelerated towards and detected by a MCP detector. The binding energy of the Rydberg states depends on the principal quantum number, n, angular momentum, l, and also varies between different levels with different sublevels, m_l. Since the ionization threshold depends on the binding energy, the excited states can be detected selectively. In order to detect the initial and final states of a microwave transition such as $ns \rightarrow np$ simultaneously, a slowly rising pulse is used. The slowly rising pulse makes it possible to detect and resolve Rydberg states that have different binding energies. This detection method of Rydberg states is simple, sensitive and energy selective.

For the experiments described in this thesis, the selective field ionization pulse, required for the ionization of Rydberg atoms, is applied to one of the electric field plates shown in Fig. 2.7. There are three holes in each plate to let the cooling-trapping laser beams into the trap, and for trap imaging and ion/electron detection purposes (see Fig. 2.7).

By varying the electric field and ionizing the Rydberg state the resultant ions (or electrons) are pushed to the MCP detector. The output signal of the MCP is gated and averaged using boxcar integrators. The analogue time-averaged output signals of the boxcars are digitized by a 16-channel digitizer (National Instruments). A graph of the ionization pulse and the detected signals corresponding to two Rydberg states is shown in Fig. 2.8.

2.4 Using microwave transitions to compensate stray electric and magnetic fields

Due to the sensitivity of Rydberg atoms to external fields, stray fields can mix atomic energy levels and make it difficult, and sometimes impossible, to excite a

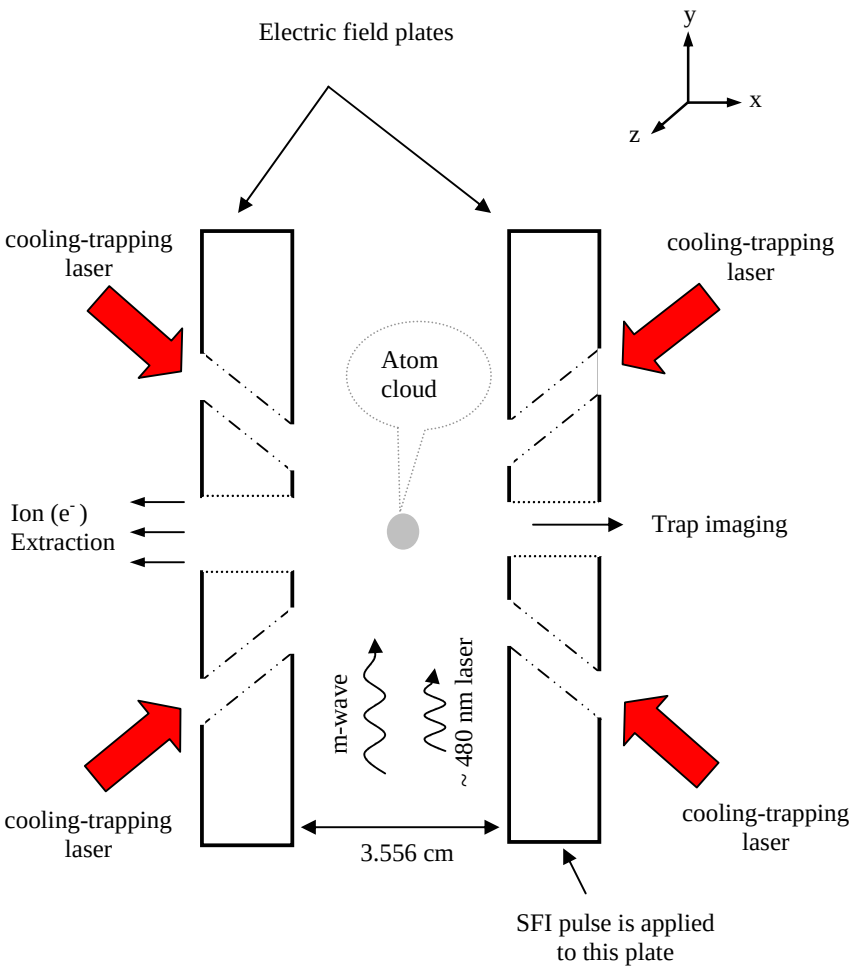

Figure 2.7: Schematic geometry of the electric field plates.

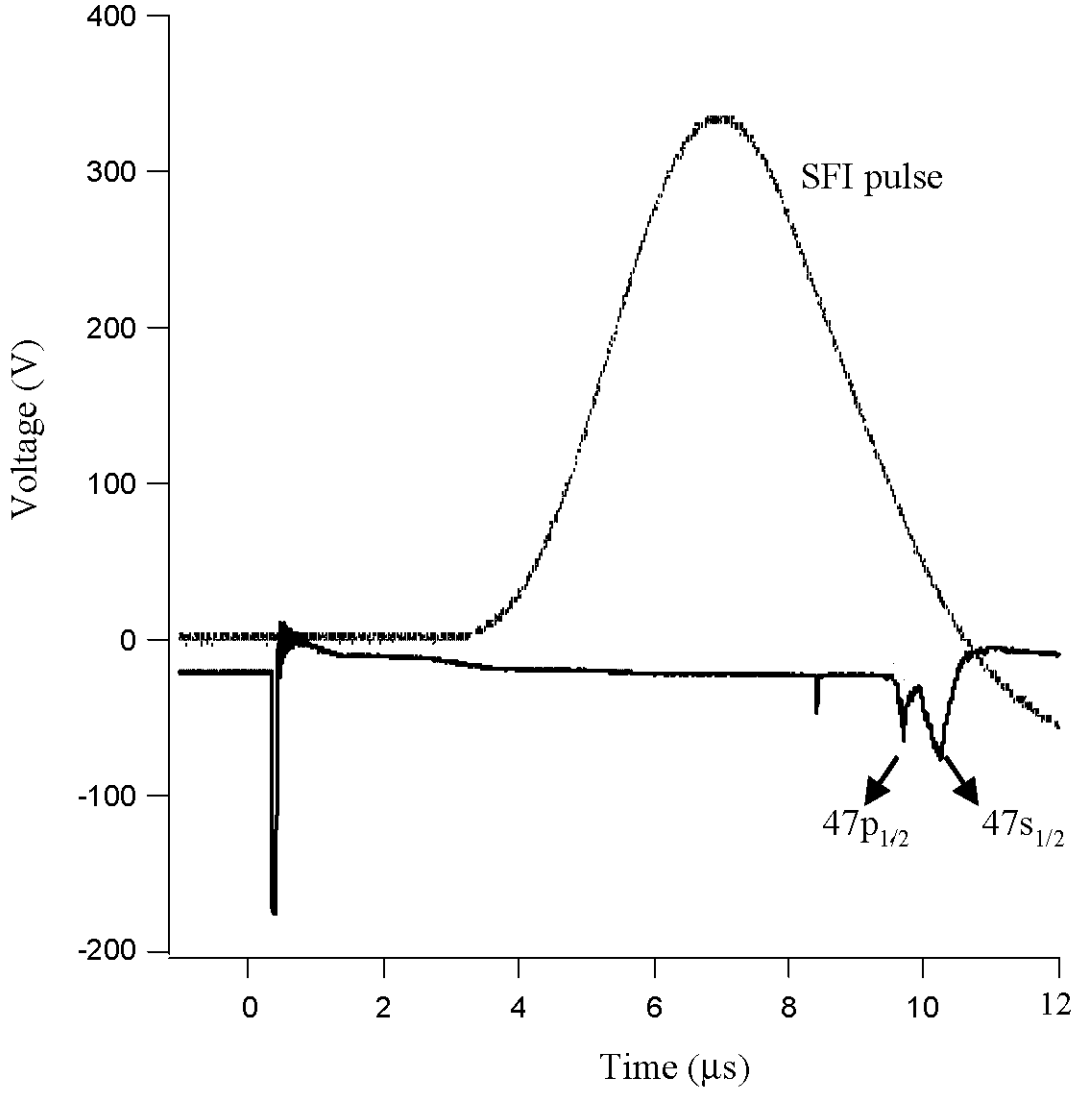

Figure 2.8: Traces of SFI signal and ion signals of $47s_{1/2}$ and $47p_{1/2}$ states observed on an oscilloscope. The large signal at $t \approx 0$ μs is due to the photoelectrons produced during the photoexcitation. The second signal at $t \approx 8.2$ μs is due to the ions produced by collisions of Rydberg atoms with other particles in the MOT. These ions appear early in time as they are free and are pushed to the MCP by a small electric field. Time is measured relative to the start of the 480 nm laser pulse. Microwaves are applied right after the optical excitation to excite atoms to the $47p_{1/2}$ Rydberg states. The SFI pulse is applied ≈ 3 μs after the optical excitation.

particular atomic level. In addition, stray fields broaden atomic transitions and reduce our sensitivity to detect physical phenomena. Therefore, it is important to zero out any unwanted stray external fields in the MOT. A brief explanation of the behavior of Rydberg atoms in electric and magnetic fields is presented in Ref. [36].

2.4.1 Magnetic field

Switching off the anti-Helmholtz coils (AHCs)

The inhomogeneous magnetic field strength necessary for the MOT operation depends on the AHCs' current. For an AHCs current of 9.5 A, cold atoms experience a magnetic field strength which varies between 0 and ≈1.2 G. The Zeeman shift of atomic energy levels is on the order of 1MHz /G. To avoid the line broadening due to the inhomogeneous magnetic field, it should be turned off before doing the experiments. We have to take into account that switching off the large AHCs current produces an induced magnetic field due to eddy currents. We need to wait for the eddy currents to die down to an appropriate level before we can conduct our experiments. Figure 2.9 shows how the magnetic field changes in the trap after turning the AHCs off. The AHCs current was brought to zero in approximately 1.7 ms. Based on the result of this measurement (Fig. 2.9), the inhomogeneous magnetic field, measured at the large fused silica window of the MOT (see Fig. 2.12), almost dropped to zero 25 ms after shutting the AHCs off.

Compensating stray magnetic fields using microwave transitions

The earth's magnetic field and an ion pump are two known sources of unwanted stray magnetic fields in our MOT. To calibrate magnetic fields, and compensate for stray fields, we use the one-photon $34s_{1/2} \rightarrow 34p_{1/2}$ microwave transition. Figure 2.10 shows the calculated Zeeman shifts of the corresponding states.

Figure 2.11 displays the $34s_{1/2} \rightarrow 34p_{1/2}$ microwave spectra taken with different dc magnetic fields. In general, line positions are dependent on the magnetic field and the hyperfine splitting of both the $34s_{1/2}$ and $34p_{1/2}$ states. However, there is a particular transition from $34s_{1/2}(m_F = -3)$ to $34p_{1/2}(m_F = -3)$ whose shift in position with magnetic field does not depend on the hyperfine spacing. This line is marked with arrows in Fig. 2.11. The transition energy for this line is $(2/3)\mu_B B$

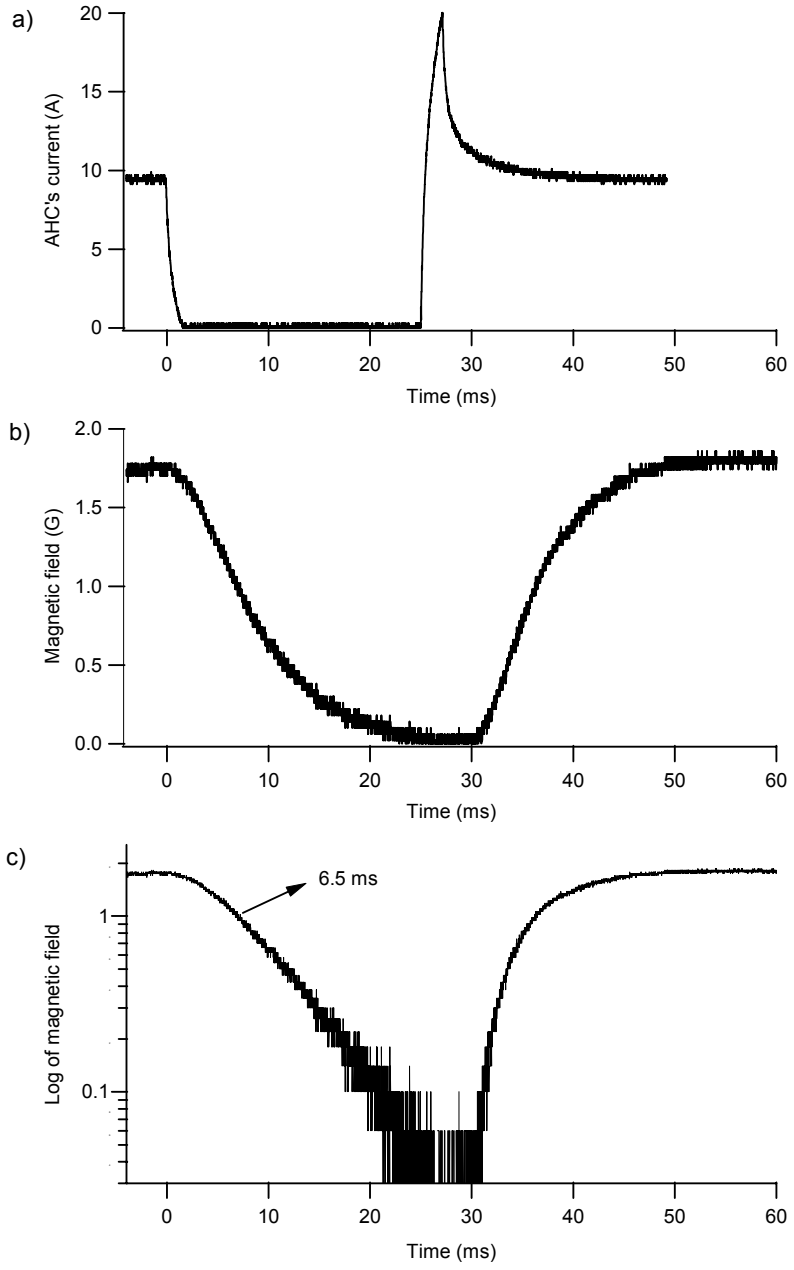

Figure 2.9: Inhomogeneous magnetic field falling off when the AHCs are turned off for 30 ms; a) AHCs current versus time, b) inhomogeneous magnetic field decay in time, and c) magnetic field decay in time (log-linear graph). Time is measured relative to the switching off of the AHCs (from Ref. [41]).

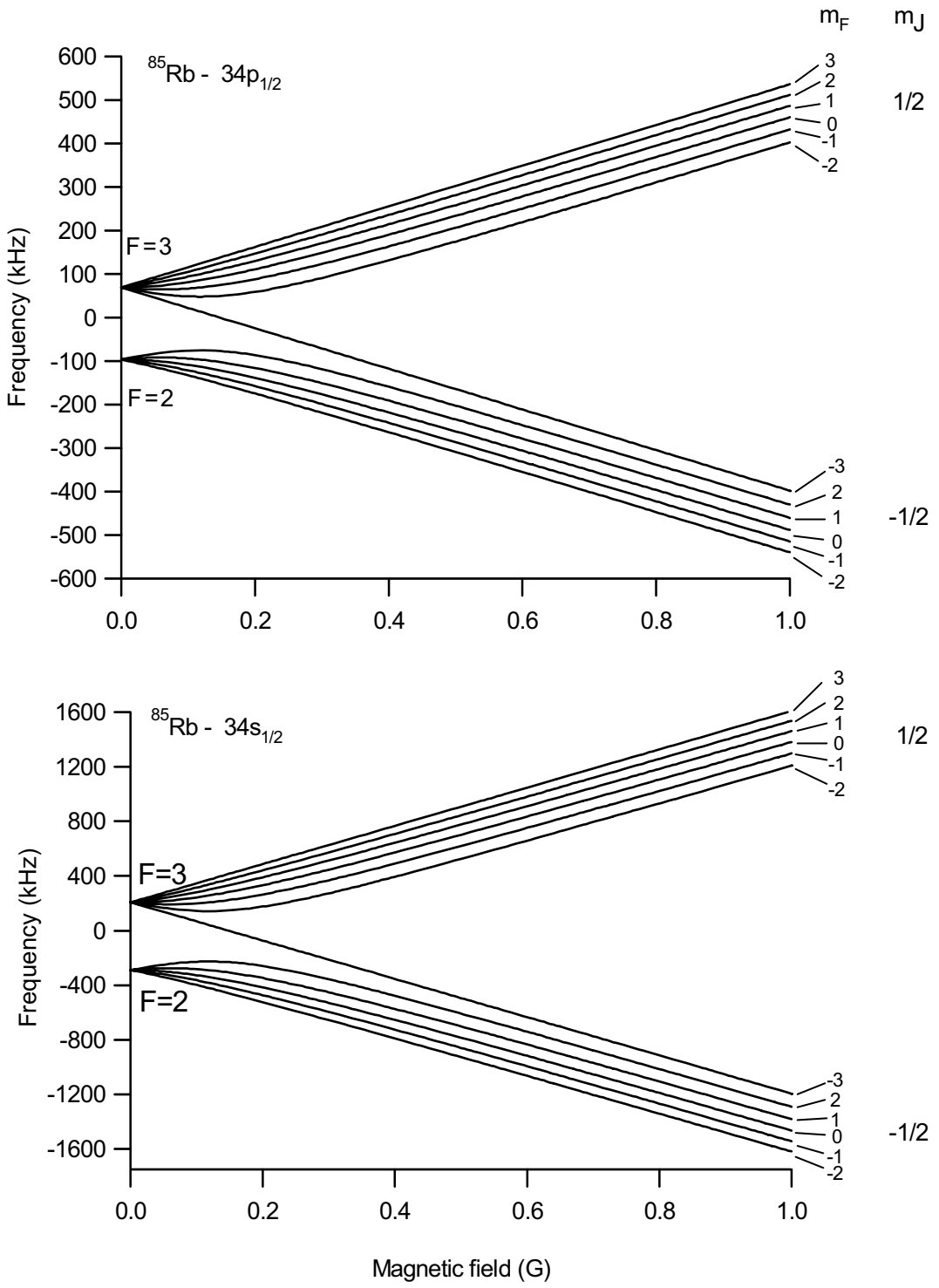

Figure 2.10: Calculated Zeeman splittings of the $34s_{1/2}$ and $34p_{1/2}$ energy levels of ^{85}Rb using the Breit-Rabi formulas [42]. The $34s_{1/2}(m_F = -3) \rightarrow 34p_{1/2}(m_F = -3)$ microwave transition is used for magnetic field calibration (from Ref. [43]).

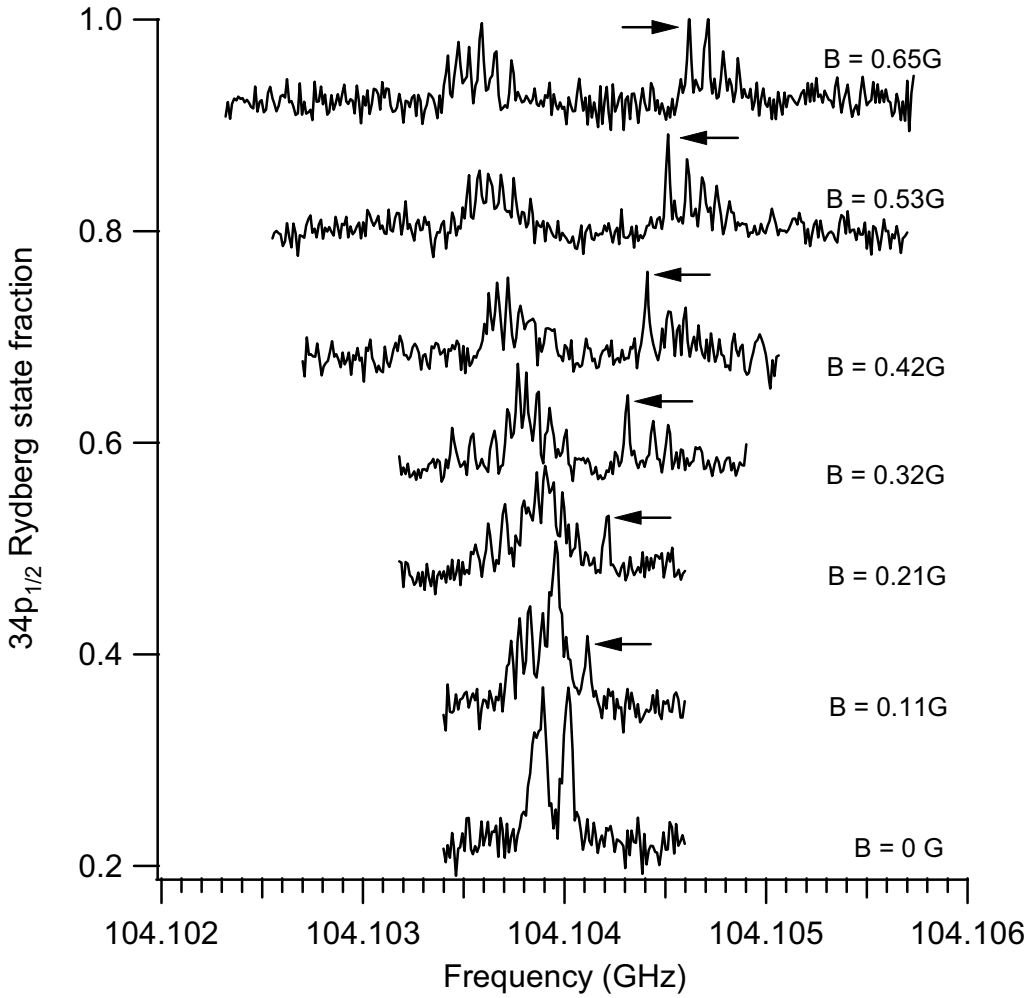

Figure 2.11: The ^{85}Rb $34s_{1/2} \rightarrow 34p_{1/2}$ microwave spectra in different dc magnetic fields. Spectra are offset vertically for clarity. The arrow labels the $34s_{1/2}(m_F = -3) \rightarrow 34p_{1/2}(m_F = -3)$ line, which is used for magnetic field calibration (from Ref. [43]).

[42], where μ_B is the Bohr magneton and B is the magnetic field. As shown in Fig. 2.11 this line is convenient as it is clearly identifiable in the spectra. To generate calibrated magnetic fields a pair of compensating coils of the MOT setup has been used. By tabulating the position of this spectral line as a function of coil current and fitting a straight line, the magnetic field as a function of coil current can be determined, without knowledge of the $34s_{1/2}$ hyperfine splitting. Using this method has made it possible to calibrate the homogeneous magnetic field within the MOT to an accuracy of ± 10 mG. The details of these procedures are presented in Ref. [43, 41]. At the time of the experiments presented in this work, the residual magnetic field inhomogeneity over the sample was less than 17 mG.

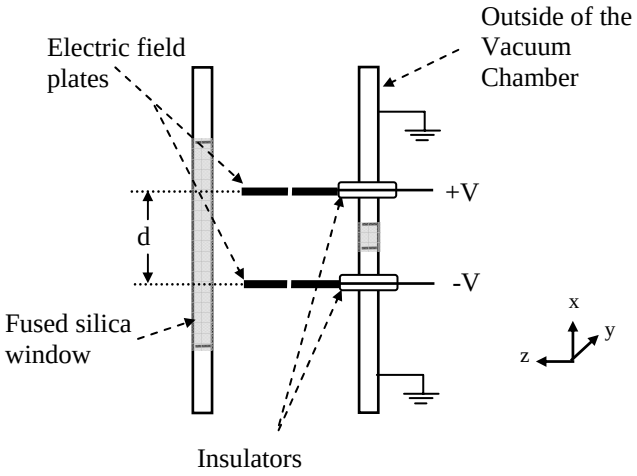

Figure 2.12: Schematic diagram of the connections for the electric field plates. They are near a grounded flange on one side and there is an insulating fused silica window on the other side. The separation of the plates is $d = 3.556$ cm. The Rb dispensers are attached to the chamber in y direction and are not shown in this diagram.

2.4.2 Electric field

As shown in Fig. 2.7 electric field plates are located on either side of the trapped atoms. By varying the voltages on these plates and the voltage of the Rb dispenser source with respect to the grounded chamber, it is possible to compensate the stray electric field in all three directions (see Figs. 2.3 and 2.12). The single-photon transition $34s_{1/2} \rightarrow 34p_{1/2}$ in ^{85}Rb is used for this purpose. This general procedure has been described in Ref. [10]. The electric field compensation process

is an iterative procedure that can be repeated indefinitely to get to a point where the stray E fields are minimized. We continue this process until the change in transition frequency of $34s_{1/2} \rightarrow 34p_{1/2}$ falls within the experimental error which in our case was 1kHz. The electric field corresponding to the frequency change of 1kHz is taken to be the upper bound of stray electric field in our setup, which is 10mV/cm. Once the stray electric field is compensated, the plate voltages may be used to produce deliberate fields. We calibrate these fields by observing the shifted transition frequencies and comparing them to the frequencies expected from a Stark map calculation [18].

Chapter 3

Optical transfer cavity stabilization using current-modulated injection-locked diode lasers

For precise excitation of Rb atoms to desired Rydberg states the frequency of the Ti:sapphire laser needed to be stablized. In the work presented in the following Chapter we addressed this issue by developing a general technique for laser frequency stabilization. This chapter is directly based on a paper published by the author together with K. Afrousheh and J. D. D. Martin [44].

3.1 Summary

It is demonstrated that RF current modulation of a frequency stabilized injection-locked diode laser allows the stabilization of an optical cavity to adjustable lengths, by variation of the RF frequency. This transfer cavity may be used to stabilize another laser at an arbitrary wavelength, in the absence of atomic or molecular transitions suitable for stabilization. Implementation involves equipment and techniques commonly used in laser cooling and trapping laboratories, and does not require electro- or acousto-optic modulators. With this technique we stabilize a transfer cavity using a RF current-modulated diode laser which is injection locked

to a 780 nm reference diode laser. The reference laser is stabilized using polarization spectroscopy in a Rb cell. A Ti:sapphire ring laser at 960 nm is locked to this transfer cavity and may be precisely scanned by varying the RF modulation frequency. We demonstrate the suitability of this system for the excitation of laser cooled Rb atoms to Rydberg states.

3.2 Background

It is often necessary to stabilize lasers at frequencies where direct locking to an atomic or molecular reference line is not possible. Several methods are commonly used for this purpose. One is to stabilize the target laser by comparison with a second laser (reference laser), which is stabilized to an absolute frequency reference such as an atomic or a molecular absorption line. If the frequency of the reference laser is sufficiently close to the frequency of the target laser, the two lasers may be heterodyned on a photodetector and the resulting beat note can be used to stabilize the target laser [38]. However, this is only practical up to a certain frequency difference due to the bandwidth of the photodetector.

An alternative technique is to use an optical cavity to "transfer" the stability from a stabilized reference laser to the target laser [45, 46, 47, 48, 49, 50, 51, 52]. One way this may be accomplished is by repetitively scanning the length of a "transfer cavity" (TC) with piezoelectric transducers (PZTs). The transmission fringe positions of the target laser are then compared to the reference laser using specialized digital circuitry [45] or computers [46, 47]. This comparison is used to derive an error signal which may be fed back to the target laser for stabilization. Using this technique, Zhao *et al.* [46] have demonstrated a long-term frequency drift on the order of 1 MHz. However, the scanning rate of the cavity puts a limit on the maximum rate of error correction. We have also found that this approach is sensitive to low frequency vibrations. The complexity of the fringe comparison is an additional drawback.

Scanning the cavity length may be avoided by making the transmission maxima of both the reference laser and the target laser coincide at the same cavity length [48, 49, 50, 51, 52]. In this case, the cavity is locked to the reference laser and the target laser is locked to the cavity using analog circuitry. To make the fringes coincide it is possible to frequency shift either the reference or the target laser using an electro-optic modulator (EOM) [48] or an acousto-optic modulator (AOM) [50, 52]. In

this way, frequency stability and precise RF frequency tunability can be obtained. Since, in general, frequency shifts on the order of the free spectral range of the cavity may be required, the modulator in these systems should be capable of producing a broad-band of frequency shifts in order to avoid an inconveniently long transfer cavity.

In this chapter, a technique for obtaining these frequency shifts that is inherently broadband and relatively easy to implement without using AOMs or EOMs is presented. A Fabry–Perot TC is stabilized using a tunable sideband from a current-modulated diode laser. The carrier of this slave laser is injection locked to a second diode laser (reference laser) [53] that is stabilized using an atomic reference. By adjusting the RF frequency of the current modulation of the injection locked slave laser, the TC may be tuned to the desired length for stabilization.

3.3 Experimental Setup

The stabilization scheme has been developed for a 960 nm commercial ring Ti:sapphire laser (Coherent MBR-110). This laser is frequency doubled in an external ring resonator (Coherent MBD-200) to produce approximately 70 mW at $\approx$ 480 nm, and used with 780 nm lasers to excite cold Rb atoms to Rydberg states [43]. Since frequency stabilized 780 nm lasers are required in our experiment to laser cool Rb atoms, they are convenient references for transfer cavity stabilization.

The locking procedure is as follows: The 960 nm laser is tuned by hand to the desired frequency by changing the internal cavity lenth of the 960 nm laser. The reference 780 nm laser is locked using polarization spectroscopy [33]. With the TC in scanning mode, injection locked operation of the slave laser is verified. RF current modulation is then applied to the slave laser, which produces two significant sidebands at f_m, the modulation frequency [53]. The RF modulation frequency is chosen so that a transmission peak of a 780 nm sideband coincides with a 960 nm transmission peak. Cavity ramping is then stopped and the cavity is locked to the 780 nm sideband transmission peak and the 960 nm laser is locked to its own transmission peak. The lock point of the 960 nm may be varied by changing the frequency of the slave laser current modulation, f_m.

Figure 3.1 illustrates the experimental setup. The reference laser is an external cavity, grating stabilized, diode laser (Toptica, DL100) operating at 780 nm with a

maximum output power of 150 mW and short term frequency stability of 1 MHz. The laser can be coarsely tuned by manually adjusting the grating angle, and fine-tuning is obtained using a PZT. The reference laser is frequency stabilized using polarization spectroscopy (PS) technique [33] in a Rb vapor cell. In this technique a strong circularly polarized pump beam induces a birefringence in a Rb cell to rotate the polarization axis of a linearly polarized probe beam. Observation of this rotation produces a dispersion-like signal which is used for frequency locking. A small fraction (10%) of the linearly polarized laser beam from the reference laser is diverted and divided into two beams. One is directed to the PS setup for frequency locking, and the other beam is used for Rb saturation absorption spectroscopy (SAS) [32], which serves as a frequency identifier. The rest of the reference laser output beam is coupled into a single mode fiber and the collimated output beam from this fiber is used to injection lock the slave laser.

The slave laser is a commercial 780 nm diode laser (Sanyo, DL7140-201S) in a temperature stabilized mount (Thorlabs, TCLDM9). Current modulation is applied using a bias-T, driven by a RF synthesizer (typically operated at 100-400 MHz, 18 dBm). The slave laser is coupled into a single mode fiber [path (b) in Fig. 3.1]. The output beam from the fiber is passed through a half wave plate and a polarizing beam splitter (PBS) to obtain a well-defined polarization. This beam is then fed into the TC, which may be temporarily operated as a scanning Fabry-Perot interferometer. A small fraction of the reference laser beam is also fed into the TC for verifying the injection locking [path(a) in Fig. 3.1].

Why not simply current-modulate the reference laser directly [54] and lock the cavity to one of the resulting sidebands? Although this will work in principle, there are a number of reasons to prefer the use of a current-modulated slave laser, despite the additional complexity. If the reference laser were directly modulated, the stability of its frequency lock would be compromised, particularly if the modulation frequency f_m were varied. In addition, by leaving the stabilized laser unmodulated, we can use part of its beam for other purposes. For example, in our experiment it is also used as a reference for beat-note locking [38, 30] the cooling-traping ECDL systems used for the MOT (see Fig. 2.5).

The TC is of the confocal Fabry-Perot type, consisting of two mirrors with radii of curvature $R = 9.18$ cm, separated by $L \approx R$ with a free spectral range of 817 MHz. It is desirable to have good finesse, thus good reflectivity at both 780 nm and 960 nm. It was possible to choose a standard dielectric mirror coating which exhibits high reflectivity at these two wavelengths (Newport, BD2). A PZT is

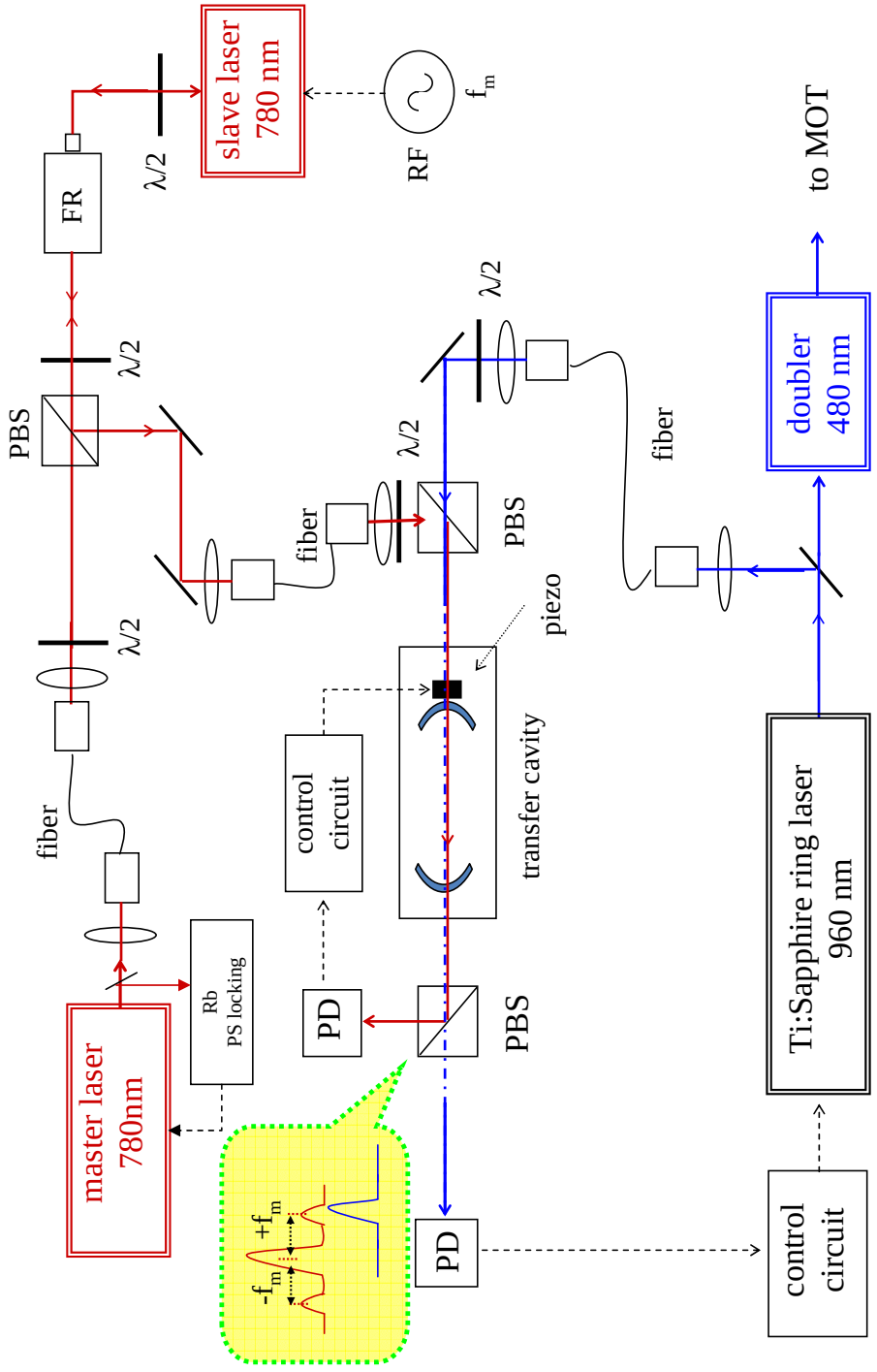

Figure 3.1: Experimental setup. PBS: polarizing beam splitter; PD: photodiode; FR: Faraday rotator; PS: polarization spectroscopy.

mounted on one of the end mirrors. The typical finesse of the TC is 100 and is limited by beam alignment and difficulty in obtaining the exact confocal condition.

A small fraction of the Ti:sapphire target laser beam is coupled into a single mode fiber. On emerging from the fiber, the light is passed through a PBS to ensure the beam is linearly polarized, and then aligned into the TC. After the orthogonally polarized 780 nm and 960 nm laser beams emerge from the TC, they are separated by a PBS and directed onto photodiodes.

The TC length is dithered slightly at 1.6 kHz using the PZT by an amplitude on the order of the cavity linewidth (10 MHz). Lock-in amplifiers are used to demodulate the transmission through the TC for both wavelengths [49, 51]. This provides a derivative-like lineshape error signal for locking the transmission maxima. The 780 nm error signal is used in an integrator feedback loop which adjusts cavity length using the PZT. This stabilizes the TC length. The 960 nm error signal is fed into another integrator control loop which uses the "Ext Lock" of the target laser control box to adjust the frequency. This "Ext Lock" control has a relatively low bandwidth ($f_{3dB} \approx 10$ Hz) [55]. However, this laser system is pre-stablized using a low-finesse cavity in a similar manner to the system described in Ref. [51].

3.4 Result

The tuning accuracy and the drift behavior of the frequency locked target laser is characterized using Rydberg atom excitation in a ^{85}Rb magneto-optical trap (MOT). The details of this apparatus appear elsewhere [27, 43].

The excitation of cold ^{85}Rb atoms to $46d$ Rydberg states occurs as a two-color process with nearly resonant 780 nm light ($5s_{1/2}$ - $5p_{3/2}$) and 480 nm light ($5p_{3/2}$ - $46d$). The 780 nm light is necessary for the ^{85}Rb MOT and is detuned 12 MHz to the red of the $5s_{1/2}$ F=3 to $5p_{3/2}$ F=4 transition. The 480 nm light is obtained by frequency doubling the output of a 960 nm Ti:sapphire ring laser – the target laser for our stabilization scheme.

The 780 nm cooling and trapping light remains on continuously. The 480 nm light is pulsed on for 1μs using an acousto-optic modulator. A pulsed electric field is then applied to field-ionize any Rydberg atoms and draw the resulting ions to a microchannel plate detector (MCP). A boxcar integrator is used to gate on the signal. The excitation and detection sequence repeat at 10 Hz.

When the 960 nm target laser is locked using the scheme described in the previous section, its output frequency may be scanned by varying the RF modulation frequency f_m. Figure 3.2 shows the resulting spectrum in the range of the ^{85}Rb $5p_{3/2}$ - $46d_{3/2}$ and $5p_{3/2}$ - $46d_{5/2}$ transitions. The strong 780 nm field is responsible for the splitting of the lines into doublets. This is the Autler-Townes effect [56, 57], similar to the results presented in Ref. [58].

We expect the target laser frequency shift Δf_t to be related to the slave laser modulation frequency shift Δf_m by

$$\Delta f_t = \frac{\lambda_{r,air}}{\lambda_{t,air}} \Delta f_m, \tag{3.1}$$

where $\lambda_{r,air}$ and $\lambda_{t,air}$ are the air wavelengths of the reference laser and the target laser. In our case, the frequencies of the reference and target lasers are well-known, but we must estimate the corresponding refractive indices to determine the air wavelengths. Equation (3.1) can be tested using the observed separation of the (β) and (δ) peaks in Fig. 3.2, together with the known $46d_{3/2}$ - $46d_{5/2}$ energy separation [9]. As shown in Fig. 3.2, the Autler-Townes splitting of $46d_{3/2}$ and $46d_{5/2}$ lines are identical and thus we do not expect these to contribute to the separation of the (β) and (δ) peaks. As illustrated in Fig. 3.2 (b), the frequency of modulation, Δf_m, has to be varied by 75 MHz to move from (β) to (δ). This corresponds to a target laser frequency change of $\Delta f_t \approx 60$ MHz. We find $\Delta f_t / \Delta f_m = (0.80 \pm 0.015)$, compared to Eq. (3.1), which predicts $\Delta f_t / \Delta f_m = 0.812$.

By repetitively scanning over the spectrum shown in Fig. 3.2 and recording the peak positions, we can monitor the frequency drift of the locked target laser. The positions of the (α) and (γ) peaks are less dependent on the frequency fluctuations of the 780 nm cooling laser than the (β) and (δ) peaks. Therefore, the stronger (γ) line is used to quantify the stability of the target laser. With the locking system activated, the control voltage applied to the Ti:sapphire laser varies as time progresses. Since the approximate relationship between a change in the control voltage and the corresponding change in the output frequency is known, we can use this to estimate the frequency drift that would have occurred if the laser were not stabilized. Figure 3.3 is a comparison between (a) the estimated unlocked and (b) the locked frequency drifts over ≈ 1 hr. There is a dramatic reduction in the long-term frequency drift when the laser is locked.

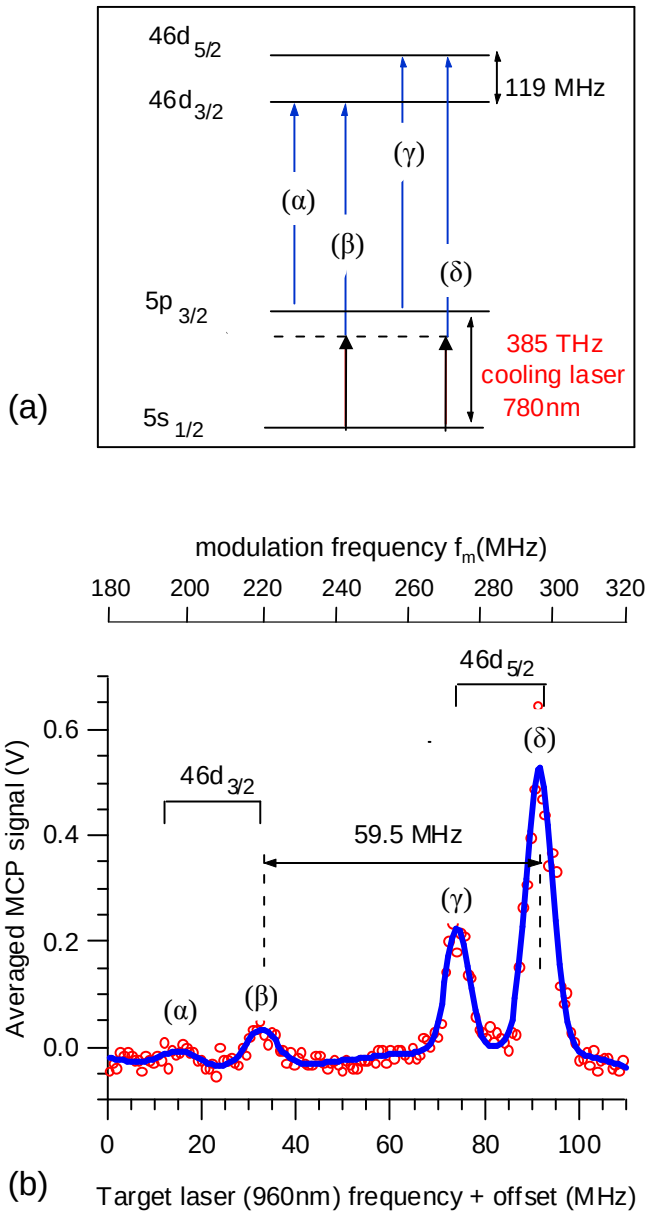

Figure 3.2: (a) Energy level diagram (b) Spectrum of ^{85}Rb $5p_{3/2}$ to $46d_{3/2}$ and $46d_{5/2}$ Rydberg state transitions obtained by scanning the RF modulation frequency f_m. The lower horizontal axis is obtained from Eq. 3.1. The observed peaks correspond to the labeled transitions shown in part (a). Autler-Townes splitting of the transitions is observed due to the presence of 780 nm cooling laser [56, 58]. With the red-detuning of the 780 nm light (for MOT operation), the (β) and (δ) peaks may be roughly understood as corresponding to 2-photon absorption from the $5s_{1/2}$ ground state, whereas the (α) and (γ) peaks arise from step-wise excitation through the $5p_{3/2}$ state [57].

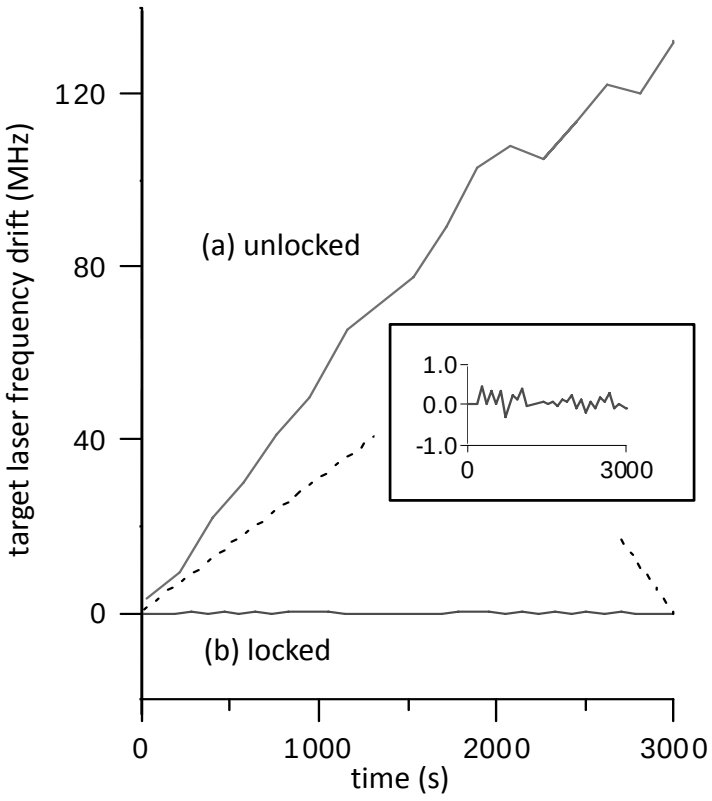

Figure 3.3: Frequency drift of the target laser system (Ti:sapphire, 960 nm) as a function of time under (a) unlocked and (b) locked conditions. The vertical scale of the trace (b) is enlarged on the inset.

3.5 Performance limitations

Since the TC is not evacuated, it is limited in performance by variations in the refractive indices of air for the target laser and the reference laser wavelengths, n_t and n_r respectively. The environmental influences on the locked target laser frequency can be approximated using:

$$\frac{\partial f_t}{\partial \alpha} = \left[\frac{(\partial n_r/\partial \alpha) n_t - (\partial n_t/\partial \alpha) n_r}{(n_t)^2} \right] \frac{n_t}{n_r} f_t, \tag{3.2}$$

where f_t is the target laser frequency and α represents an environmental parameter such as pressure, temperature, or humidity. The resulting sensitivities are tabulated in Table 3.1.

Figure 3.4 illustrates the frequency drift of the locked target laser as a function of time collected at various time over several months. From nine such data sets we observed an average long term (≈ 1 h) frequency drift of -0.141 ± 0.90 MHz/h. This is consistent with the typical variation of environmental parameters listed in Table 3.1. Thus, we expect that the frequency stability of the target laser will be improved if the TC is evacuated to minimize the environmental effects.

Ultimate long-term stability is also limited by the frequency drift of the reference laser. The reference laser is frequency stabilized using polarization spectroscopy (PS) in a Rb vapor cell [33]. To observe the drift of this laser we have monitored the beat note between this laser and a 780 nm laser stabilized using saturated absorption spectroscopy with third-harmonic lock-in detection. The relative drift of these two systems was typically less than 100 kHz/hr. We have found polarization spectroscopy locking to be a good compromise between several factors, including long-term stability, robustness and complexity. However, if necessary, less long-term reference laser drift could be obtained using alternative techniques [61, 62, 63].

Table 3.1: Frequency sensitivity of the locked target laser to environmental conditions for $\lambda_{\mathrm{t,vac}} = 960$ nm, $\lambda_{\mathrm{r,vac}} = 780$ nm, $P = 760$ torr, $T = 20\,^{\circ}$C, RH = 50% and $CO_2 = 450$ ppm. To evaluate Eq. 3.2, we used the NIST refractive index calculation program [59], which is based on the Ciddor equation [60].

α	$\partial f_t/\partial \alpha$
Pressure	350 kHz/torr
Temperature	-850 kHz/°C
Relative Humidity	19 kHz/ %

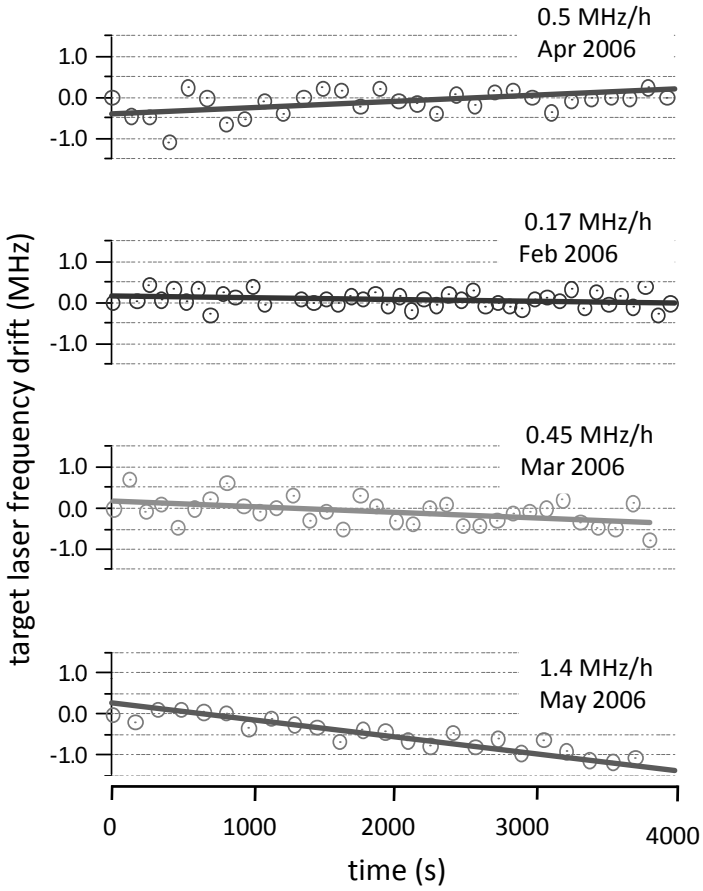

Figure 3.4: Frequency drift of the locked target laser system (Ti:sapphire, 960 nm) for several time periods over a few months.

It is essential to be able to vary the TC length over several free spectral ranges. This is to ensure that the slave laser sideband and 960 nm transmission peaks are well removed from the carrier transmission, which is stronger and may interfere with cavity locking to the sideband. This requires a long-extension PZT, which limits the bandwidth of the cavity lock and consequently the target laser lock. An improved system could use a fast short extension PZT on one end-mirror and a slower long extension PZT on the other end-mirror. The fast PZT would be used for dithering and fast cavity stabilization, whereas the slow PZT would handle long-term drift [64]. With these improvements it is expected that the bandwidth of the error signal would be sufficient to directly stabilize external cavity diode lasers for many applications.

3.6 Conclusion

In this Chapter, we report a general technique for laser frequency stabilization at arbitrary wavelengths using a reference laser and transfer cavity. A target laser frequency drift of < 1 MHz/hr has been demonstrated. The equipment involved is commonly used in laser cooling and trapping laboratories, and does not require special modulators and drivers. A controllable frequency source is required, but this is the same as for electro- or acousto-optic modulators. If precise RF scanning is not required, the RF synthesizer could be replaced by inexpensive voltage controlled oscillators, as in Ref. [53]. The achieved frequency stability for 960 nm Ti:sapphire laser ensured a reliable excitation of Rb atoms to Rydberg states for the experiments performed in this thesis work.

Chapter 4

Determination of the ^{85}Rb ng-series quantum defect by electric-field-induced resonant energy transfer between cold Rydberg atoms

Resonant energy transfer between cold Rydberg atoms using a dc electric field is the subject of research in the following chapter. This chapter is directly based on a paper published by the author together with K. Afrousheh, J. A. Petrus, and J. D. D. Martin [65].

4.1 Summary

Resonant energy transfer between cold Rydberg atoms was used to determine Rydberg atom energy levels, at precisions approaching those obtainable in microwave spectroscopy. Laser cooled ^{85}Rb atoms from a magneto-optical trap were optically excited to $32d_{5/2}$ Rydberg states. The two-atom process $32d_{5/2} + 32d_{5/2} \rightarrow 34p_{3/2} + 30g$ is resonant at an electric field of approximately 0.3 V/cm. This process is driven by the electric dipole-dipole interaction, which is allowed due to the partial f character that the g state acquires in an electric field. The experimentally

observed resonant field, together with the Stark map calculation is used to make a determination of the ^{85}Rb ng-series quantum defect: $\delta_g(n = 30) = 0.00405(6)$.

4.2 Introduction

Energy can be transferred more rapidly between two atoms when the process is *resonant*: one atom gives its energy to another, without a change in the kinetic energy of either atom. Although resonant energy transfer often relies on serendipity, the large Stark shifts of Rydberg atoms may allow the resonant condition to be exactly satisfied by application of an electric field [16]. The resonant energy transfer process between Rydberg atoms is driven by the electric dipole-dipole interaction. Transition dipole moments between nearby Rydberg states can be large, typically scaling as n^2, where n is the principal quantum number [1]. As a consequence, resonant energy transfer collision cross-sections scale as n^4, and are large compared to typical collision cross-sections for less excited atoms – usually by many orders of magnitude [1, 16].

Stoneman *et al.* [66] pointed out that the fields at which resonant energy transfer occurs may – under certain conditions – be used for precise Rydberg energy level spectroscopy. They examined the resonant energy transfer process: $29s + 29d \rightarrow 29p + 28p$, in potassium. Since the shifts of the Rydberg energy levels with field are relatively well-understood, they were able to use the resonance fields to determine improved values for zero field atomic energy levels. In particular, they determined a substantially more precise value for the quantum defect of the np-series of potassium.

The range of electric fields or "width" over which significant resonant energy transfer can be observed is important in this type of experiment, as it dictates the precision to which line centers can be determined. By reducing the spread in the velocity distribution of their sample Stoneman *et al.* [66] were able to significantly narrow the width of their observed resonances.

With the development of laser cooling, Rydberg atom samples with much narrower velocity distributions could be studied [23, 24]. In general, the resulting narrowness of the resonant energy transfer resonances has not been exploited for spectroscopic purposes. Instead, work has concentrated on the dynamical aspects of resonant energy transfer between cold Rydberg atoms. For example, Carroll *et*

al. [67] have recently studied how the relative orientation of the electric field with respect to the spatial orientation of two Rydberg atoms influences their dipole-dipole interaction. They used cold Rb atoms obtained from a magneto-optical trap (MOT) to study the process: $32d + 32d \rightarrow 34p + 30k$, where $30k$ represents the Stark-states centered around $n = 30$. The Stark states are superpositions of high angular momentum states ($l \geq 4$ in this case) exhibiting energy shifts which are linear in the applied electric field strength. Strong resonant energy transfer was observed between 1 to 6 V/cm, and was fully explained by a Stark map calculation, which took into account the energy shifts of the participating atoms. However, a series of peaks at approximately 0.5 V/cm were not reproduced in the calculations (these peaks were not relevant to the main point of their paper).

In this paper we demonstrate that the resonances observed at low field are due to the process:

$$32d + 32d \rightarrow 34p_{3/2} + 30g \tag{4.1}$$

which is an allowed electric dipole-dipole interaction, due to the f character that the g state acquires in the electric field. In the spirit of the work of Stoneman *et al.* [66] we use the observed resonant fields together with a Stark map calculation to determine the ng-series quantum defect.

Han *et al.* [68] have reported a preliminary observation of two-photon $(n+2)d-ng$ microwave transitions in ^{85}Rb. However, we are unaware of any other work on the ng Rydberg series of Rb.

4.3 Experiment

The essence of the experiment is to measure the electric fields required for efficient resonant energy transfer between cold $32d_{5/2}$ ^{85}Rb atoms. Some details of our apparatus have been previously described [43]. A standard vapor cell MOT is used as the source of cold ^{85}Rb atoms. These atoms are excited to $32d_{5/2}$ Rydberg states using a two-photon, two-color process with 480 nm light, and the nearly resonant, red-detuned 780 nm light used for cooling and trapping. The 480 nm light is obtained by frequency doubling a 960 nm cw ring Ti:sapphire laser, which is frequency stabilized using the technique described in Chp. 3. The experiment is done at a 10 Hz repetition rate, with an acousto-optic modulator used to produce pulses of light.

For energy level determination from resonant energy transfer spectroscopy it is critical to zero out any stray electric fields, and then be able to apply accurately known electric fields. Two stainless steel electrode plates, separated by 36 mm, are located to either side of the trapped atoms. By varying the voltages on these plates and the voltage of the Rb dispenser source (see Fig. 2.3) with respect to the grounded chamber, it is possible to compensate the stray electric field in all three directions. The single-photon transition $48s_{1/2} - 48p_{1/2}$ in ^{85}Rb is used for this purpose. This general procedure has been described by Osterwalder and Merkt [10]. Since the single photon transition is sensitive to magnetic fields, the inhomogeneous magnetic field necessary for MOT operation is shut-off prior to photoexcitation to Rydberg states. At the time of the experiment the residual magnetic field inhomogeneity over the sample is less than 17 mG. The details of this shutting off procedure are presented in Ref. [43].

Once the stray electric field is compensated, the plate voltages may be used to produce deliberate fields. We calibrate these fields by observing the shifted frequencies of the $48s_{1/2} - 48p_{1/2}$ transition and comparing them to the frequencies expected from a Stark map calculation [18]. The Stark map calculation uses the most recent quantum defect data for ^{85}Rb [9, 68]. Although quantum defects for $\ell > 3$ are not known, these do not significantly influence the calculated transition frequencies.

To observe resonant energy transfer between Rydberg atoms with known electric fields, we produce the fields in exactly the same way as during calibration using the $48s_{1/2} - 48p_{1/2}$ transition. The inhomogeneous magnetic field is also shut-off in an identical manner. After a light excitation pulse of 1 μs duration, the electric field is ramped from zero to the desired value in 160 ns. The atoms may interact during a waiting period of 21 μs. The typical experimental sequence for a single shot is shown in Fig. 4.1.

Final Rydberg state populations after the waiting period are analyzed by selective field ionization (SFI) [1]. In this case SFI is only able to distinguish states differing by energies equivalent to a change of approximately one principal quantum number. The $34p$ Rydberg states are ionized at a lower field than both the $32d_{5/2}$ initial states and $30g, k$ final states. By changing the applied electric field and recording the $34p$ population, resonant energy transfer spectra may be obtained (see Fig. 4.2(a)). For comparison we have also recorded analogous spectra at one lower n (Fig. 4.3(a)) and one higher n (Fig. 4.4(a)).

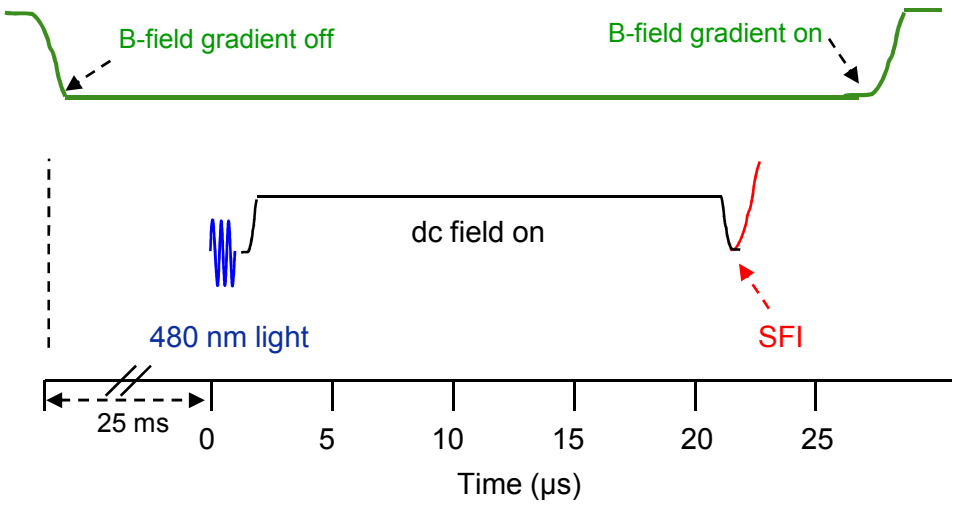

Figure 4.1: Timing diagram for dc electric-field-induced RET experiments. This sequence is repeated at 10 Hz.

4.4 Analysis

The striking difference in the three spectra presented in Figs. 4.2, 4.3, and 4.4 is the presence of the low-field resonances in the $32d_{5/2}$ case, but not in the others. Carroll *et al.* have also observed similar resonances in $32d$ (Ref. [67]), but not for $31d$ (Ref. [69]). Energetics [9, 68] rule out the process: $32d_{5/2} + 32d_{5/2} \rightarrow 34p_{3/2} + 30f$ as a possible explanation for these low-field resonances. The final state $34p_{3/2}+30f$ is at an energy less than the initial state in zero electric field, and this difference increases with increasing field, due to the f state polarizability.

There are no processes involving the well-characterized low-angular momentum Rydberg states ($\ell \leq 3$) of Rb which would account for the low field resonances in Fig. 4.2(a). We need to consider higher angular momentum states. The non-penetrating high angular momentum states of Rydberg atoms have quantum defects which scale like $1/\ell^5$ (see, for example, Ref. [1]). Thus a rough estimate of the ng-series quantum defect may be obtained from the nf-series quantum defect [68]:

$$\delta_g \approx \delta_f (3/4)^5 \approx 0.004. \tag{4.2}$$

A preliminary calculation with this estimated quantum defect shows that a resonance will occur for the process: $32d_{5/2}(m_j = 1/2) + 32d_{5/2}(m_j = 1/2) \rightarrow 34p_{3/2}(m_j = 1/2) + 30g_{7/2}(m_j = 1/2)$ at an electric field of 0.31 V/cm. This is very close to the

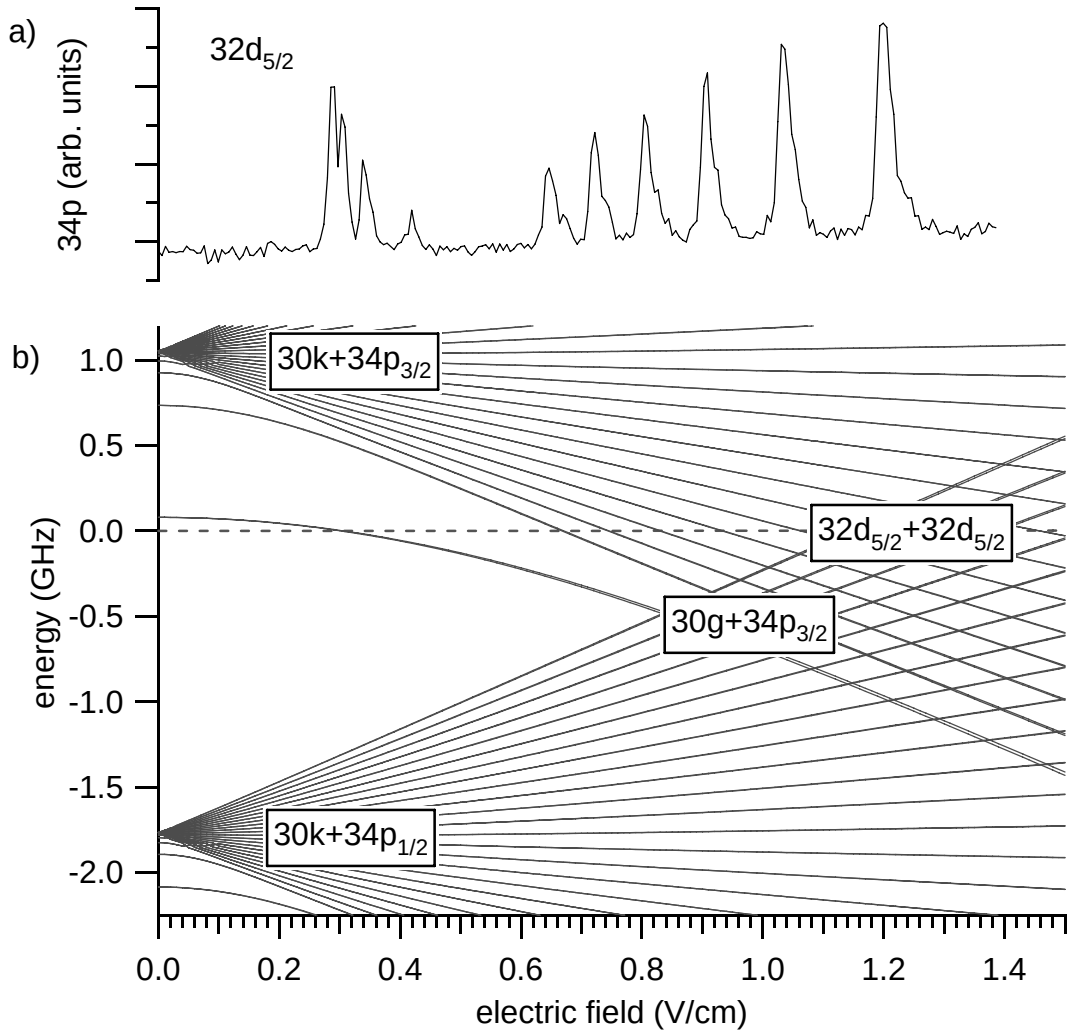

Figure 4.2: (a) Resonant energy transfer spectrum with atoms initially in the $32d_{5/2}$ state. (b) Calculated total energy of several two atom states, relative to the zero field energy of $nd_{5/2} + nd_{5/2}$ where $n = 32$. The calculations follow the procedures of Zimmerman *et al.* [18], using $\delta_g = 0.004$ and for $\ell > 4$, $\delta_\ell = \delta_g(4/\ell)^5$.

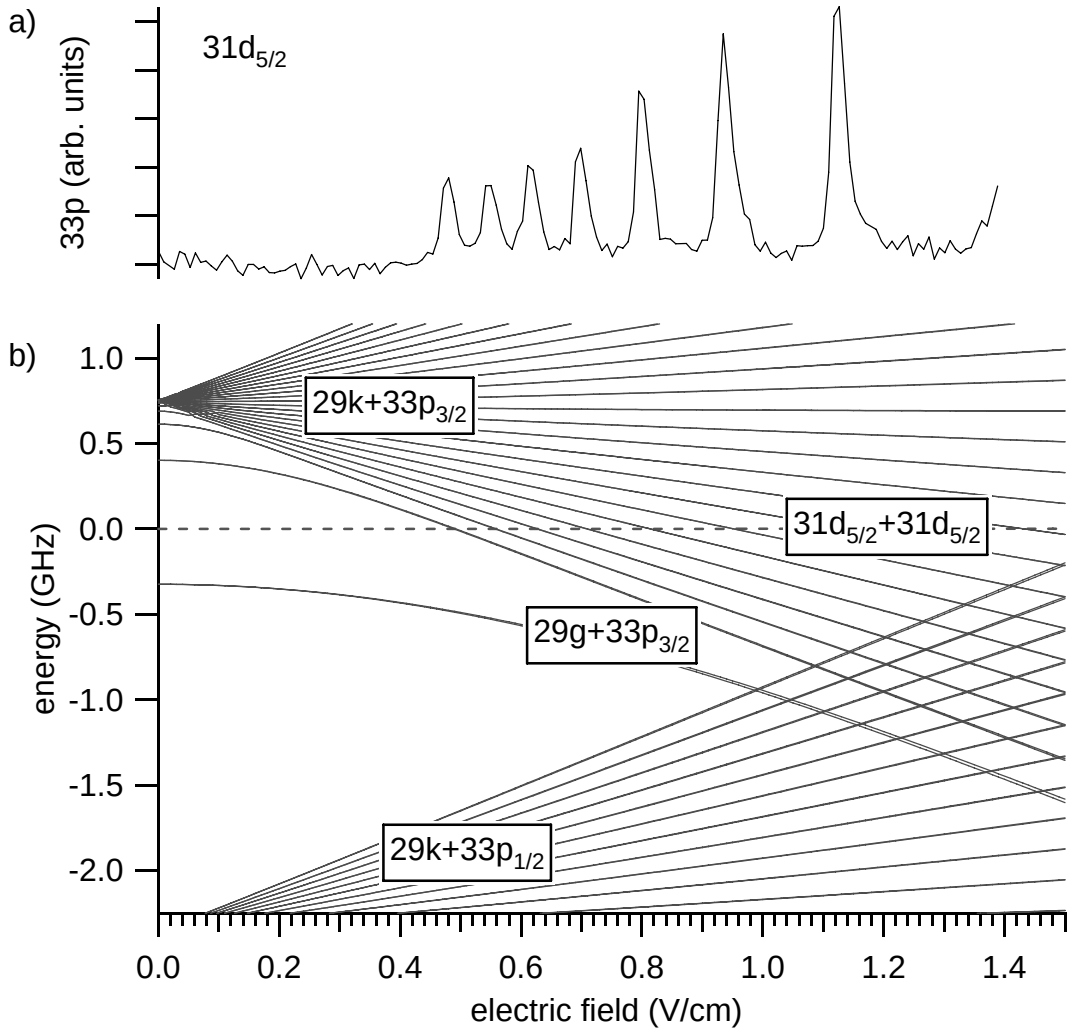

Figure 4.3: (a) Resonant energy transfer spectrum with atoms initially in the $31d_{5/2}$ state. (b) Calculated total energy of several two atom states, relative to the zero field energy of $nd_{5/2} + nd_{5/2}$ where $n = 31$. The calculations follow the procedures of Zimmerman *et al.* [18], using $\delta_g = 0.004$ and for $\ell > 4$, $\delta_\ell = \delta_g(4/\ell)^5$.

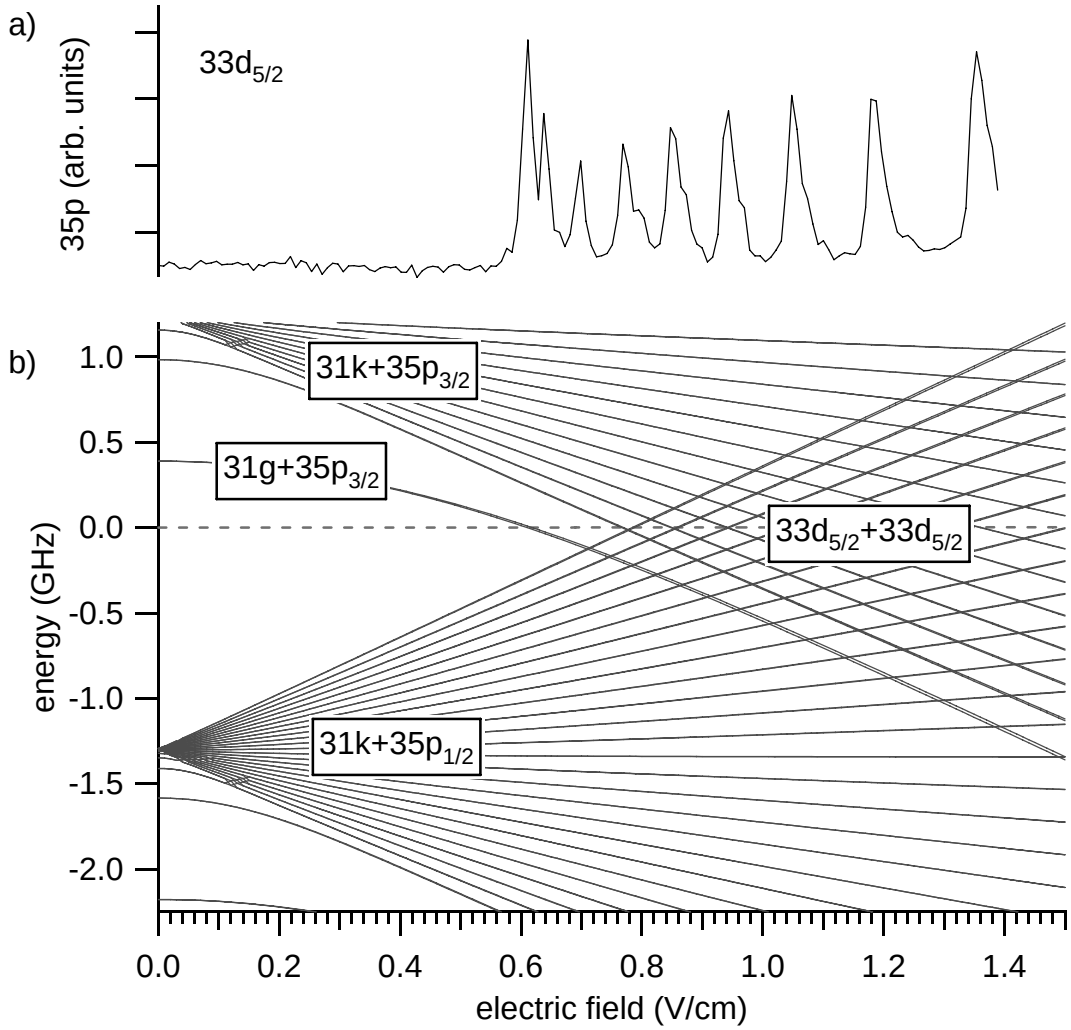

Figure 4.4: (a) Resonant energy transfer spectrum with atoms initially in the $33d_{5/2}$ state. (b) Calculated total energy of several two atom states, relative to the zero field energy of $nd_{5/2} + nd_{5/2}$ where $n = 33$. The calculations follow the procedures of Zimmerman *et al.* [18], using $\delta_g = 0.004$ and for $\ell > 4$, $\delta_\ell = \delta_g(4/\ell)^5$.

lowest field resonance observed in Fig. 4.2(a). However for the $31d_{5/2}$ case, the energy of the two-atom state $33p_{3/2} + 29g$ is less than the initial state $31d_{5/2} + 31d_{5/2}$, and this difference increases with increasing field (see Fig. 4.3(b)). This is consistent with the lack of observed low-field resonances in the $31d_{5/2}$ spectrum (Fig. 4.3(a)).

In the case of the $33d_{5/2}$, the electric field does shift $35p_{3/2} + 31g$ closer in energy to $33d_{5/2} + 33d_{5/2}$. However, the $31g$ state reaches the $n = 31$ Stark manifold at approximately the same field (Fig. 4.4(b)). This is consistent with the experimental observations in Fig. 4.4(a).

The calculations in Figs. 4.2(b), 4.3(b), and 4.4(b) consider only $m_j = 1/2$ magnetic sublevels. However, electric fields break the magnetic sublevel energy degeneracy; therefore, there should be different resonance fields corresponding to the different possible magnetic sublevels for the states in Eq. 4.1. The largest splittings are due to the magnetic sublevels of $30g$. The four peaks observed at low fields in Fig. 4.2(a) correspond to $m_\ell = 0$, 1, 2, 3, and 4 (the $m_\ell = 0$ and 1 resonances are unresolved). The splittings due to the magnetic sublevels of the other states are much less than the widths of each of these four peaks. Similarly, the three peaks observed between 0.6 and 0.7 V/cm in Fig. 4.4(a) correspond to the magnetic sublevels of $31g$.

All four observable resonances should be explainable by the same ng-series quantum defect (δ_g). Figure 4.5(a) illustrates calculated resonance fields as a function of a variable δ_g, centered around the estimated $\delta_g \approx 0.004$ (see Eq. 4.2). As illustrated in Fig. 4.5, all four resonances are consistent with the same quantum defect, to better than the widths of the resonances. We consider this as strong evidence that the process in Eq. 4.1 is the explanation for the low field resonances.

As Fig. 4.5 suggests, we can extract an estimate of the quantum defect from each one of these four resonances. The uncertainty may also be estimated for each of these experimentally determined quantum defects from the derivatives $\partial\delta_g/\partial F$ evaluated at the estimated quantum defects (where F is the electric field strength). The electric field zeroing and calibration procedure is estimated to have a 1σ uncertainty of less than 30 mV/cm at the resonance fields. From the four resonances we determine $\delta_g(n = 30) = 0.00405(6)$, which is consistent with a preliminary report of $\delta_g = 0.00400(9)$ from Han *et al.* [68].

As demonstrated, energetics strongly support Eq. 4.1 as the explanation for the low-field resonances. However, what drives this process? Resonant energy transfer

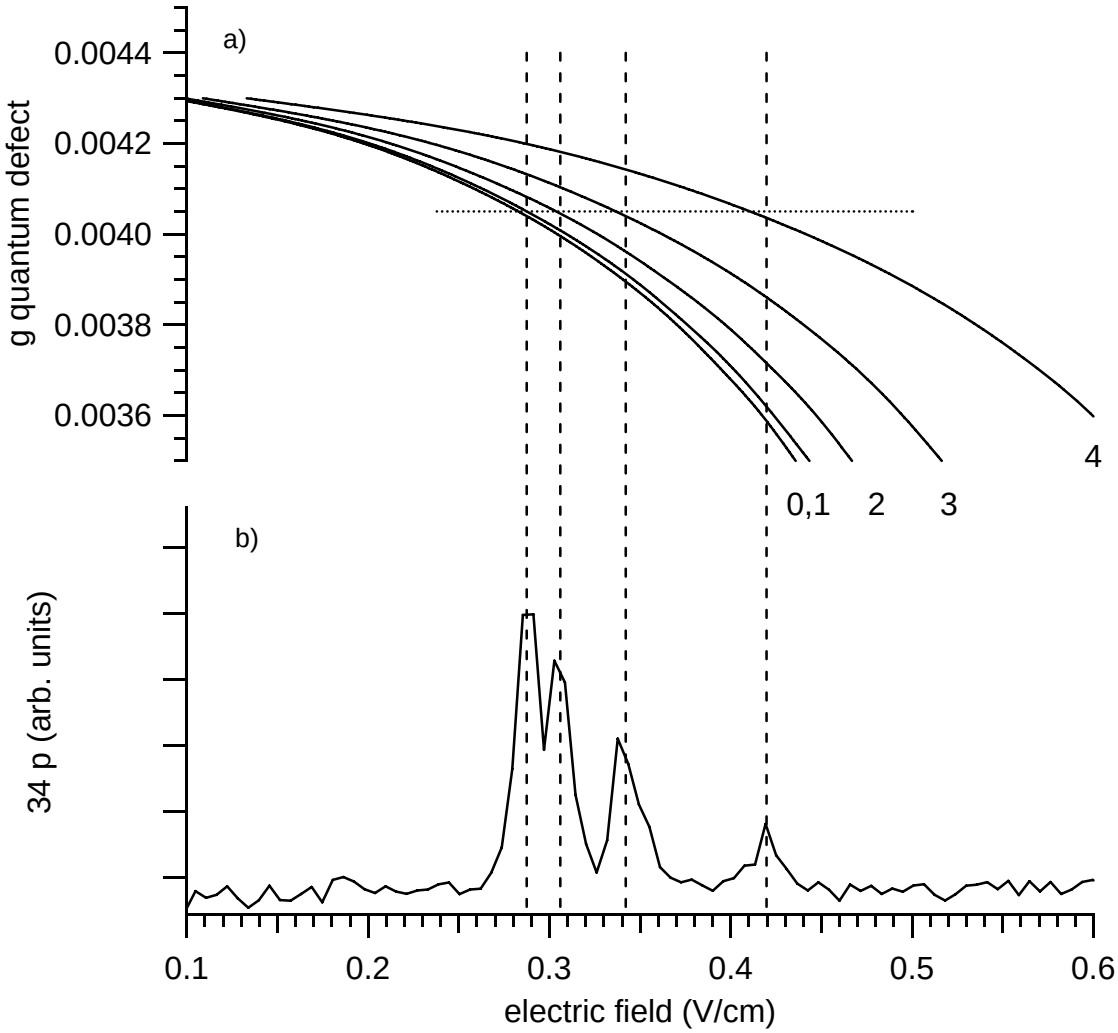

Figure 4.5: a) Resonance fields calculated for variable δ_g (vertical axis). The five lines correspond to different magnetic sub-levels (m_ℓ) for the $30g$ state. The calculated fields are shown on the horizontal axis to allow a direct comparison to the experimental data below. b) The same $32d_{5/2} + 32d_{5/2}$ resonant energy transfer spectrum as Fig. 4.2(a), shown on an expanded scale.

between Rydberg atoms is typically a dipole-dipole interaction, with the coupling between the two-atom states given by:

$$\hat{V}_{dd} = \frac{\vec{\mu}_{\rm A} \cdot \vec{\mu}_{\rm B} - 3(\vec{\mu}_{\rm A} \cdot \vec{n})(\vec{\mu}_{\rm B} \cdot \vec{n})}{R_{\rm AB}^3} \tag{4.3}$$

where $R_{\rm AB}$ is the separation of the two atoms, $\vec{n}$ is a unit vector pointing between them, and $\vec{\mu}_{\rm A}$ and $\vec{\mu}_{\rm B}$ are *transition* dipole moments evaluated on each of the individual atoms (A and B). In zero electric field the process given in Eq. 4.1 cannot be driven by the dipole-dipole interaction, since $\left\langle 32d_{5/2}|\vec{\mu}|30g_{7/2}\right\rangle = 0$, given the $\Delta\ell = \pm 1$ selection rule for transition dipole moments. However, when a weak electric field is applied, the ℓ quantum number is no longer good. Instead, it serves to label the dominant character of a state until it reaches the Stark manifold. In particular, the mixing of $30g$ with $30f$ gives $\left\langle 32d_{5/2}m_j{=}1/2|\mu_z|30g_{7/2}m_j{=}1/2\right\rangle = 17\, q_e a_0$ at 0.3 V/cm, where $q_e a_0$ is the atomic unit of electric dipole moment. The $32d_{5/2}$ to $34p_{3/2}$ coupling is allowed in zero field, and is much stronger. For example at 0.3 V/cm, $\left\langle 32d_{5/2}m_j{=}1/2|\mu_z|34p_{3/2}m_j{=}1/2\right\rangle = 357\, q_e a_0$ (which differs little from its zero field value).

It is interesting to compare the expected signal strengths for the resonance in Eq. 4.1 with other resonances that have been studied in similar experimental set-ups. For example, if we compare our transition dipole moments to those for the ^{85}Rb, $33s_{1/2} + 25s_{1/2} \rightarrow 24p_{1/2} + 34p_{3/2}$ process observed in Ref. [23], we would expect to have to wait approximately 10 times longer to see the equivalent amount of collision signal (at the same density). Since typical waiting times are 3 μs in Ref. [23] *vs.* 21 μs in our case, this is consistent.

In the quasi-static picture [23] the collision signal is expected to scale with the square of the density for a dipole-dipole interaction, and to a higher power for higher-order multipole processes (for small collision signals). Experimentally, we observe the square law behavior. It does not appear necessary to consider higher-order multipole interactions (see, for example, Ref. [1]).

4.5 Discussion

Resonant energy transfer spectroscopy has been demonstrated as a useful tool for the determination of unknown energy levels differences. In particular, prior to the work of Han *et al.* [68], no spectroscopy of the Rb ng-series had been performed.

Although resonant energy transfer spectroscopy is not a general technique for the determination of energy levels, there may be more possibilities for the observation of resonances than previously thought. In particular, at first glance the resonance studied in this paper (Eq. 4.1) does not appear to be allowed by the dipole-dipole interaction. However, the mixing of the g-state with the nearby f-state allows this process to be observed. It is expected that similar scenarios exist in Rb and other atoms.

Microwave transitions have been used to calibrate the applied electric fields in this work. However, there is a great deal of flexibility in the particular transition (and corresponding microwave frequency) that can be used for this calibration. A precise microwave source is not required for the actual spectroscopic measurement. This may be considered to be a significant advantage.

Chapter 5

Enhancement of Rydberg atom interactions using ac Stark shifts

In Chapter 4, resonant electric dipole-dipole interactions between cold Rydberg atoms using dc Stark shifts was discussed. In the following Chapter, we study the influence of ac Stark shifts on the two-atom dipole-dipole processes. Using ac Stark shifts for enhancing interactions benefits from the ability to shift energy levels either up or down by an appropriate choice of frequency. This Chapter is directly based on a paper published by the author together with J. A. Petrus and J. D. D. Martin [70].

5.1 Summary

The ac Stark effect was used to induce resonant energy transfer between translationally cold ^{85}Rb Rydberg atoms. When a 28.5 GHz dressing field was set at specific field strengths, the two-atom dipole-dipole process $43d_{5/2} + 43d_{5/2} \rightarrow 45p_{3/2} + 41f$ was dramatically enhanced, due to induced degeneracy of the initial and final states. This method for enhancing interactions is complementary to dc electric-field-induced resonant energy transfer, but has more flexibility due to the possibility of varying the applied frequency.

5.2 Introduction

The large transition dipole moments of Rydberg atoms make them much more sensitive to electric fields than less excited atoms. For example, the dc polarizabilities of low-angular momentum Rydberg states scale like n^7, where n is the principal quantum number [1]. This high sensitivity can be exploited for various means. For instance, energy transfer between Rydberg atoms may often be tuned into resonance using dc electric fields [16].

Rydberg atoms are also sensitive to small oscillating electric fields. For example, microwave dressing fields may be used to modify the dc polarizabilities of Rydberg states [17]. This could be used to reduce the influence of electric field inhomogeneities on the dephasing of a Rydberg atom qubit.

The present work demonstrates the use of weak microwave dressing fields to tune electric dipole-dipole interactions between Rydberg atoms into resonance, in a case where this cannot be accomplished by dc fields. We exploit the latitude to change both the amplitude *and* frequency of the dressing fields to create interatomic interactions which are much stronger than could otherwise be achieved.

Our results may be understood in terms of the ac Stark shifts of the relevant states. The ac Stark shift of a state $|\phi>$, in an electric field oscillating at angular frequency ω, with amplitude ε_z in the z direction, is given by Eq. 1.12:

$$\Delta E_\phi = \frac{1}{2}\varepsilon_z^2 \sum_{m \neq \phi} \frac{(E_\phi - E_m)|<\phi|\mu_z|m>|^2}{(E_\phi - E_m)^2 - (\hbar\omega)^2}$$

where E_m refers to the energy of state $|m>$ and μ_z is the electric dipole moment in the z direction. The modification of resonant energy transfer between Rydberg atoms by microwave fields has been previously studied in a strong field regime, where the Floquet description was more suitable [71, 72].

5.3 Experimental

The ac Stark shifts of Rydberg states can be probed using microwave spectroscopy. For our purposes, this provides a useful check on the validity of Eq. 1.12, and allows us to calibrate the applied field strengths when studying interatomic interactions.

Our apparatus has been described previously [43, 44]. A standard vapor cell magneto-optical trap (MOT) acts as a source of cold ^{85}Rb atoms. These are excited to $49s_{1/2}$ Rydberg states using a 1 μs pulse of laser light. Before excitation, the magnetic and electric fields are reduced to less than 0.02 G and 0.05 V/cm respectively. Approximately 3 μs after excitation, a 28.5 GHz ac dressing field is turned on. While the dressing field is on, a ≈ 33 GHz probe drives the $49s_{1/2} - 50s_{1/2}$ two-photon transition. The probe pulse lasts 6 μs. The dressing field is then switched off and a selective field ionization pulse [1] is applied to measure the $49s_{1/2}$ and $50s_{1/2}$ populations. By scanning the probe frequency between laser shots and collecting the resulting spectra, we can measure the difference in the ac Stark shifts of the two states involved in the transition (see Fig. 5.1). As Eq. 1.12 indicates, the shifts should scale linearly with applied dressing field power. This is verified in Fig. 5.2.

As shown in Fig. 5.1, the linewidth of the transitions increase as they shift. By varying the Rydberg density and probe power, we have determined that this is not due to interatomic interactions or power broadening. The observed broadening is very sensitive to the alignment of the horn that launches the dressing microwaves towards the atoms, suggesting that it is due to spatial inhomogeneity of the dressing fields over the cold atom sample. Minimizing this inhomogeneity is a major technical challenge in using dressing fields.

By evaluating the matrix elements in Eq. 1.12 using the techniques of Zimmermann *et al.* [18], we can compute the frequency dependence of the ac Stark shift. In particular, as the denominator of Eq. 1.12 suggests, the shift direction may be reversed by changing ω. Spectroscopy probes the differential shift between the two levels involved, and this may also be reversed. For example, we have observed that the $49s_{1/2} - 50s_{1/2}$ transition is shifted to higher frequency with a dressing field of 37.45 GHz, and that this shift is also proportional to dressing power. This ability to change the direction of differential energy shifts with the applied frequency is essential to what follows.

5.4 Results

It is well-known that dc Stark shifts may be used to enhance the interactions between Rydberg atoms [16, 1]. For example, consider the following resonant energy transfer process in Rb, which may be driven by the dipole-dipole interaction:

$$nd_{5/2} + nd_{5/2} \rightarrow (n+2)p_{3/2} + (n-2)f_{5/2,7/2}. \tag{5.1}$$

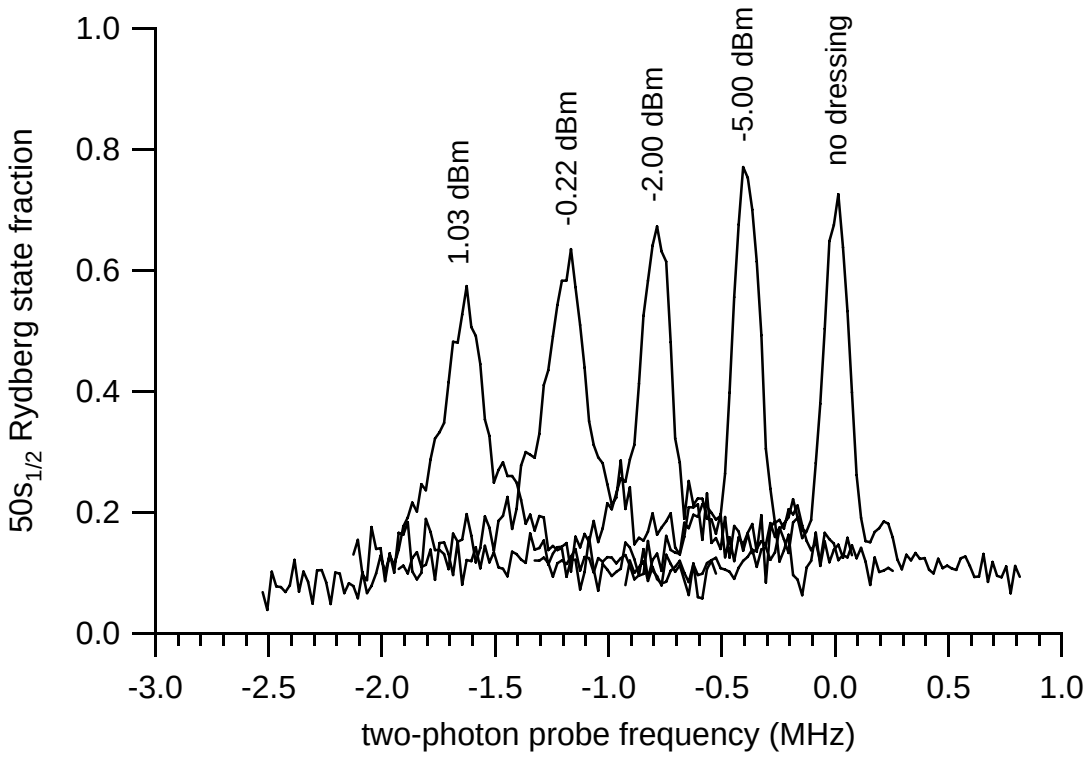

Figure 5.1: Observation of the two-photon $49s_{1/2} - 50s_{1/2}$ microwave transition for different powers of a 28.5 GHz dressing field. The probe frequency shown on the horizontal axis is twice the applied frequency, offset by 66.012926 GHz for clarity. The synthesizer power settings are indicated.

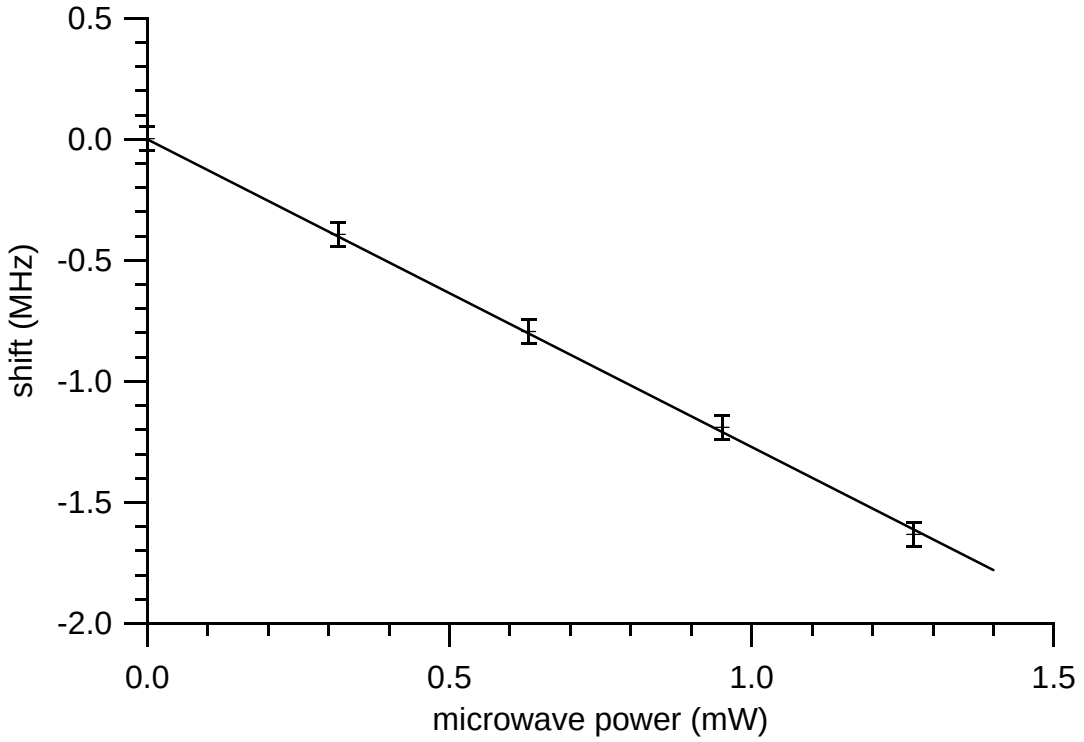

Figure 5.2: Shift in the line centers $49s_{1/2}-50s_{1/2}$ as a function of synthesizer power. Based on a calculated differential shift of $-0.195\,\mathrm{GHz/(V/cm)^2}$ from Eq. 1.12, we can find the calibration factor relating the synthesizer power to ε_z^2.

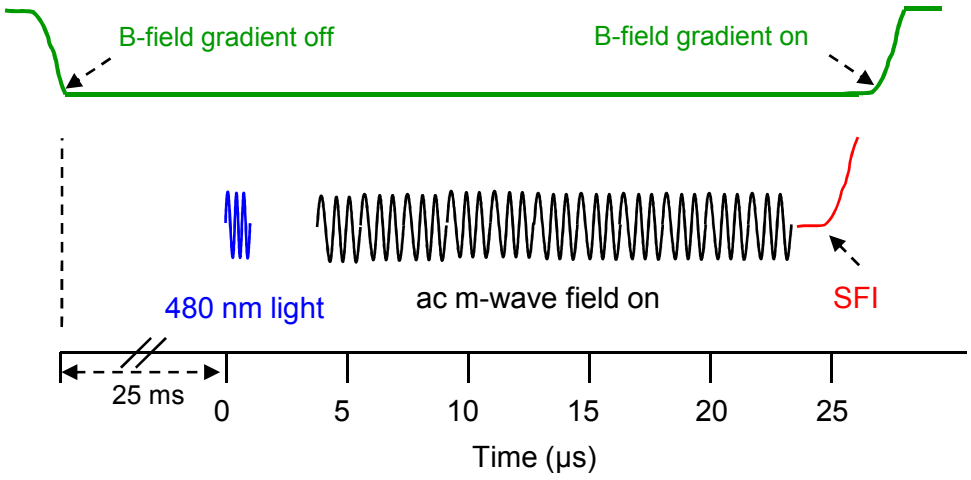

Figure 5.3: Timing diagram for ac electric-field-induced RET experiments. This sequence is repeated at 10 Hz.

For $n = 44$ the energy of the final state is approximately 60 MHz higher than that of the initial state (calculated using the spectroscopic data of Ref.'s [9, 68]). However, as an electric field is applied, the $42f$ states exhibit strong, quadratic Stark shifts to lower energies. This tunes the process into resonance, as shown in Fig. 5.4. In particular, atoms are excited to $nd_{5/2}$ Rydberg states and allowed to interact in the presence of a weak dc field. By varying the dc electric field between laser shots, and detecting the $(n+2)p$ population by selective field ionization, resonant energy transfer spectra may be obtained (see Ref. [65] for more details). As Fig. 5.4 illustrates, at $n = 44$ the resonance condition is turned on by a weak electric field, but for $n = 43$ (see Fig. 5.5) it is tuned further out of resonance. In this case the initial state is higher in energy than the final state by ≈ 10 MHz.

Since dc fields cannot tune $43d_{5/2} + 43d_{5/2} \rightarrow 45p_{3/2} + 41f_{5/2,7/2}$ into resonance, we consider using ac fields. In particular, we expect that the flexibility in the choice of ω, which allows shift directions to be reversed, could be beneficial. To illustrate this, the difference in ac Stark shifts between the final and initial states have been computed as a function of frequency using Eq 1.12. Figure 5.6 illustrates that over certain frequency ranges the ac field would shift the initial and final states closer into resonance – which could not be achieved with a dc electric field (see Fig. 5.5).

To experimentally test this idea, we have looked for the resonant energy transfer

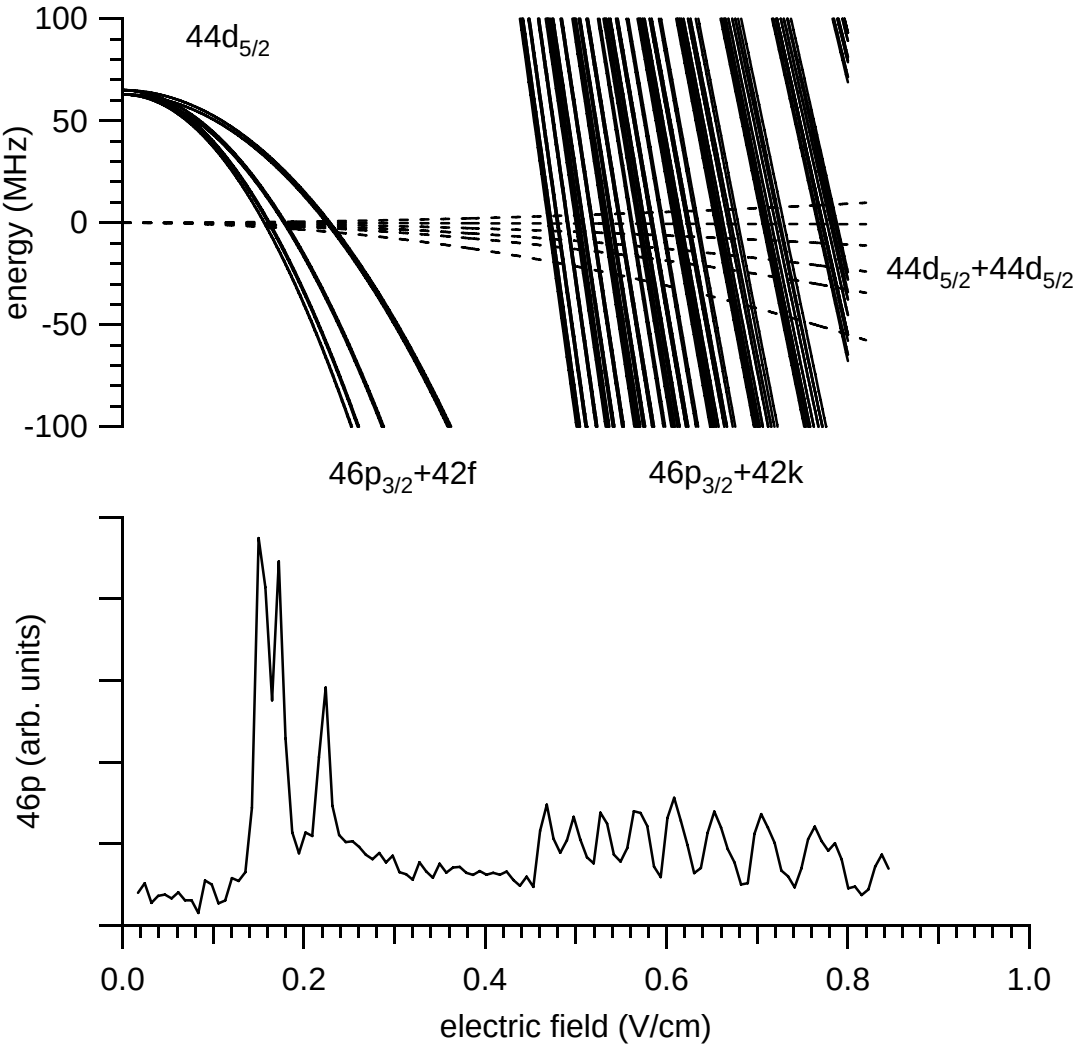

Figure 5.4: The dc electric-field-induced RET spectrum, with atoms initially in the $44d_{5/2}$ state. Also shown are the calculated total energy of several two atoms states, relative to the zero field energy of $nd_{5/2} + nd_{5/2}$, where $n = 44$. For the initial states $nd_{5/2} + nd_{5/2}$ (dashed lines), we plot all magnetic sublevel possibilities for each of the two atoms involved ($m_j = 1/2, 3/2, 5/2$). In the case of the final states $46p_{3/2} + 42f$, we consider the different possibilities for the two atom energies depending on the magnetic sublevel of the $(n+2)p_{3/2}$ states ($m_j = 1/2, 3/2$), and the $(n-2)f$ and $(n-2)k$ states ($m_j = 1/2, ..., 7/2$). The calculations follow the procedures of Ref. [18] and use the spectroscopic data of Ref.'s [9] and [68]. The observed RET peaks shown in the spectrum (lower graph) have excellent agreement with the theoretical predictions (top graph) where the total energy of the initial states intersect with the total energy of the final states.

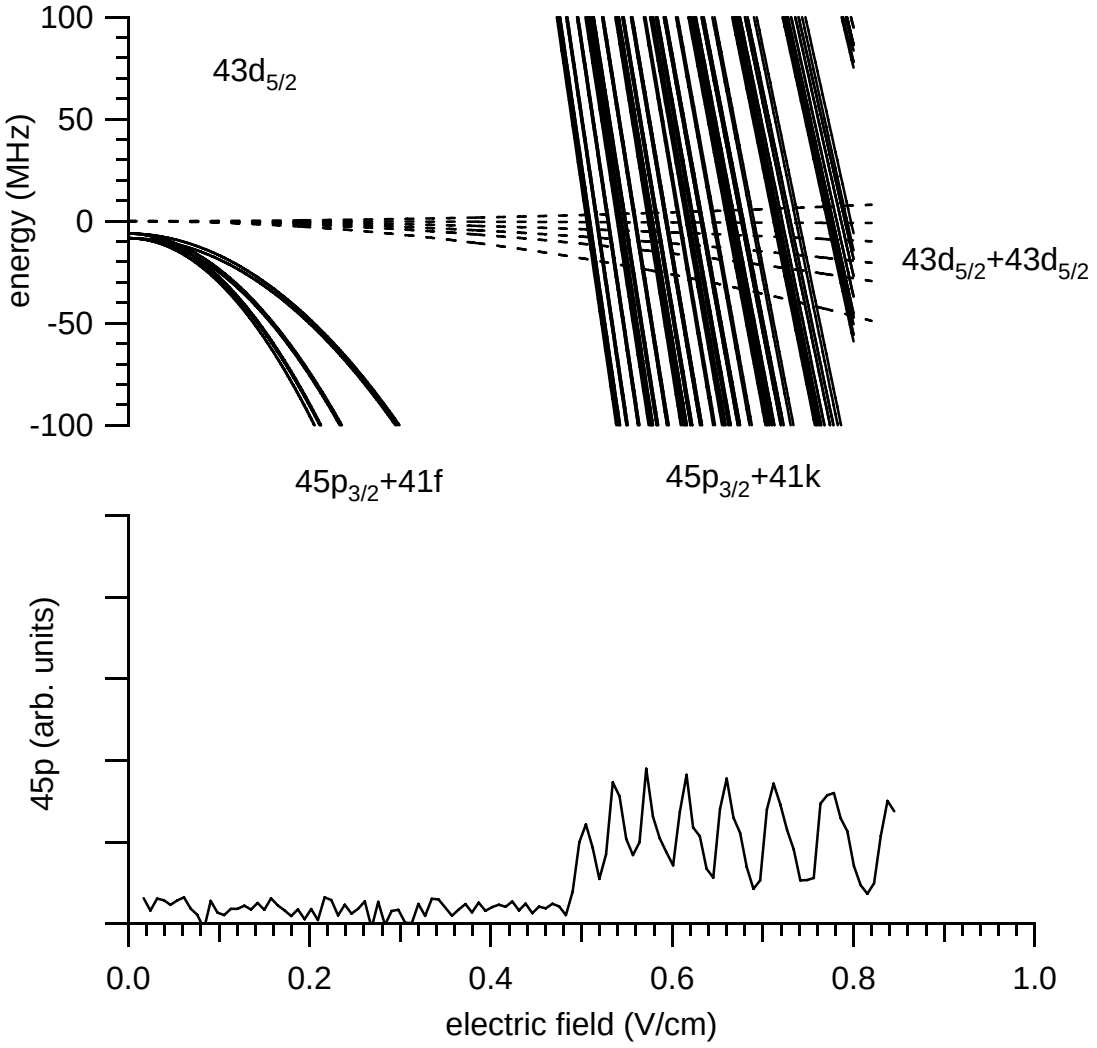

Figure 5.5: the dc electric-field-induced resonant energy transfer spectra, with atoms initially in the $43d_{5/2}$ state. Also shown are the calculated total energy of several two atoms states, relative to the zero field energy of $nd_{5/2}+nd_{5/2}$, where $n = 43$. For the initial states $nd_{5/2} + nd_{5/2}$ (dashed lines), we plot all magnetic sublevel possibilities for each of the two atoms involved ($m_j = 1/2, 3/2, 5/2$). In the case of the final states, we consider the different possibilities for the two atom energies depending on the magnetic sublevel of the $(n+2)p_{3/2}$ states ($m_j = 1/2, 3/2$), and the $(n-2)f$ and $(n-2)k$ states ($m_j = 1/2, ..., 7/2$). The calculations follow the procedures of Ref. [18] and use the spectroscopic data of Ref.'s [9] and [68].

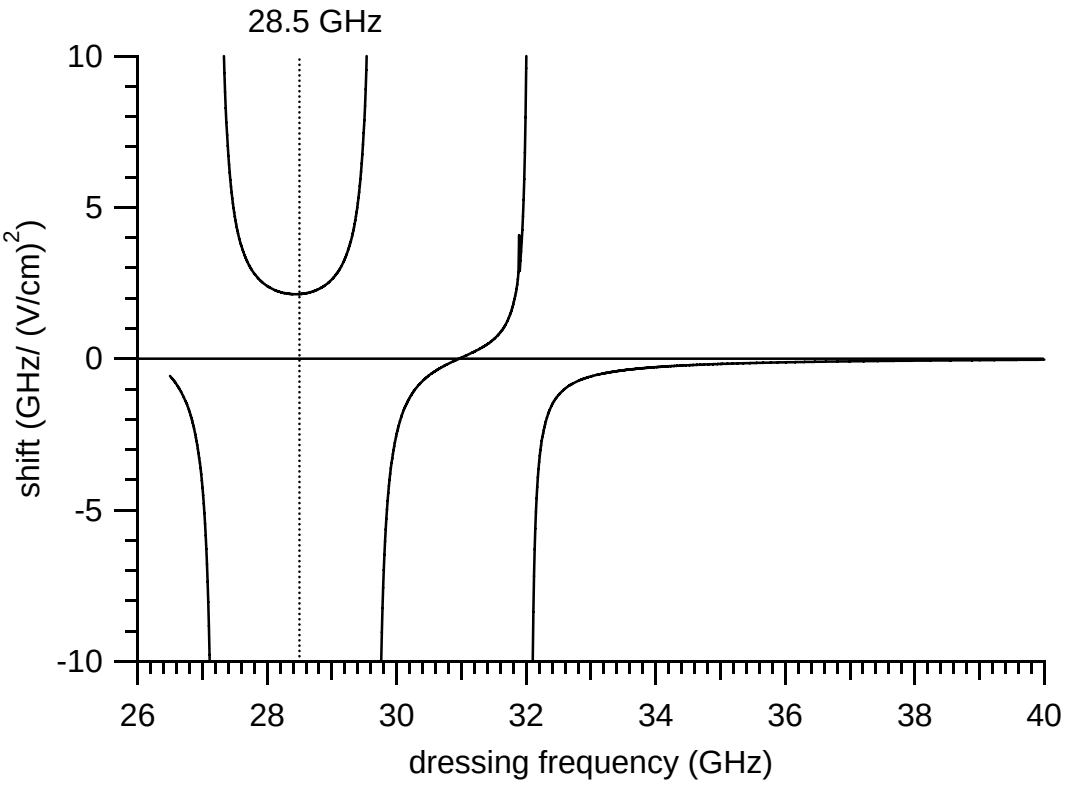

Figure 5.6: Calculated difference in the ac Stark shifts of the final and initial states of the process $43d_{5/2} + 43d_{5/2} \rightarrow 45p_{3/2} + 41f_{5/2}$ (all in $m_j = 1/2$) as a function of microwave frequency. With no microwave field, the final state is lower in energy than the initial state by 6.0 MHz and 8.3 MHz (for $41f_{5/2}$ and $41f_{7/2}$ respectively) [9, 68]. Therefore, frequencies where the shift is positive in this figure (*ie.* 28.5 GHz) will push this process closer to resonance.

process: $43d_{5/2} + 43d_{5/2} \rightarrow 45p_{3/2} + 41f_{5/2,7/2}$, in the presence of a 28.5 GHz microwave field. The atoms are excited to $43d_{5/2}$ Rydberg states (as discussed above), and the dressing field is turned on $3\,\mu$s after excitation. This field is held on for $20\,\mu$s until shortly before selective field ionization. This is repeated, scanning the applied microwave power between shots. The typical experimental sequence for a single shot is shown in Fig. 5.3. No deliberate dc electric field is applied. As Fig. 5.7 indicates, a significant population transfer to the $45p$ state is observed with the microwave field applied. As with the dc case, a series of resonances are observed. This is expected, due to the different magnetic sublevel possibilities for the final and initial states (see below). When the microwave field strength is fixed at a resonance position and the overall Rydberg density of the sample is varied (by changing the excitation laser power), the fraction transferred decreases with reduced density. This confirms that the observed resonances are due to an interatomic process. The transferred fraction grows linearly with density (for small transfer fractions, where depletion of the initial states is not significant). The widths of the resonances also increase with density. Figure 5.8 shows same spectrum as in Fig. 5.7 in addition to the calculated total energies of initial and final state atom pairs for different magnetic sublevel possibilities of $43d_{5/2} + 43d_{5/2} \rightarrow 45p_{3/2} + 41f_{5/2,7/2}$. Note that the horizontal axis in Fig. 5.8 is converted to V/cm whereas in Fig. 5.7 it is $(\mathrm{V/cm})^2$.

To calibrate the applied fields in Fig. 5.7, we observe the single-photon transition $43d_{5/2} - 45p_{3/2}$ with a series of dressing field strengths. As with the $49s_{1/2} - 50s_{1/2}$ case, the shifts are observed to be linear in applied microwave power. However, this case is slightly more complicated, due to the different magnetic sublevels involved. By equating the experimentally observed shift of these transitions with those based on the prediction of Eq. 1.12, we can determine the factor relating ε_z^2 to the applied microwave power. This calibration can be compared with the field calibration obtained from the $49s_{1/2}-50s_{1/2}$ line discussed at the beginning of this paper. These calibrations agree to within 20 %. Discrepancies may be due to the distribution of the probe field, which will have a slightly different spatial distribution over the trapped atom cloud at these two different frequencies.

Although the experiment is done with no deliberately applied dc electric fields, they are difficult to avoid, since they vary from day to day. Therefore, the frequencies of each of the $43d_{5/2} - 45p_{3/2}$ and $43d_{5/2} - 41f_{5/2,7/2}$ transitions are measured, with no dressing field present. These give the experimental difference in energies between the final and initial states of Eq. 5.1 for the field conditions of the experiment. We find that this "energy defect", $\delta E \approx -7.4 \pm 0.1$ MHz for the $41f_{5/2}$

case and $\approx -9.6 \pm 0.1$ MHz for the $41f_{7/2}$ case. These differ from the values of $-6.0(5)$ MHz and $-8.3(4)$ MHz obtained from the constants of Ref.'s [9] and [68]. Although a small electric field explains some of this discrepancy, the shifts of the $43d_{5/2} - 45p_{3/2}$ and $43d_{5/2} - 41f_{5/2,7/2}$ lines are not consistent with the same field. In addition, the field required to explain the shift of the $43d_{5/2} - 45p_{3/2}$ line exceeds the uncertainty in the electric field zero (± 0.05 V/cm), suggesting that a slight adjustment of the spectroscopic constants may be necessary.

From the experimentally observed energy defects we can calculate the resonance field strengths for the different magnetic sublevel possibilities. The ac Stark shifts for a state $|\phi>$ may be written as $\Delta E_\phi = k_\phi(\omega)\varepsilon_z^2$, where $k_\phi(\omega)$ is computed using Eq. 1.12. For a process like Eq. 5.1 ($|a> + |b> \rightarrow |c> + |d>$) the resonance fields may be computed by rearrangement of: $\delta E + [k_c(\omega) + k_d(\omega) - k_a(\omega) - k_b(\omega)]\,\varepsilon_z^2 = 0$, where δE is the energy difference between the final states ($|c> + |d>$) and the initial states ($|a> + |b>$) at zero field. Due to the selection rules for the dipole-dipole interaction, not all final and initial state magnetic sublevel combinations are coupled. In Fig. 5.7 the vertical lines indicate all calculated resonance fields consistent with $\Delta m_j = 0, \pm 1$ for each atom. Although many of the resonances are unresolved, the general agreement is good, and the highest field resonances are in clear agreement with the calculation.

Some caution is required in applying Eq. 1.12 to the $41f_{5/2,7/2}$ states, due to the small energy separation of the two fine structure components (2.3 MHz). The fine structure splittings of the other relevant states, $45p_{3/2,1/2}$ and $43d_{3/2,5/2}$, are significantly larger. When the Stark shifts become comparable to the splitting of the two fine structure components, Eq. 1.12 is not valid. To examine this issue, a Floquet calculation has been implemented (see, for example, Ref. [73]). This calculation shows that for the field strengths at the resonance locations, the perturbative calculation is accurate on the scale of Fig. 5.7.

5.5 Discussion

The modification of resonant energy transfer between Rydberg atoms due to *strong* microwave fields has been reported [71, 72]. In this case, the primary observation was that an integer number of microwave photons can either be given up or gained in resonant energy transfer to account for the energy defect between the initial and final states. Thus, the exact frequency of the ac field plays an important role.

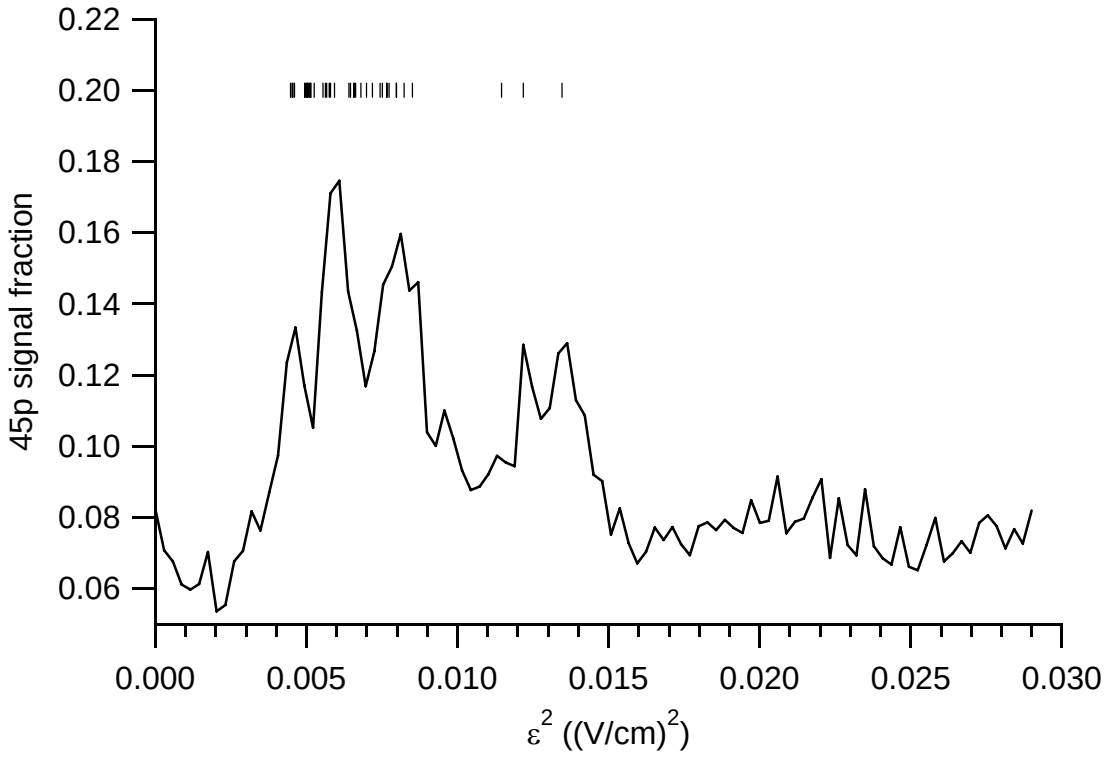

Figure 5.7: Observed $45p$ signal as a fraction of total Rydberg signal following a 23 μs waiting period after excitation of $43d_{5/2}$ Rydberg atoms, with a 28.5 GHz field of variable strength present. The field amplitude calibration is discussed in the text. The vertical lines indicate calculated resonance field strengths for the different magnetic sublevel possibilities for the initial and final states of $43d_{5/2} + 43d_{5/2} \rightarrow 45p_{3/2} + 41f_{5/2,7/2}$ (see text for details).

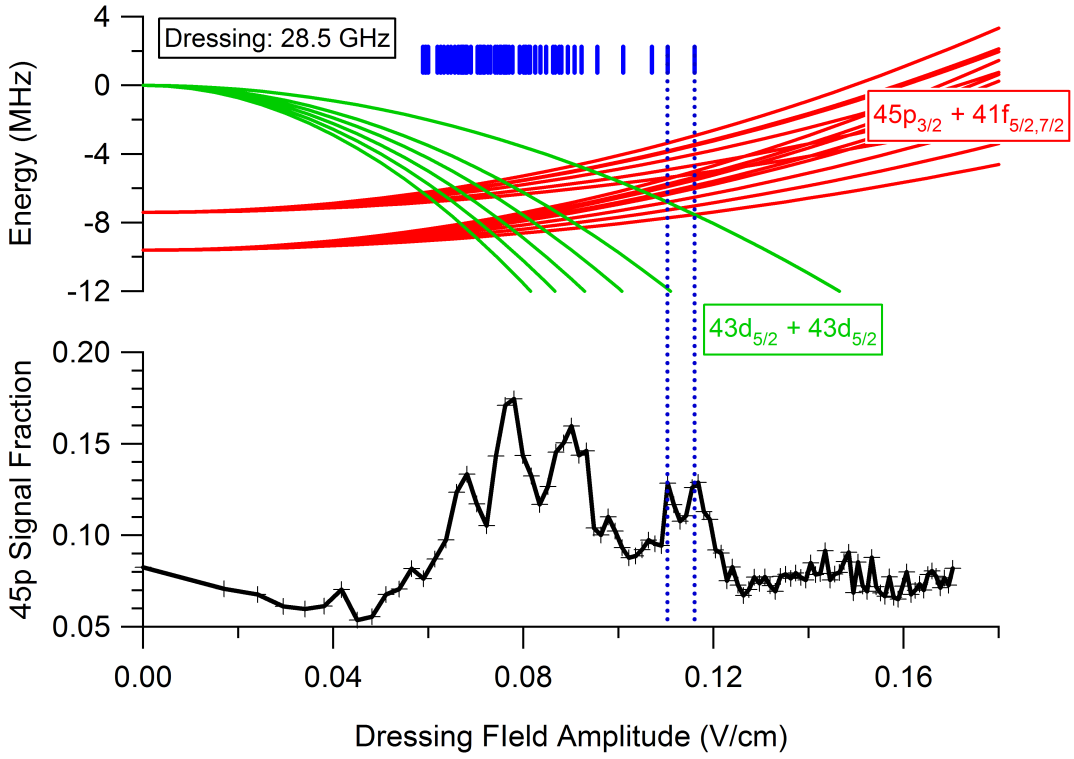

Figure 5.8: Same spectrum as in Fig. 5.7. Also are shown calculated total energies of initial and final state atom pairs for different magnetic sublevel possibilities of $43d_{5/2} + 43d_{5/2} \rightarrow 45p_{3/2} + 41f_{5/2,7/2}$. The two vertical dashed lines at high fields are shown to highlight the agreement between the calculated and experimentally observed resonance field amplitudes. The blue lines indicate dipole-dipole couplings that are allowed based on $|\Delta m_j| \leq 1$ for each atom. i.e. not all crossings correspond to states coupled by the dipole-dipole interaction.

The microwave power determines the number of "sidebands" present (the number of photons lost or gained in the collision). This can be accurately described using Floquet theory [72] (although the ac Stark effect does play a minor, observable role). In the present work – where the energy level shifts are perturbative – the important tuning parameter is the microwave power. The frequency is not as important – it should be set within a range to give the desired shift the correct sign. However, it should not be too close to any resonance, as this will prevent the microwave fields from being turned on and off adiabatically.

Rydberg atom interactions have recently received considerable attention in the context of quantum information processing with neutral atoms. For example, the dipole-dipole interaction between Rydberg atoms has been proposed as means of allowing clouds of cold atoms to store qubits, using a process known as dipole blockade [15]. Lukin *et al.* [15] considered using long-range resonant electric dipole interactions. However, initial experiments in Rb have focused on non-resonant van der Waals interactions [74, 75, 76]. Recently, local blockade has been observed in Cs using resonant dipole-dipole interactions between Rydberg atoms [28]. In Rb, several groups have identified Eq. 5.1 as a strong resonant process [77]. As the experimental results of the present work indicate, this process may be shifted into resonance by either dc or ac electric fields (Figs. 5.4 and 5.7). This would enhance the blockade effect. Possible advantages of ac fields over dc fields include the capacity to turn interactions on and off very quickly (due to the modulation capabilities of the source), and the ability to induce interactions at arbitrary dc fields.

In summary, perturbative ac fields have been demonstrated to enhance the interactions between Rydberg atoms by making them *resonant*. The frequency dependence of the ac Stark shift allows this to be accomplished with more versatility than the dc Stark shift. With strong laser fields, this approach could be used to enhance interactions between ground state atoms and/or molecules.

Chapter 6

ac electric-field-induced resonant energy transfer between cold Rydberg atoms

In the following Chapter, we further study the enhancement of interactomic interactions using 1.356 GHz ac dressing fields. Compared to earlier work performed at higher frequencies, 28.5 GHz (see Ch. 5), the choice of dressing frequency and structure of the spectra may be intuitively understood by analogy with the dc field case. This chapter is directly based on a paper published by the author together with J. A. Petrus and J. D. D. Martin [78].

6.1 Summary

An oscillating electric field at 1.356 GHz was used to promote the resonant energy transfer process: $43d_{5/2} + 43d_{5/2} \rightarrow 45p_{3/2} + 41f$ between translationally cold ^{85}Rb Rydberg atoms. The ac Stark shifts due to this dressing field created degeneracies between the initial and final two-atom states of this process. The ac field strength was scanned to collect spectra which are analogous to dc electric-field-induced resonant energy transfer spectra. Different resonances were observed for different magnetic sublevels involved in the process.

6.2 Introduction

The interaction energies between neighbouring Rydberg atoms can be much larger than between ground state atoms, separated by the same distance. These interactions can be made even larger if they are resonant. For example, Vogt *et al.* [28] have demonstrated that optical transitions to Cs Rydberg states are partially inhibited by tuning the energy of two Cs atoms in the $38p_{3/2}$ state to be identical to the energy of a $38s_{1/2}$, $39s_{1/2}$ atom pair. This tuning was accomplished using small electric fields ($\approx 1 - 2$ V/cm). With this induced degeneracy, the electric dipole-dipole interaction gives a first order energy shift, rather than a weaker second-order effect (van der Waals).

The use of external fields to create resonant interactions is common in atomic physics. Tunable dc magnetic fields may be used to create Feshbach resonances, dramatically enhancing the interactions between ultracold atoms [79, 80]. Oscillating fields may also be used. For example, Gerbier *et al.* [81] recently demonstrated that oscillating magnetic fields may also be used to shift dressed state energy levels into resonance, and thereby enhance interatomic interactions between ultracold atoms. The ability to vary both the frequency and amplitude of the "dressing field" gives additional latitude in achieving the resonance condition.

In a similar vein, we have recently shown that the resonant energy transfer process:

$$43d_{5/2} + 43d_{5/2} \rightarrow 45p_{3/2} + 41f \tag{6.1}$$

in ^{85}Rb may be greatly enhanced by the application of a microwave field (28.5 GHz) of appropriate field strengths [70]. The results agreed with the theoretical predictions for the ac Stark effect, but it is not obvious why 28.5 GHz was an appropriate frequency to use. Since all of the participating levels ($43d_{5/2}$, $45p_{3/2}$ and $41f$) show significant shifts at this frequency, the situation is complicated. In the present work, we demonstrate that a much lower frequency of 1.356 GHz – chosen to be slightly blue detuned from the $41f - 41g$ transition – shifts only $41f$ significantly. By varying the dressing field amplitude we can shift the process in Eq. 6.1 into resonance.

There is an additional benefit to using a lower dressing frequency. As discussed in Ref. [70], the different magnetic sublevels involved in Eq. 6.1 show different ac Stark shifts. With a 28.5 GHz dressing field, these give a complicated series of resonances. In the present work – at much lower frequencies – the spectra are not

as complicated, as the only important magnetic sublevel structure is due to the $41f$ states.

6.3 Theoretical Background

This section begins by motivating the choice of a dressing frequency of 1.356 GHz, and concludes by discussing the techniques used for calculating the dressed atom energy levels.

The process given in Eq. 6.1 is not resonant in the absence of applied fields. The final state is lower in energy than the initial state by approximately 10 MHz [70]. The $41f$ states shift to lower energy with increasing dc electric field. The other states involved have significantly smaller dc polarizabilities, and do not shift as much. Therefore, the resonant energy transfer process in Eq. 6.1 cannot be shifted into resonance with a dc field.

The shift of the $41f$ states to lower energies can be intuitively understood using 2^{nd} order perturbation theory. For an arbitrary state $|\phi>$, and an electric field of magnitude $\varepsilon_{z,dc}$ pointing in the z direction:

$$\Delta E_\phi = \varepsilon_{z,dc}^2 \sum_{p \neq \phi} \frac{|<\phi|\mu_z|p>|^2}{(E_\phi - E_p)}, \tag{6.2}$$

where E_p refers to the energy of state $|p>$ and μ_z is the electric dipole moment in the z direction. Figure 6.1(a) illustrates the simplified case of one dominant perturber. States are pushed away in energy from the perturber. For the $41f$ state, the dominant nearby perturber is the $41g$ state, located 1.19 GHz higher in energy (see Fig. 6.2). As an electric field is applied, the $41f$ state shifts down in energy, away from $41g$.

The expression for the perturbative ac Stark shift is similar to that for the dc case:

$$\Delta E_\phi = \frac{1}{2}\varepsilon_{z,ac}^2 \sum_{p \neq \phi} \frac{(E_\phi - E_p)|<\phi|\mu_z|p>|^2}{(E_\phi - E_p)^2 - (\hbar\omega)^2}, \tag{6.3}$$

where ω is the angular frequency of a dressing field, pointing in the z direction with electric field amplitude $\varepsilon_{z,ac}$. (For a derivation, see Ref. [21].) Again, Fig. 6.1(b) illustrates the simplified case of one dominant perturber. In contrast to the dc effect, ω may be used to control the sign of the shift. In our specific case of Rb,

we expect that applying a dressing frequency greater than the $41f - 41g$ transition frequency would cause the $41f$ state to move up in energy with increasing dressing field strength. As we demonstrate experimentally in Sec. 6.4, this shifts the initial($43d_{5/2} + 43d_{5/2}$) and final states $45p_{3/2} + 41f$) of Eq. 6.1 into resonance.

Although the perturbative formula (Eq. 6.3) for the ac Stark shift provides insight, some caution is required in its application. In particular, the energy shifts of the $41f$ states that are required to make the process in Eq. 6.1 degenerate are of the same order of magnitude as the fine structure splitting between $41f_{5/2}$ and $41f_{7/2}$ levels (2.3 MHz). This was not as significant with a dressing field frequency of 28.5 GHz as the shifts of the $41f$ states were not as large (the $43d_{5/2}$ and $45p_{3/2}$ states shifted more to make up the energy difference in Eq. 6.1, and their fine structure splitting is much larger). To treat this complication the dressed energy levels are calculated using a Floquet approach [82]. This approach takes the "bare" basis states of energy E_{bi} and adds "sideband" states of energy $E_{bi} + k\hbar\omega$, where k is an integer. The ac field introduces coupling between states differing in sideband order k by one. Our basis set and couplings are very similar to those used in dc electric-field Stark map calculations [18]. These calculations use the experimentally determined ^{85}Rb Rydberg energy levels [9, 68] as input. A nice description of the Floquet approach is given in Ref. [73].

6.4 Apparatus and Results

We start with a general overview of the experiment. To observe resonant energy transfer, we optically excite cold ^{85}Rb atoms from a magneto-optical trap (MOT) to Rydberg states using a pulse of light. Then a dc or ac electric field of variable amplitude is applied. The Rydberg atoms are allowed to interact in this field for a fixed amount of time, and then a selective field ionization pulse is applied to measure the Rydberg state populations. If, for example, $43d_{5/2}$ Rydberg states are excited and the ac field establishes the resonance condition between the initial and final states shown in Eq. 6.1, then both $45p_{3/2}$ and $41f$ Rydberg atoms are observed. By scanning the field strength, repeating the excitation and detection process, and recording the fraction of Rydberg atoms transferred to the $45p_{3/2}$ level, resonant energy transfer spectra may be obtained (Fig. 6.4).

We will now discuss the various aspects of the experiment in more detail. The Rydberg atoms are excited using a two-colour scheme involving the 780 nm light

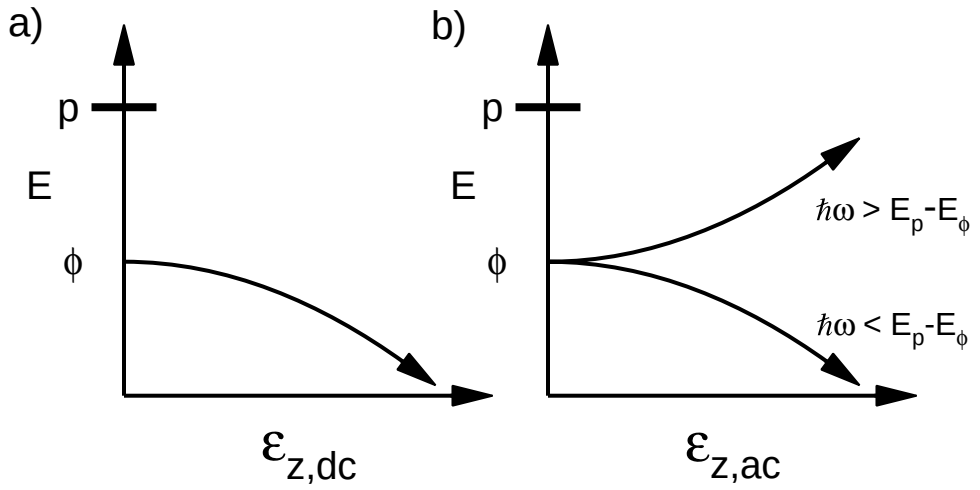

Figure 6.1: (a) The dc Stark effect in the case of a single nearby perturber $|p>$. The energy of the perturbed state $|\phi>$ is shown as a function of the dc electric-field magnitude $\varepsilon_{z,dc}$. (b) The ac Stark effect in the case of a single nearby perturber $|p>$. In this case the shifts are shown as a function of the amplitude of the oscillating electric field $\varepsilon_{z,ac}$. These two figures illustrate that the ac Stark shift direction may be altered by an appropriate choice of frequency ω, whereas the dc Stark shift direction is fixed. In both cases the energy of the perturber also shifts with field strength; however, this has not been shown.

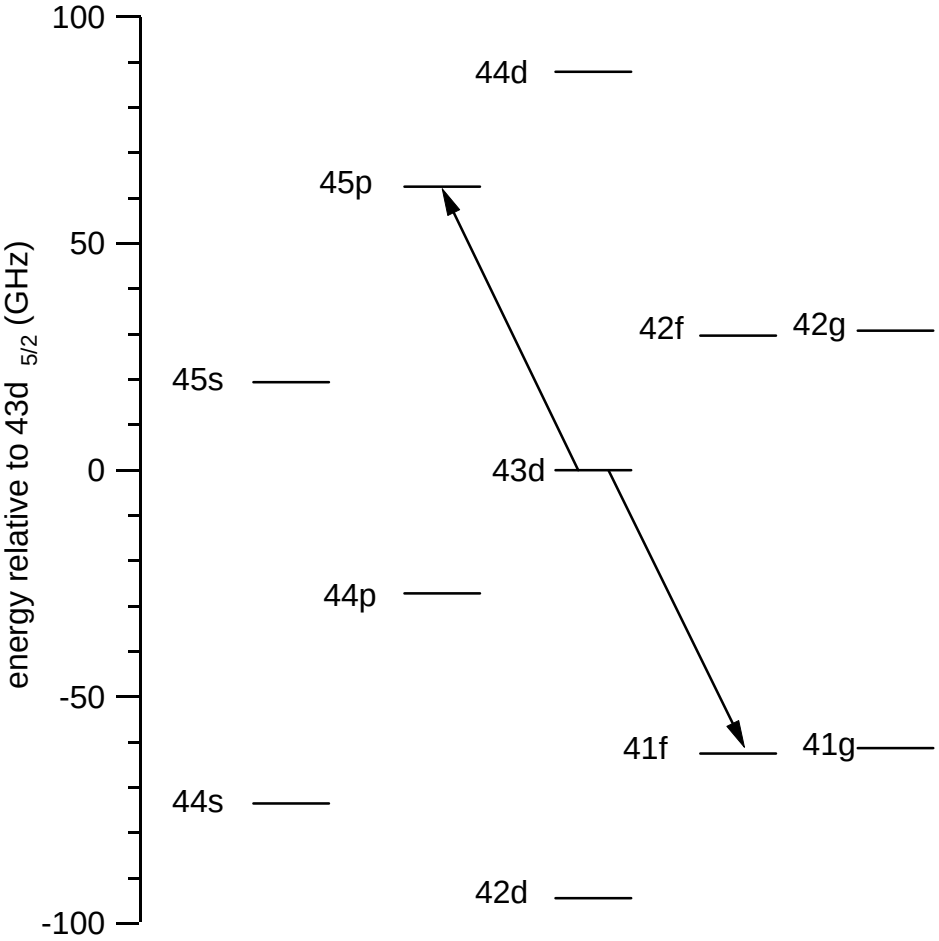

Figure 6.2: Some relevant ^{85}Rb Rydberg atom energy levels. Fine structure is too small to be observed on this scale (e.g. $43d_{3/2}$ and $43d_{5/2}$). In addition, although the g and f series appear degenerate, $41g$ is approximately 1.19 GHz higher in energy than $41f$. The arrows indicate the transitions involved in the ac-electric-field assisted resonant energy transfer (see Eq. 6.1).

used for cooling and trapping, and additional light at approximately 480 nm. This blue light is generated by frequency doubling a cw Ti:sapphire laser. It is introduced to the atoms in $1-2\,\mu$s pulses at a repetition rate of 10 Hz, using an acousto-optic modulator. Our frequency stabilization scheme for the Ti:sapphire laser has been discussed previously [44].

Approximately 25 ms prior to photoexcitation, the coil current generating the inhomogeneous magnetic field necessary for operation of the MOT is switched off. A 25 ms delay allows the fields due to eddy currents to decay. By using microwave spectroscopy of a magnetic-field-sensitive transition [43], we have verified that the residual magnetic field is less than 0.02 G at the time of photoexcitation. Following excitation, two parallel metal plates surrounding the atoms are used to apply both dc and ac fields. One-photon transitions may also be used to zero-out any residual electric field, and calibrate applied electric fields [65] (as required for dc electric field assisted resonant energy transfer spectra – see Fig. 6.3).

Photoexcitation to Rydberg states takes place with no deliberately applied dc electric field. For dc-electric-field induced resonant energy transfer spectra, the field is ramped up over 160 ns, immediately following Rydberg excitation (ramping this up relatively slowly avoids ringing). In the case of ac-electric-field induced resonant energy transfer, the oscillating field is switched on approximately 3 μs following photoexcitation (a delay of this magnitude was not necessary, but it is important that the dressing field and laser excitation do not temporally overlap). The Agilent E8254A synthesizer providing this field has a specified rise time of 100 ns. These field conditions are maintained for approximately 20 μs, in which time the cold atoms can possibily change states due to the resonant energy transfer process (at our densities this time gives maximum amounts of transfer of about $10-30\%$). It is essential to switch off the ac field prior to selective field ionization. Otherwise, this normally non-resonant field is shifted into resonance with various transitions as the electric field increases, creating population transfer unrelated to interatomic interactions.

Selective field ionization allows the $nd_{5/2}$, $(n+2)p_{3/2}$ and $(n-2)f$ populations to be distinguished. All three signals are measured simultaneously using boxcar integrators, digitized and recorded as a function of dc or ac field strength.

To illustrate the similarities between ac- and dc-electric-field induced resonant energy transfer spectra, both have been collected (see Figs. 6.3, 6.4). For the

process:

$$nd_{5/2} + nd_{5/2} \rightarrow (n+2)p_{3/2} + (n-2)f \tag{6.4}$$

the final state is higher in energy than the initial state for $n \geq 44$, allowing this process to be shifted into resonance with a dc electric field. In Ref. [70] an $n = 44$ spectrum was presented. Here in Fig. 6.3 we show the case of $n = 46$. There has been a previous report of this resonant energy transfer spectrum in the literature [83], but it differs from what we have observed, possibly due to differences in signal to noise. Note the excellent agreement between the calculated and observed resonance fields in Fig. 6.3.

As discussed in the introduction, and shown experimentally in Ref. [70], dc fields cannot be used to shift the process in Eq. 6.4 into resonance at $n = 43$ (see Fig. 5.5). However, as illustrated in Fig. 6.4, an ac electric field at frequency of 1.356 GHz, approximately 160 MHz higher than the $41f - 41g$ transition, raises the energy of the final state of Eq. 6.4, allowing the resonance condition to be achieved. The choice of 1.356 GHz is somewhat arbitrary. The frequency of the ac field should be far enough off resonance to avoid population transfer, but not so far that unreasonably strong field amplitudes are required. Comparing Fig. 6.4 to Fig. 5.8, it is noted that in the case of high dressing frequency of 28.5 GHz all of the states are shifting significantly whereas in the low dressing frequency case (1.356 GHz) only the f-state magnetic sublevels have significant shifts.

Due to unknown impedance mismatchs, we cannot readily determine the applied ac field strength electrically. To calibrate the applied ac electric field amplitude in Fig. 6.4 we observed microwave spectra of the single-photon $43d_{5/2}$ to $41f_{5/2,7/2}$ transitions in the presence of a 1.356 GHz dressing field. These were done at low density to avoid interatomic effects. A comparison of observed and expected shifts (calculated using the Floquet approach) allowed us to assign field strengths to synthesizer power levels. As we also use this calculation to predict the resonance field strengths, we cannot attach much significance to the overall absolute agreement between the observed and calculated resonance fields in Fig. 6.4. However, the simultaneous agreement of several resonance peaks (corresponding to different magnetic sub-level possibilities) suggests that the calculation is correct, as we only used the shift of the $m_j = 1/2$ states for the field strength calibration.

Some practical advantages of applying a relatively low frequency field (1.356 GHz here *vs.* 28.5 GHz in Ref. [70]) are that the resulting field homogeneity can be much larger due to the longer corresponding radiation wavelength, and that sources of lower RF frequencies are more readily available.

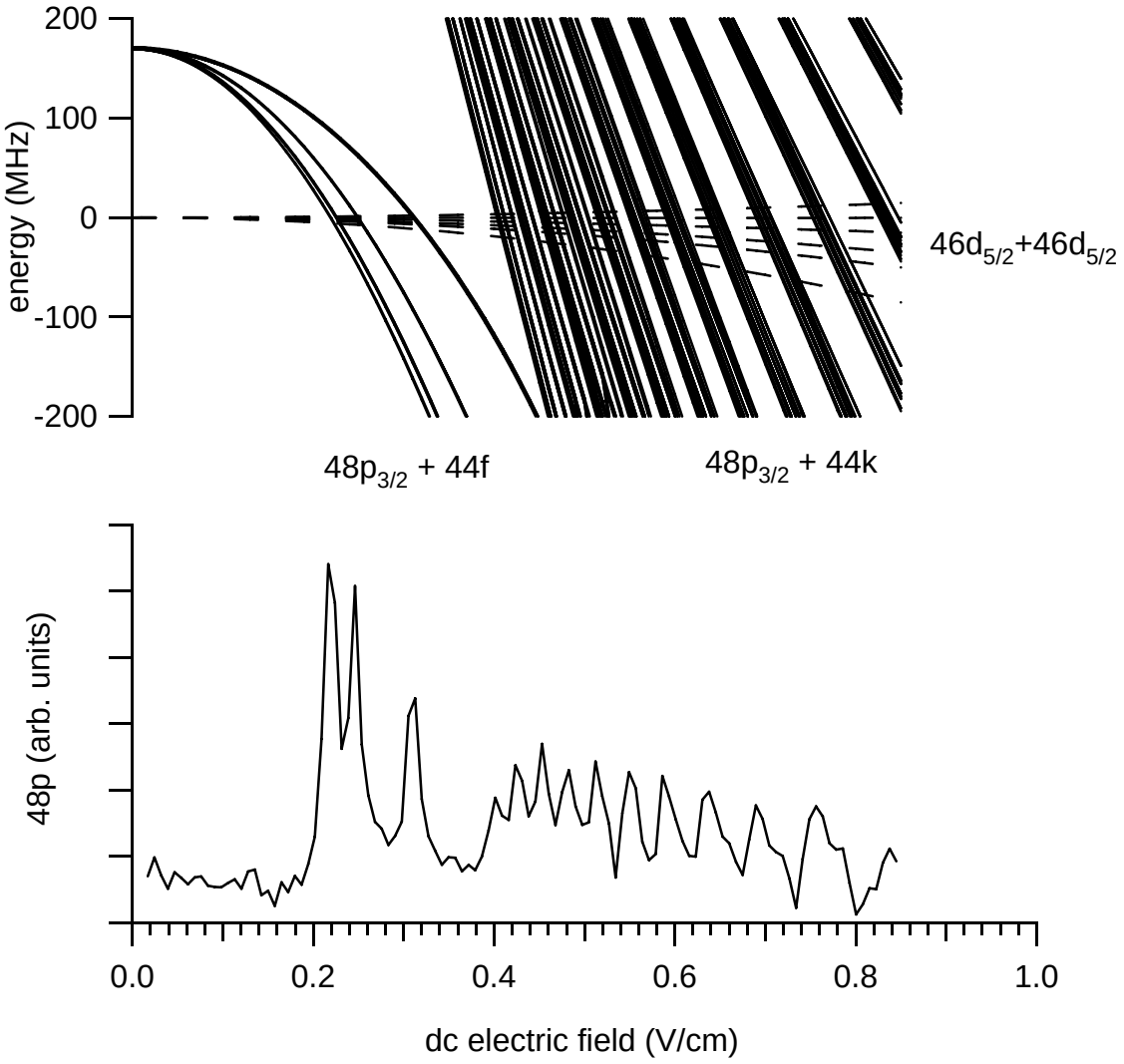

Figure 6.3: The dc electric-field-induced resonant energy transfer: $46d_{5/2}+46d_{5/2} \rightarrow 48p_{3/2}+44f, 44k$. The $44k$ label refers to Stark states – in this case superpositions of angular momentum states with $\ell \geq 4$. Also shown are calculated total energies of initial and final state atom pairs (for different magnetic sublevel possibilities). The calculation procedures are discussed in the text.

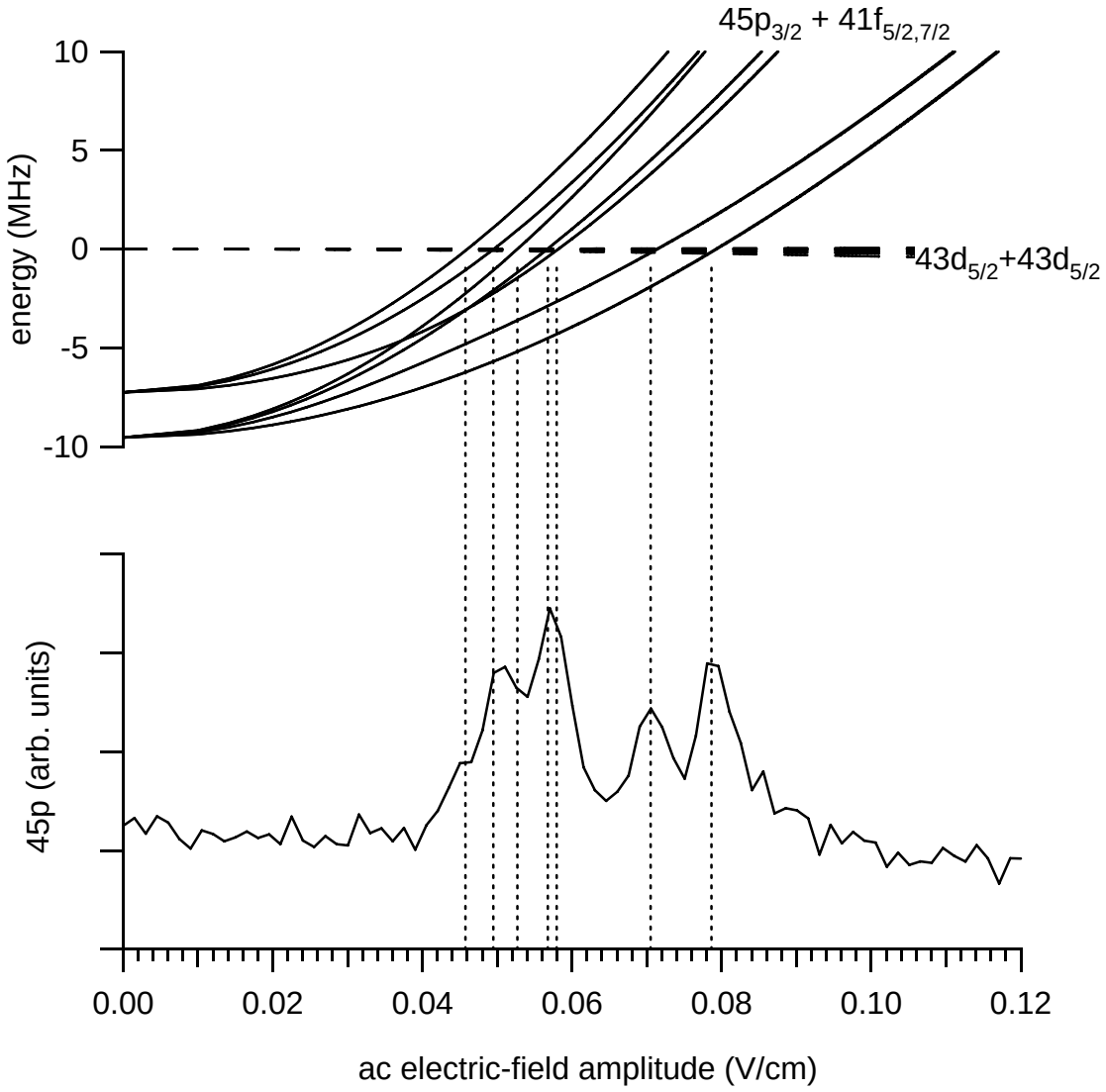

Figure 6.4: The ac electric-field-induced resonant energy transfer: $43d_{5/2}+43d_{5/2} \rightarrow 45p_{3/2}+41f$, using a dressing frequency of 1.356 GHz. Note the different horizontal axis scalings for Fig. 6.3 and Fig. 6.4. Also shown are calculated total energies of initial and final state atom pairs (for different magnetic sublevel possibilities). The calculation procedures are discussed in the text. Vertical dashed lines are shown to highlight the agreement between the calculated and experimentally observed resonance field amplitudes.

6.5 Discussion

Atomic energy levels may be determined by dc field induced resonant energy transfer spectra (see, for example, Ref. [65]). The ac field induced resonant energy transfer process may also be useful in this context. In this and other applications the frequency of the applied fields allows a variability in the signs and magnitudes of the Stark shifts involved that gives more flexibility than the dc shift alone.

Chapter 7

Concluding Remarks

In this thesis work remarkable properties of laser cooled Rydberg states of ^{85}Rb atoms were employed to study interatomic interactions at precisions comparable to those obtainable in microwave spectroscopy.

For precise excitation of Rb atoms to Rydberg states a general technique for laser frequency stabilization was developed. Using this technique, lasers at arbitrary wavelengths can be stabilized with frequency drift of < 1 MHz/hr.

The large dipole moments of the Rydberg atoms are responsible for the observed dipole-dipole interactions between neighboring Rydberg states. Both static and oscillating electric fields were used to shift the energy levels of Rydberg atoms into resonance through dipole-dipole interactions. Resonant energy transfer, RET, between cold Rydberg atoms was then used to determine Rydberg atom energy levels and enhance interatomic interactions.

For energy level determination from RET spectroscopy, ultra cold ^{85}Rb atoms from a magneto-optical trap were optically excited to $32d_{5/2}$ Rydberg states. A dc electric field was applied and the atoms were allowed to interact with each other for about 21μs. At an electric field of approximately 0.3 V/cm, resonance transitions of the two atom dipole-dipole process $32d_{5/2} + 32d_{5/2} \rightarrow 34p_{3/2} + 30g$ were observed. The experimentally observed resonant fields, together with the Stark map calculations were used to determine the ^{85}Rb ng-series quantum defect to be $\delta_g(n = 30) = 0.00405(6)$.
Due to the sensitivity of Rydberg states to electric fields, Stark shifts of microwave transitions between nearby Rydberg states were used to compensate stray electric fields and precisely calibrate and apply known electric fields.

It is also shown that ac electric fields may be used to induce RET in a conceptually similar manner as dc electric fields. It was demonstrated that a dressing field of 28.5 GHz at a field strength corresponding to ≈ 0.09 V/cm enhances the two-atom dipole-dipole process $43d_{5/2} + 43d_{5/2} \rightarrow 45p_{3/2} + 41f$ for cold atomic ^{85}Rb. This is due to induced degeneracy of the initial and final states. The frequency dependence of the ac Stark shift allows RET between Rydberg atoms to be accomplished with more versatility than the dc Stark shift.

At a dressing field of 28.5 GHz all of the participating levels ($43d_{5/2}$, $45p_{3/2}$ and $41f$) show significant shifts and these give a complicated series of resonances. It is not obvious why 28.5 GHz was an appropriate frequency to use. We demonstrated that a much lower frequency of 1.356 GHz shifts only $41f$ significantly and we can still shift the $43d_{5/2} + 43d_{5/2} \rightarrow 45p_{3/2} + 41f$ process into resonance by varying the dressing field amplitude. Different resonances were observed at an ac electric-fields ≈ 0.06 V/cm for different magnetic sublevels involved in the process. Compared to the higher dressing field frequency of 28.5 GHz, the choice of dressing frequency of 1.356 GHz, which is slightly blue detuned from the $41f - 41g$ transition, and structure of the spectra may be understood, by analogy with the dc field case.

We have shown that dc and ac electric fields may be used to induce resonant energy transfer. This method for enhancing the interactions between Rydberg atoms may be useful for "dipole-blockade" [15]. The basic principle of the dipole blockade is that the excitation of one atom prevents the excitations of its neighbors due to the energy shift induced by the dipole-dipole interaction between a pair of atoms. The dipole blockade effect provides novel approaches for a number of applications in quantum information processing. Local blockade has been achieved through use of the van der Waals interaction between Rydberg atoms [74, 76] (See also Ref. [84] for progress on very small numbers of interacting atoms.) However, it is desirable to enhance the interatomic interactions by making them resonant. This has recently been achieved using dc electric fields [28]. The ac Stark shifts induced by dressing fields offer an additional means to accomplish this with possible distinct advantages. For example in a glass cell (coated with alkali) it is typically difficult to establish dc electric fields with external electrodes, whereas high frequency ac fields can be applied more easily (see, for example, Ref. [85]).

In this thesis work, precise measurement and control of the interaction between many cold Rydberg atoms have been reported. Recently the dipole blockade of two atoms, separated by more than a few μm, has been observed [86, 87]. It was recently found by Pohl *et al.* [88] that the presence of the third or more atoms can break

the dipole blockade. Saffman *et al.* [89] reviews the theoretical and experimental progress of the use of properties of Rydberg atoms for a wide range of quantum information tasks in the last decade.

References

[1] T. F. Gallagher, *Rydberg Atoms*. Cambridge University Press, 1994. 1, 2, 4, 5, 6, 7, 26, 48, 50, 51, 57, 60, 61

[2] J. P. Connerade, *Highly Excited Atoms*. Cambridge, 1998. 1

[3] National Institute of Standards and Technology (NIST) (http://physics.nist.gov/cuu/Constants/energy.html), 1998. 1

[4] C. Fabre, M. Gross, J. M. Raimond, and S. Haroche, "Measuring atomic dimensions by transmission of Rydberg atoms through micrometre size slits," *J. Phys. B: At. Mol. Phys.*, vol. 16, p. L671, 1983. 2, 11

[5] P. Filipovicz, P. Meystre, and G. R. nd H. Walther, "Rydberg atoms - A testing ground for quantum electrodynamics," *Optica Acta*, vol. 32, pp. 1105–1123, 1985. 2, 3

[6] W. E. Lamb, Jr., and T. M. Sanders, "Fine structure of n=3 Hydrogen by a radio-frequency method," *Phys. Rev.*, vol. 103, p. 313, 1956. 2

[7] P. Goy, J. M. Raimond, G. Vitrant, and S. Haroche, "Millimeter-wave spectroscopy in cesium Rydberg states. Quantum defects, fine- and hyperfine-structure measurements," *Phys. Rev. A.*, vol. 26, p. 2733. 2

[8] F. Merkt and H. Schmutz, "Very high resolution spectroscopy of high Rydberg states of the argon atom," *J. Chem. Phys.*, vol. 108, pp. 10033–10045, 1998. 2

[9] W. Li, I. Mourachko, M. W. Noel, and T. F. Gallagher, "Millimeter-wave spectoscopy of cold Rb Rydberg atoms in a magneto-optical trap: Quantum defects of the *ns*, *np*, and *nd* series," *Phys. Rev. A*, vol. 67, p. 052502, 2003. 2, 41, 50, 51, 64, 65, 66, 67, 69, 76

[10] A. Osterwalder and F. Merkt, "Using high Rydberg states as electric field sensors," *Phys. Rev. Lett.*, vol. 82, p. 1831, 1999. 2, 33, 50

[11] M. T. Frey, X. Ling, B. G. Lindsay, K. A. Smit, and F. B. Dunning, "Use of the stark effect to minimize residual electric fields in an experimental volume," *Rev. Sci. Instrum.*, vol. 64, p. 3649, 1993. 2

[12] T. Killian, S. Kulin, S. Bergeson, L. A. Orozco, and S. L. Rolston, "Creation of an ultracold neutral plasma," *Phys. Rev. Lett.*, vol. 83, p. 4776, 1999. 3

[13] M. P. Robinson, B. L. Tolra, M. W. Noel, T. F. Gallagher, and P. Pillet, "Spontaneous evolution of Rydberg atoms into an ultracold plasma," *Phys. Rev. Lett.*, vol. 85, p. 4466, 2000. 3

[14] D. Jaksch, J. I. Cirac, P. Zoller, S. L. Rolston, R. Côté, and M. D. Lukin, "Fast quantum gates for neutral atoms," *Phys. Rev. Lett.*, vol. 85, p. 2208, 2000. 3

[15] M. D. Lukin, M. Fleischhauer, and R. Coteothers, "Dipole Blockade and Quantum Information Processing in Mesoscopic Atomic Ensembles," *Phys. Rev. Lett.*, vol. 87, p. 037901, 2001. 3, 72, 85

[16] K. A. Safinya, J. F. Delpech, F. Gounand, W. Sandner, and T. F. Gallagher, "Resonant Rydberg-atom Rydberg-atom collisions," *Phys. Rev. Lett.*, vol. 47, p. 405, 1981. 3, 10, 11, 12, 48, 60, 61

[17] P. Hyafil *et al.*, "Coherence-Preserving Trap Architecture for Long-Term Control of Giant Rydberg Atoms," *Phys. Rev. Lett.*, vol. 93, p. 103001, 2004. 3, 60

[18] M. L. Zimmerman, M. G. Littman, M. M. Kash, and D. Kleppner, "Stark structure of the Rydberg states of alkali-metal atoms," *Phys. Rev. A*, vol. 20, p. 2251, 1979. 7, 34, 50, 52, 53, 54, 61, 65, 66, 76

[19] D. Vagale. private communication. 7, 8, 9

[20] I. I. Sobel'man, *Introduction to the Theory of Atomic Spectra*. Pergamon Press, 1972. 9

[21] M. Haas, U. D. Jentschura, and C. H. Keitel, "Comparison of classical and second quantized description of the dynamic Stark shift," *Am. J. Phys.*, vol. 74, p. 77, 2006. 9, 75

[22] T. F. Gallagher and P. Pillet, "Dipole-Dipole Interactions of Rydberg Atoms," in *Advances in Atomic, Molecular, and Optical Physics* (E. Arimondo, P. R. Berman, and C. C. Lin, eds.), vol. 56, pp. 161–218, Elsevier, 2008. 10

[23] W. R. Anderson, J. R. Veale, and T. F. Gallagher, "Resonant dipole-dipole energy transfer in a nearly frozen Rydberg gas," *Phys. Rev. Lett*, vol. 80, p. 249, 1998. 11, 48, 57

[24] I. Mourachko, D. Comparat, F. de Tomasi, A. Fioretti, P. Nosbaum, V. M. Akulin, and P. Pillet, "Many-body effects in a frozen Rydberg gas," *Phys. Rev. Lett.*, vol. 80, p. 253, 1998. 11, 48

[25] W. R. Anderson, M. P. Robinson, J. D. D. Martin, and T. F. Gallagher, "Dephasing of resonant energy transfer in a cold Rydberg gas," *Phys. Rev. A*, vol. 65, p. 063404, 2002. 11

[26] I. Mourachko, W. Li, and T. F. Gallagher, "Controlled many-body interactions in a frozen Rydberg gas," *Phys. Rev. A*, vol. 70, p. 031401(R), 2004. 11

[27] K. Afrousheh, P. Bohlouli-Zanjani, D. Vagale, A. Mugford, M. Fedorov, and J. D. D. Martin, "Spectroscopic observation of resonant electric dipole-dipole interactions between cold Rydberg atoms," *Phys. Rev. Lett.*, vol. 93, p. 233001, 2004. 11, 40

[28] T. Vogt, M. Viteau, J. Zhao, A. Chotia, D. Comparat, and P. Pillet, "Dipole blockade at Förster resonances in high resolution laser excitation of Rydberg states of Cesium atoms," *Phys. Rev. Lett.*, vol. 97, p. 083003, 2006. 11, 72, 74, 85

[29] H. J. Metcalf and P. van der Straten, *Laser Cooling and Trapping*. Springer, 1999. 13, 15, 17, 18

[30] U. Schünemann, H. Engler, R. Grimm, M. Weidemüller, and M. Zielonkowski, "Simple scheme for tunable frequency offset-locking of two lasers," *Rev. Sci. Instrum.*, vol. 70, p. 242, 1999. 13, 19, 20, 38

[31] K. L. Corwin, Z.-T. Lu, C. F. Hand, R. J. Epstein, and C. E. Wieman, "Frequncy-stablized diode laser with the Zeeman shift in an atomic vapor," *Appl. Opt.*, vol. 37, p. 3295, 1998. 13, 19

[32] D. W. Preston, "Doppler-free saturated absorption: Laser spectroscopy," *Am. J. Phys.*, vol. 64, p. 1432, 1996. 13, 19, 38

[33] C. P. Pearman, C. S. Adams, S. G. Cox, P. F. Griffin, D. A. Smith, and I. G. Hughes, "Polarization spectroscopy of a closed atomic transition: applications

to laser frequency locking," *J. Phys. B.*, vol. 35, p. 5141, 2002. 13, 20, 22, 24, 37, 38, 44

[34] C. Monroe, W. Swann, H. Robinson, and C. Wieman, "Very cold trapped atoms in a vapor cell," *Phys. Rev. Lett.*, vol. 65, p. 1571, 1990. 15

[35] E. Raab, M. Prentiss, A. Cable, S. Chu, and D. Pritchard, "Trapping of neutral-sodium atoms with radiation pressure," *Phys. Rev. Lett.*, vol. 59, p. 2631, 1987. 15

[36] P. Bohlouli-Zanjani, "High resolution microwave spectroscopy of ultra cold Rydberg atoms as a probe of electric and magnetic fields." M.Sc. Thesis. University of Waterloo, Waterloo, On, Canada, 2003. 15, 19, 29

[37] E. Arimondo, M. Inguscio, and P. Violino, "Experimental determinations of the hyperfine structure in the alkali atoms," *Rev. Mod. Phys.*, vol. 49, p. 31, 1977. 18

[38] R. L. Barger and J. L. Hall, "Pressure shift and broadening of Methane line at 3.39 μ studied by laser-saturated molecular absorption," *Phys. Rev. Lett.*, vol. 22, p. 4, 1969. 19, 36, 38

[39] T. F. Gallagher, L. M. Humphery, W. E. Cooke, R. M. Hill, and S. A. Edelstein, "Field ionization of highly excited states of Sodium," *Phys. Rev. A.*, vol. 16, 1977. 24

[40] R. F. Stebbings and F. B. Dunning, *Rydberg states of atoms and molecules*. Cambridge University Press, 1983. 26

[41] K. Afrousheh, "Observation of resonant electric dipole-dipole interactions between cold Rydberg atoms using microwave spectroscopy." Ph.D. Thesis. University of Waterloo, Waterloo, On, Canada, 2006. 30, 33

[42] H. G. Kuhn, *Atomic Spectra*. London: Longmans, 1962. 31, 33

[43] K. Afrousheh, P. Bohlouli-Zanjani, J. D. Carter, A. Mugford, and J. D. D. Martin, "Resonant electric dipole-dipole interactions between cold Rydberg atoms in a magnetic field," *Phys. Rev. A*, vol. 73, p. 063403, 2006. 31, 32, 33, 37, 40, 49, 50, 61, 79

[44] P. Bohlouli-Zanjani, K. Afrousheh, and J. D. D. Martin, "Optical transfer cavity stabilization using current-modulated injection-locked diode lasers," *Rev. Sci. Instrum.*, vol. 77, p. 093105, 2006. 35, 61, 79

[45] B. G. Lindsay, K. A. Smith, and F. B. Dunning, "Control of long-term output frequency drift in commercial dye-lasers," *Rev. Sci. Instrum.*, vol. 62, p. 1656, 1991. 36

[46] W. Z. Zhao, J. E. Simsarian, L. A. Orozco, and G. D. Sprouse, "A computer-based digital feedback control of frequency drift of multiple lasers," *Rev. Sci. Instrum.*, vol. 69, p. 3737, 1998. 36

[47] B. M. A. Rossi, V. Biancalana and L. Tomassetti, "Long-term drift laser frequency stabilization using purely optical reference," *Rev. Sci. Instrum.*, vol. 73, p. 2544, 2002. 36

[48] B. Burghardt, W. Jitschin, and G. Meisel, "Precise RF tuning for cw dye-lasers," *App. Phys.*, vol. 20, p. 141, 1979. 36

[49] E. Riedle, S. H. Ashworth, J. T. Farrell, Jr., and D. J. Nesbitt, "Stabilization and precise calibration of a continuous-wave difference-frequency spectrometer by use of a simple transfer cavity," *Rev. Sci. Instrum.*, vol. 65, p. 42, 1994. 36, 40

[50] D. F. Plusquellic, O. Votava, and D. J. Nesbitt, "Absolute frequency stabilization of an injection-seeded optical parametric oscillator," *Appl. Opt.*, vol. 35, p. 1464, 1996. 36

[51] J. Helmcke, S. A. Lee, and J. L. Hall, "Dye-laser spectrometer for ultrahigh spectral resolution - design and performance," *Appl. Opt.*, vol. 21, p. 1686, 1982. 36, 40

[52] A. Grabowski, R. Heidemann, R. Löw, J. Stuhler, and T. Pfau, "High resolution Rydberg spectroscopy of ultracold Rubidium atoms," *Fortschr. Phys.*, vol. 54, p. 765, 2006. 36

[53] R. Kowalski, S. Root, S. D. Gensemer, and P. L. Gould, "A frequency-modulated injection-locked diode laser for two-frequency generation," *Rev. Sci. Instrum.*, vol. 72, p. 2532, 2001. 37, 46

[54] C. J. Myatt, N. R. Newbury, and C. E. Wieman, "Simplified atom trap by using direct microwave modulation of a diode-laser," *Opt. Lett.*, vol. 18, p. 649, 1993. 38

[55] "Operator's manual model MBR-110 single frequency Ti:Sapphire laser," tech. rep., Coherent, Santa Clara, CA,, 2002. 40

[56] S. H. Autler and C. H. Townes, "Stark effect in rapidly varying fields," *Phys. Rev.*, vol. 100, p. 703, 1955. 41, 42

[57] C. Cohen-Tannoudji, J. Dupont-Roc, and G. Grynberg, *Atom-Photon Interactions : Basic Processes and Applications*. New York: J. Wiley & Sons, 1998. 41, 42

[58] B. K. Teo, D. Feldbaum, T. Cubel, J. R. Guest, P. R. Berman, and G. Raithel, "Autler-Townes spectroscopy of the $5s_{1/2} - 5p_{3/2} - 44d$ cascade of cold ^{85}Rb atoms," *Phys. Rev. A.*, vol. 68, p. 053407, 2003. 41, 42

[59] National Institute of Standards and Technology (NIST) (http://emtoolbox.nist.gov/Wavelength/Ciddor.asp), 30 March 2006. 44

[60] P. E. Ciddor, "Refractive index of air: New equations for the visible and near infrared," *Appl. Opt.*, vol. 35, p. 1566, 1996. 44

[61] J. Ye., S. Swartz, P. Jungner, and J. L. Hall, "Hyperfine structure and absolute frequency of the ^{87}Rb $5P_{3/2}$ state," *Opt. Lett.*, vol. 21, p. 1280, 1996. 44

[62] M. Zhu and J. R. W. Standridge, "Optical frequency standard for optical fiber communication based on the Rb $5s \rightarrow 5d$ two-photon transition," *Opt. Lett.*, vol. 22, p. 730, 1997. 44

[63] A. Bruner, V. Mahal, I. Kiryuschev, A. Arie, M. A. Arbore, and M. M. Fejer, "Frequency stability at the Kilohertz level of a Rubidium-locked diode laser at 192.114 THz," *Appl. Opt.*, vol. 37, p. 6410, 1998. 44

[64] J. L. Hall, M. S. Taubman, and J. Ye, "Laser stabilization," in *Handbook of Optics* (M. Bass, J. M. Enoch, E. V. Stryland, and W. L. Wolfe, eds.), vol. IV, Chap. 27, Optical Society of America, Washington, DC/McGraw-Hill, New York, 2000. 46

[65] K. Afrousheh, P. Bohlouli-Zanjani, J. A. Petrus, and J. D. D. Martin, "Determination of the ^{85}Rb ng-series quantum defect by electric-field-induced resonant energy transfer between cold Rydberg atoms," *Phys. Rev. A*, vol. 74, p. 062712, 2006. 47, 64, 79, 83

[66] R. C. Stoneman, M. D. Adams, and T. F. Gallagher, "Resonant-collision spectroscopy of Rydberg atoms," *Phys. Rev. Lett.*, vol. 58, p. 1324, 1987. 48, 49

[67] T. J. Carrol, K. Claringbould, A. Goodsell, M. J. Lim, and M. W. Noel, "Angular dependence of the dipole-dipole interaction in a nearly one-dimensional sample of Rydberg atoms," *Phys. Rev. Lett.*, vol. 93, no. 153001, 2004. 49, 51

[68] J. Han, Y. Jamil, D. V. L. Norum, P. J. Tanner, and T. F. Gallagher, "Rb nf quantum defects from millimeter-wave spectroscopy of cold ^{85}Rb Rydberg atoms," *Phys. Rev. A*, vol. 74, p. 054502, 2006. 49, 50, 51, 55, 57, 64, 65, 66, 67, 69, 76

[69] T. J. Carroll, S. Sunder, and M. W. Noel, "Many-body interactions in a sample of ultracold Rydberg atoms with varying dimensions and densities," *Phys. Rev. A*, vol. 73, p. 032725, 2006. 51

[70] P. Bohlouli-Zanjani, J. A. Petrus, and J. D. D. Martin, "Enhancement of Rydberg atom interactions using ac Stark shifts," *Phys. Rev. Lett.*, vol. 98, p. 203005, 2007. 59, 74, 75, 80

[71] R. Kachru, N. H. Tran, and T. F. Gallagher, "Microwave-assisted resonant collisional energy transfer in Na Rydberg states," *Phys. Rev. Lett.*, vol. 49, p. 191, 1982. 60, 69

[72] P. Pillet, R. Kachru, N. H. Tran, W. W. Smith, and T. F. Gallagher, "Radiative collisions in a strong-field regime," *Phys. Rev. Lett.*, vol. 50, p. 1763, 1983. 60, 69, 72

[73] W. van de Water *et al.*, "Microwave multiphoton and excitation of Helium Rydberg atoms," *Phys. Rev. A*, vol. 42, pp. 572–591, 1990. 69, 76

[74] D. Tong *et al.*, "Local blockade of rydberg excitation in an ultracold gas," *Phys. Rev. Lett.*, vol. 93, p. 063001, 2004. 72, 85

[75] K. Singer, M. Reetz-Lamour, T. Amthor, L. G. Marcassa, and M. Weidemüller, "Suppression of excitation and spectral broadening induced by interactions in a cold gas of Rydberg atoms," *Phys. Rev. Lett.*, vol. 93, p. 163001, 2004. 72

[76] T. Cubel Liebisch, A. Reinhard, P. R. Berman, and G. Raithel, "Atom counting statistics in ensembles of interacting Rydberg atoms," *Phys. Rev. Lett.*, vol. 95, p. 253002, 2005. 72, 85

[77] T. G. Walker and M. Saffman, "Zeros of Rydberg-Rydberg föster interactions," *J. Phys. B: At. Mol. Opt. Phys.*, vol. 38, p. S309, 2005. 72

[78] J. A. Petrus, P. Bohlouli-Zanjani, and J. D. D. Martin, "ac electric-field-induced resonant energy transfer between cold Rydberg atoms," *J. Phys. B: At. Mol. Opt. Phys.*, vol. 41, p. 245001, 2008. 73

[79] S. Inouye, M. R. Andrews, J. Stenger, H.-J. Miesner, D. M. Stamper-Kurn, and W. Ketterle, "Observation of Feshbach resonances in a Bose-Einstein condensate," *Nature*, vol. 392, p. 151, 1998. 74

[80] P. Courteille, R. S. Freeland, D. J. Heinzen, F. A. van Abeelen, and B. J. Verhaar, "Observation of a Feshbach resonance in cold atom scattering," *Phys. Rev. Lett.*, vol. 81, pp. 69–72, Jul 1998. 74

[81] F. Gerbier, A. Widera, S. Fölling, O. Mandel, and I. Bloch, "Resonant control of spin dynamics in ultracold quantum gases by microwave dressing," *Phys. Rev. A*, vol. 73, p. 041602, 2006. 74

[82] J. H. Shirley, "Solution of the Schrödinger equation with a Hamiltonian periodic in time," *Phys. Rev.*, vol. 138, pp. B979–B987, May 1965. 76

[83] M. Reetz-Lamour *et al.*, "Prospects of ultracold Rydberg gases for quantum information processing," *Fortschr. Phys.*, vol. 54, p. 776, 2006. 80

[84] T. A. Johnson *et al.*, "Rabi oscillations between ground and Rydberg states with dipole-dipole atomic interactions," *Phys. Rev. Lett.*, vol. 100, p. 113003, 2008. 85

[85] A. K. Mohapatra, T. R. Jackson, and C. S. Adams, "Coherent optical detection of highly excited Rydberg states using electromagnetically induced transparency," *Phys. Rev. Lett.*, vol. 98, p. 113003, 2007. 85

[86] E. Urban *et al.*, "Observation of Rydberg blockade between two atoms," *Nat. Phys.*, vol. 5, p. 110, 2009. 85

[87] A. Gatan *et al.*, "Observation of collective excitation of two individual atoms in the Rydberg blockade regime," *Nat. Phys.*, vol. 5, p. 115, 2009. 85

[88] T. Pohl and P. R. Berman, "Breaking the Dipole Blockade: Nearly Resonant Dipole Interactions in Few-Atom Systems," *Phys. Rev. Lett.*, vol. 102, p. 013004, 2009. 85

[89] M. Saffman, T. G. Walker, and K. M∅lmer, "Quantum information with Rydberg atoms," *arXiv:0909.4777v3*, May 2010. 86